



Universiteit  
Leiden  
The Netherlands

## **Putting a spin on it: amyloid aggregation from oligomers to fibrils**

Zurlo, E.

### **Citation**

Zurlo, E. (2020, July 9). *Putting a spin on it: amyloid aggregation from oligomers to fibrils*. *Casimir PhD Series*. Retrieved from <https://hdl.handle.net/1887/123273>

Version: Publisher's Version

License: [Licence agreement concerning inclusion of doctoral thesis in the Institutional Repository of the University of Leiden](#)

Downloaded from: <https://hdl.handle.net/1887/123273>

**Note:** To cite this publication please use the final published version (if applicable).

Cover Page



Universiteit Leiden



The handle <http://hdl.handle.net/1887/123273> holds various files of this Leiden University dissertation.

**Author:** Zurlo, E.

**Title:** Putting a spin on it: amyloid aggregation from oligomers to fibrils

**Issue Date:** 2020-07-09

# **Putting a Spin on it: Amyloid Aggregation from Oligomers to Fibrils**

Enrico Zurlo



# **Putting a Spin on it: Amyloid Aggregation from Oligomers to Fibrils**

**Proefschrift**

ter verkrijging van  
de graad van Doctor aan de Universiteit Leiden,  
op gezag van Rector Magnificus prof.mr. C.J.J.M. Stolker,  
volgens besluit van het College voor Promoties  
te verdedigen op donderdag 9 Juli 2020  
klokke 15:00

door

**Enrico Zurlo**

geboren te Cittadella (Italië)  
in 1987

Promotores: Dr. Martina Huber

Prof. Dr. Eric Eliel

Promotiecommissie: Dr. Marilena Di Valentin (Università di  
Padova, Italië)

Prof.dr. Thomas Schmidt (Universiteit Leiden)

Prof.dr. Marcellus Ubbink (Universiteit Leiden)

Dr. Shai Rahimipour (Bar-Ilan University, Israël)

Dr. Patrick van der Wel (Rijksuniversiteit Groningen)



**Universiteit  
Leiden**  
The Netherlands



**Casimir**  
research school

Casimir PhD series, Delft-Leiden 2020-16

ISBN 978-90-8593-443-1

An electronic version of this thesis can be found at <https://openaccess.leidenuniv.nl>

To

**my beloved mother Giuseppina who could not witness my  
achievements in the last few years**





# Contents

1	Introduction.....	1
1.1	Proteins and their properties .....	2
1.1.1	Structure of Proteins .....	2
1.1.2	Intrinsically disordered proteins.....	4
1.1.3	Alzheimer's disease: the amyloid $\beta$ peptide .....	5
1.1.4	Parkinson's disease: the alpha synuclein protein .....	6
1.1.5	Solid Phase Peptide Synthesis .....	6
1.2	Electron paramagnetic resonance.....	7
1.2.1	Electron Zeeman interaction and g-factor .....	8
1.2.2	Electron spin – nuclear spin interaction: hyperfine interaction.....	10
1.2.3	Spin-label EPR.....	11
1.2.4	Spin-label dynamics: The rotational correlation time .....	12
1.2.5	Distance determination by EPR: Dipole-dipole interaction .....	14
1.2.6	Double electron-electron resonance .....	14
1.3	Thesis outline .....	17
2	Synthesis and first CD and EPR characterization of small amyloid peptides designed to form oligomers.....	19
2.1	Introduction.....	20
2.2	Results .....	21
2.3	Discussion .....	23
2.4	Supporting information .....	24
2.4.1	Synthesis and Characterization of Peptides .....	24
2.4.2	Electron Paramagnetic Resonance.....	25
2.4.3	Circular Dichroism .....	26
2.4.4	Protocol of Aggregation Experiments .....	26
3	Tracking amyloid oligomerization with monomer resolution using a $^{13}$ -amino acid peptide with a backbone-fixed spin label.....	29
3.1	Introduction.....	30
3.2	Materials and methods .....	32
3.2.1	Synthesis and characterization of peptides .....	32
3.2.2	Protocol for the aggregation experiments.....	33
3.2.3	ThioflavinT fluorescence .....	34
3.2.4	EPR measurement conditions .....	34
3.2.5	Simulations of EPR spectra .....	34

3.2.6	Interpretation of $\tau_r$ values and molecular volumes .....	35
3.3	Results .....	36
3.4	Discussion .....	40
3.4.1	Is TOAC a good monitor for peptide size? .....	40
3.4.2	Influence of TOAC position on the aggregation of the EZ peptides .....	40
3.4.3	Oligomerization of T0EZ as followed by EPR .....	41
3.4.4	Aggregation of T0EZ.....	42
3.5	Conclusions and outlook .....	43
3.6	Supporting information .....	44
3.6.1	Supplementary figures .....	44
3.6.2	Supplementary materials and methods .....	47
3.6.3	Supplementary data .....	47
4	In situ kinetic measurements of $\alpha$ -synuclein aggregation reveal large population of short-lived oligomers.....	57
4.1	Introduction.....	58
4.2	Material and methods .....	59
4.2.1	Protein expression and labeling .....	59
4.2.2	Sample preparation .....	59
4.2.3	EPR measurement conditions.....	60
4.2.4	Simulations of EPR spectra .....	60
4.2.5	Fitting of kinetics .....	61
4.3	Results .....	62
4.4	Discussion .....	64
4.4.1	Relation of the EPR derived fractions to the aggregation state of $\alpha$ S.....	64
4.5	Conclusion .....	66
4.6	Supporting information .....	67
5	A two-armed probe for in-cell DEER measurements on protein.....	71
5.1	Introduction.....	72
5.2	Materials and methods.....	73
5.2.1	Protein expression and purification .....	74
5.2.2	DEER sample preparation .....	74
5.2.3	EPR measurements conditions .....	75
5.3	Results .....	76
5.3.1	Design and synthesis of Gd(III)-CLaNP13.....	76
5.3.2	Protein labeling.....	77
5.3.3	Results of EPR experiments .....	77

5.3.4	Results of distance measurements .....	78
5.3.5	In-cell DEER.....	79
5.4	Discussion.....	81
5.5	Supporting information.....	83
5.5.1	Cell culture and live cell imaging.....	84
5.5.2	Quantification of the in-cell T4-ATTO-647 concentration.....	84
6	Synthesis and characterization by EPR of backbone-labeled Amyloid $\beta$ peptides and influence of an antiamyloidogenic cyclic D,L- $\alpha$ -peptide as potential inhibitor for their aggregation.....	89
6.1	Introduction.....	90
6.2	Materials and methods .....	92
6.2.1	Synthesis and Characterization of Peptides .....	92
6.2.2	Protocol for the aggregation experiments.....	93
6.2.3	ThioflavinT fluorescence plate reader experiments.....	94
6.2.4	EPR measurement conditions .....	94
6.2.5	Simulations of EPR spectra .....	95
6.3	Results .....	95
6.4	Discussion.....	100
6.4.1	EPR properties of monomers .....	100
6.4.2	Influence of TOAC on aggregation behavior .....	101
6.4.3	Cyclic peptide CP-2 as amyloid aggregation inhibitor .....	101
6.5	Conclusions.....	102
6.6	Supporting information.....	103
6.6.1	Interpretation of $\tau_r$ values and molecular volumes.....	105
6.6.2	EPR experiments on spin-labeled CP-2.....	105
	Bibliography.....	107
	Summary .....	119
	Samenvatting.....	121
	Curriculum vitae .....	125
	List of publications.....	127
	Acknowledgments .....	129



# **1 Introduction**

Neurodegenerative diseases are a category of disorders that are characterized by a progressive degeneration of the structure and function of the neurons. As described in more details below, the most widely spread of such diseases are Alzheimer's disease and Parkinson's disease and they are expected to increase still further in the future due to the ageing of the population, causing large distress for society and a large burden for economy. Although treatments may help relieve some of the physical or mental symptoms associated with neurodegenerative diseases, there is currently no way to slow disease progression and no available treatments. Research on neurodegenerative diseases has considerably expanded over multiple scientific disciplines, however more progress is still needed.

This thesis focuses on amyloid proteins, a class of proteins that convert into amyloid fibrils. Such proteins are of high interest because they are related to many of the neurodegenerative diseases, such as Parkinson's disease (PD), type II diabetes, Huntington's disease and Alzheimer's disease (AD). Spin-label electron paramagnetic resonance (EPR) is the method we employed to study these complex systems. This chapter presents a brief introduction to this thesis. We describe the general structures of proteins, the intrinsically disordered proteins and their relation to neurodegenerative diseases. We explain the basis of the solid phase synthesis technique and give a general overview of EPR and the methods applied in this work.

## 1.1 Proteins and their properties

### *1.1.1 Structure of Proteins*

Proteins are large biomolecules composed of one or more long chains of amino acid residues, and perform a vast array of functions within an organism. A linear chain of amino acid residues is referred as a polypeptide. Short polypeptides are commonly called peptides, while a protein contains at least one long polypeptide<sup>1</sup>. In most cases proteins adopt a specific three-dimensional structure that allows them to carry out their specific functions in the cells. Generally, this protein structure is organized from primary to quaternary levels (Figure 1.1).

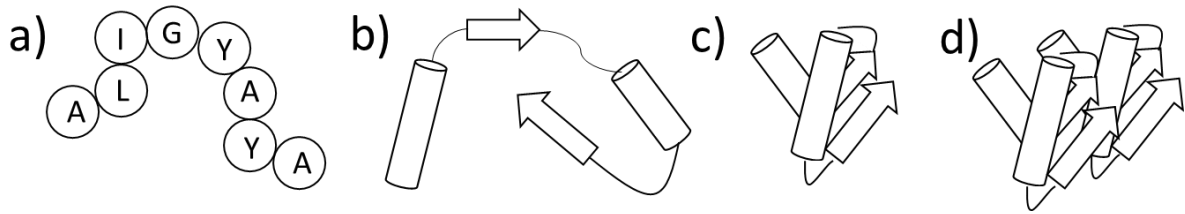


**Figure 1.1** Levels of protein structure. The primary amino acid sequence (a) (letters are acronyms of different amino acids) interacts to adopt secondary local structures (b). Compacting of these structures yields the global tertiary structure (c). Some proteins are active as quaternary complexes in which multiple polypeptide chains have associated (d).

The order and number of the amino acids residues in the polypeptide chain is called the primary structure of a protein and contains all necessary information to adopt the final three dimensional structures of the protein<sup>2</sup>. The secondary structure of the protein is determined by hydrogen bonding between the amide and carbonyl groups of the protein backbone and is identified in different folding patterns, i.e.  $\alpha$ -helices,  $\beta$ -sheets (Figures 1.1b, 1.2).

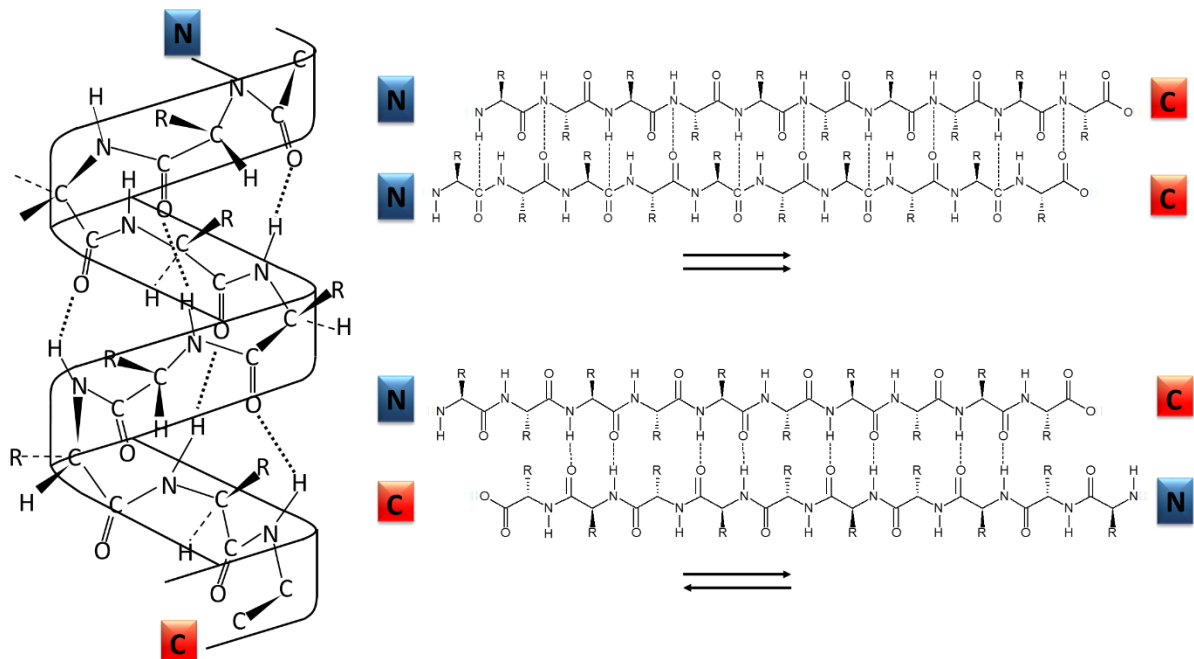


**Figure 1.2** Secondary structure elements of polypeptides. a)  $\alpha$ -helix, b) parallel  $\beta$ -sheet, and c) anti-parallel  $\beta$ -sheet. The N and C in the boxes corresponds to the N-terminus and C-terminus respectively. The dotted lines represent the hydrogen bonds. Arrows show the direction of the  $\beta$ -strands in the  $\beta$ -sheet secondary structures.

The typical  $\alpha$ -helix is a right-handed helix with 3.6 amino-acid residues per turn and each turn has a pitch of 5.4 Å. The N-H group of an amino acid forms a hydrogen bond with the C=O group of the amino acid four residues earlier, as shown in Figure 1.2a. The  $\beta$ -sheet secondary structure, like  $\alpha$ -helix, uses the full hydrogen-bonding capacity of its backbone, however, in this case, the bonds occur between neighboring polypeptide chains rather than a single chain. The direction of the chains categorize the  $\beta$ -sheet structure in two classes: Anti-parallel  $\beta$ -sheet and parallel  $\beta$ -sheet<sup>3</sup>.

Further compacting of the secondary structures into the global conformation of the polypeptide chain forms the tertiary structure (Figure 1.1c). For most proteins, the tertiary structure is the final conformation adopted to become fully activated, however if proteins with a tertiary structure associate, a quaternary protein structure is formed (Figure 1.1d)<sup>2</sup>.

### ***1.1.2 Intrinsically disordered proteins***

Proteins are considered to fold during their synthesis or immediately thereafter, and their function is assumed to be very closely related to their conformation. The structural characterization of the protein is considered key in understanding the biological role of these sequences. However, in the last few years, more and more of unstructured proteins have been discovered, and they are classified as intrinsically disordered proteins (IDPs)<sup>4-6</sup>. The IDPs are important components of the cellular signaling processes, allowing the same polypeptide to undertake different interactions with different consequences under different conditions<sup>7,8</sup>. Such IDPs can engage into non-functional intermolecular interactions and the proteins can aggregate into amorphous or amyloid-fibrils aggregates. Various IDPs without any sequence or conformational homology can form amyloid fibrils with similar characteristics<sup>9</sup>. This suggests that the main interactions within the fibril are made through the common protein backbone and not by the individual amino acid side chain residues, although these can influence the process. Amyloid fibrils are long, unbranched and often twisted structures with a diameter of 7-13 nanometers<sup>9,10</sup>.

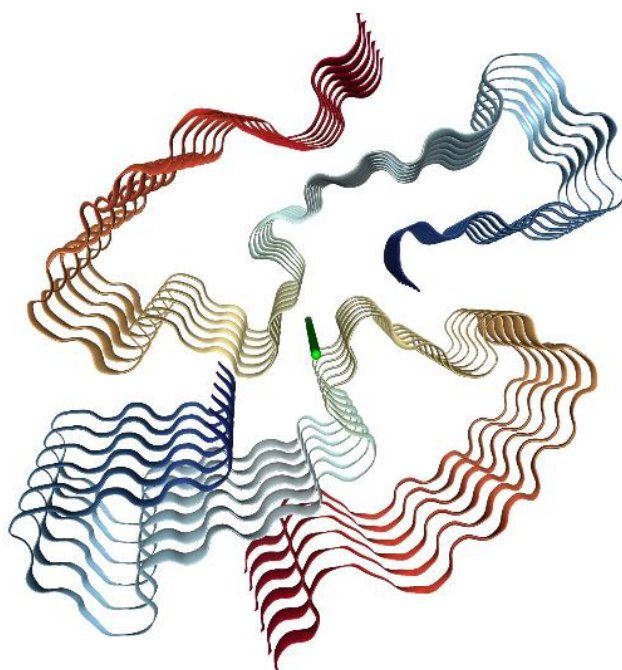


**Figure 1.3** Fibrillar structure of amyloid- $\beta$  (42) obtained from Cryo-EM. The peptide chains are colored in rainbows to show directionality of amino acids sequences. In the center the fibril axis is shown.<sup>11,12</sup>



Figure 1.3 shows that fibrils display typical cross- $\beta$  structure. The proteins are structurally organized as  $\beta$ -strands oriented perpendicular to the fibril axis, with hydrogen bonds running parallel to the long axis of the fibril. Individual molecules are stacked every 4.7 Å along the axis; parallel, in register and stabilized by hydrogen bonding<sup>12,13</sup>.

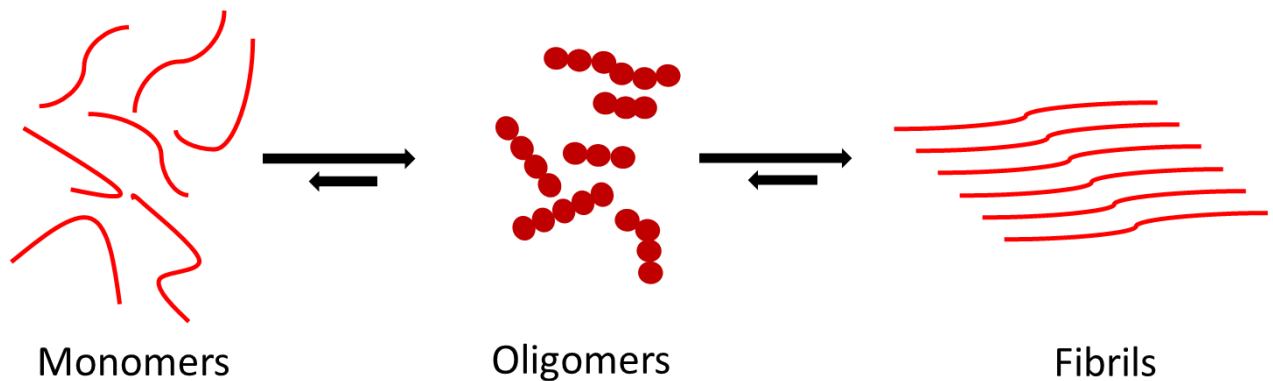


**Figure 1.4** Overall reaction pathway of amyloid aggregation shown schematically. Intrinsically disordered amyloid proteins in monomeric form (left), oligomer intermediates (shapes of oligomers are arbitrary), fibrils (right).

The aggregation of IDPs to fibrils is considered to be a key aspect to understand the development of neurodegenerative diseases. The protein aggregation process is represented in a simplified way in Figure 1.4. Oligomers are intermediate species between the monomeric and fibrillary forms of the protein, and recent research seems to show that they are the toxic species implied possibly in the destruction of the cell membranes<sup>14–20</sup>. The oligomer formation is a rather obscure state in the amyloid aggregation process. It is still challenging to study the properties of such species due to their transient nature. In this thesis, Chapter 2,3 and 4 focus on the development and utility of new methods to study the properties of oligomers in amyloid systems.

### 1.1.3 Alzheimer's disease: the amyloid $\beta$ peptide

Alzheimer's disease (AD) is the leading cause of dementia worldwide and more than 40 million people suffer AD. Clinically, AD is characterized by progressive cognitive impairment that inevitably leads to severe dementia, a stage marked by acute loss of almost all cognitive functions<sup>21–24</sup>. Biochemically and biophysically at the cellular level, AD is characterized by extracellular amyloid plaques and intraneuronal neurofibrillary tangles<sup>22,25,26</sup>. Amyloid plaques are extracellular deposits mainly build up from amyloid- $\beta$  (A $\beta$ ) peptides. The A $\beta$  peptide is the product of sequential proteolytic cleavage of the amyloid precursor protein, a transmembrane protein located in the neuronal membrane<sup>27</sup>. The predominant forms of A $\beta$  contain 40 or 42 amino acids, commonly identified as A $\beta$ 40 and A $\beta$ 42, respectively. The A $\beta$ 42 is more hydrophobic, has a higher propensity to form insoluble fibrils, and thus, is more abundant in plaques than A $\beta$ 40,

however such properties make A $\beta$ 42 more difficult to study at the early stages of the aggregation process than A $\beta$ 40. In vitro toxicity studies have demonstrated that the A $\beta$  assemblies are neurotoxic, but there is now general agreement that oligomers are the most pathogenic form of A $\beta$ <sup>28-31</sup>. The potent pathological effects of the A $\beta$  oligomers provide a compelling reason for the development of new methods to prevent their formation or to inhibit their activity. In Chapter 6 we study the effect of a potential drug inhibitor in the formation of A $\beta$  aggregates.

### ***1.1.4 Parkinson's disease: the alpha synuclein protein***

Parkinson's disease (PD) is the second-most frequent neurodegenerative disorder, which affects primarily the population above 60 years of age<sup>32</sup>. The most obvious symptoms in Parkinson's disease include resting tremor, muscular rigidity, depression and difficulty with walking<sup>33-35</sup>. A cure to PD is difficult to develop, because the symptoms of the disease are difficult to detect at the early stage of the disease. Parkinson's disease is characterized by the accumulation of a neuronal protein,  $\alpha$ -synuclein ( $\alpha$ S), in Lewy bodies plaques in the brain, which are the pathological hallmark of Parkinson's disease. Misfolding and aggregation of the  $\alpha$ S protein is accompanied by the loss of dopaminergic neurons in the *substantia nigra*, a region in the midbrain<sup>36</sup>. The  $\alpha$ S protein (40 kDa) consists of 140 amino-acid residues and is part of the IDP class<sup>4,5</sup>. The function of the  $\alpha$ -synuclein protein ( $\alpha$ S) is associated with its ability to bind to the membranes of intracellular vesicles and thought to involve membrane remodeling and vesicle trafficking. It mainly localizes at the synaptic terminus where it plays a role in synaptic transmission<sup>37</sup>. Under certain conditions in vitro (see Chapter 4 of this thesis),  $\alpha$ S forms oligomers and ultimately fibrils. Several works have shown that these oligomeric species are toxic to cells, and are related to the development of Parkinson's disease<sup>38,39</sup>. In Chapter 4 we investigate the aggregation kinetics of  $\alpha$ S from monomers to fibrils using EPR to observe the formation of oligomers in situ.

### ***1.1.5 Solid Phase Peptide Synthesis***

Solid phase peptide synthesis (SPPS) was invented by Merrifield in 1963 and it has become widely used in peptide synthesis<sup>40</sup>. Small solid resin beads, insoluble yet porous, are treated with functional linkers onto which peptide chains can be built. The peptide remains covalently attached to the bead until cleaved. The peptide is thus immobilized on the solid-phase and can be retained during a filtration process, whereas liquid-phase reagents and by-products of synthesis are flushed away as shown in detail in Figure 1.5.

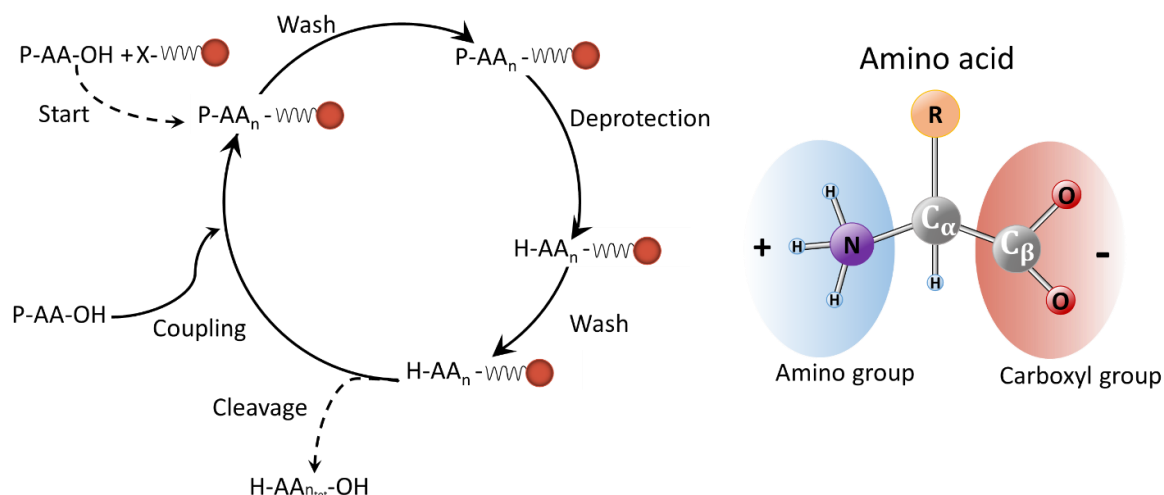


**Figure 1.5** The general process for synthesizing peptides on a resin. *Start*: The first amino acid ( $AA_n$ ,  $n = 1$ ), the C-terminal residue, gets attached to the resin through a linker. To prevent the polymerization of the amino acid, the amino group and the reactive side chains are protected with a temporary protecting group. Once the amino acid is attached to the resin, the resin is filtered and washed to remove byproducts and excess reagents. Next, the amino group protection is removed in a deprotection process and the resin is again washed to remove byproducts and excess reagents. Then the next amino acid is coupled to the attached amino acid ( $n + 1$ ), usually with the addition of activation reagents of the carboxyl group. This is followed by another washing procedure, which leaves the resin-peptide ready for the next coupling cycle. The cycle is repeated until the peptide sequence is complete ( $n = n_{tot}$ ). Then typically, all the protecting groups are removed and the peptide resin is washed, and the peptide is cleaved from the resin.

The coupling reactions can be driven to completion and high yields through the use of excess reagent. In this method, the amino acids are protected at all reactive functional groups. The order of functional group reactions can be controlled by the order of deprotection. To take note is that unnatural amino acids can be added to the sequence, as shown in Chapters 2, 3 and 6 of this thesis. Another main advantage of SPPS is the increased simplicity and speed of the entire process compared to in-solution synthesis.

## 1.2 Electron paramagnetic resonance

Electron paramagnetic resonance (EPR) is a powerful spectroscopic technique useful to study systems with at least one unpaired electron (paramagnetic species) such as organic and inorganic free radicals or transition metal ion complexes. Stable radicals like nitroxide radicals are widely used as spin probes in biological samples.

The EPR technique is a magnetic resonance spectroscopy, relying on the same concepts as NMR. The splitting of the electron-spin energy levels (Figure 1.6) is due to the presence of an external magnetic field ( $B_0$ ). The transitions between the energy levels can be induced by on-resonant microwave radiation. Two main categories of EPR experiments can be distinguished: continuous-wave (cw) experiments and pulsed EPR measurements. The extensive development of EPR techniques is providing new possibilities to get insights into the nature of the paramagnetic species and their surroundings. Here will be

given a brief overview of the basic principles of EPR. More details can be found for example in the monographies of Atherton and Brustolon<sup>41-43</sup>.

### ***1.2.1 Electron Zeeman interaction and g-factor***

When an electron is subject to an external magnetic field, the energy levels associated with its spin split up as a function of the magnetic field, see Figure 1.6. The quantum mechanical description of this phenomenon is given by the spin Hamiltonian ( $\mathcal{H}$ ) in eqn. (1.1):

$$\mathcal{H} = g_e \mu_B \mathbf{S} \cdot \mathbf{B} \quad (1.1)$$

where  $g_e = 2.0023$  is the g-factor of an isolated electron in vacuum,  $\mu_B$  is the Bohr magneton,  $\mathbf{B}$  is the external magnetic field, and  $\mathbf{S}$  is the electron spin operator. The magnetic field is oriented along one direction, conventionally  $z$ , so only the magnetic field  $B_0$  along that axis is taken into account, and therefore only the  $S_z$  component in the spin operator  $\mathbf{S}$  is considered. For a system that contains an electron spin  $S = \frac{1}{2}$ , the eigenvalues of  $S_z$  are  $m_s = \pm \frac{1}{2}$ , thus equation 1.1 can be rewritten as:

$$E_{\pm} = \pm \frac{1}{2} g_e \mu_B B_0 \quad (1.2)$$

which evidences the linear dependence of the splitting of the energy levels from the strength of the external magnetic field ( $B_0$ ), shown in Figure 1.6.

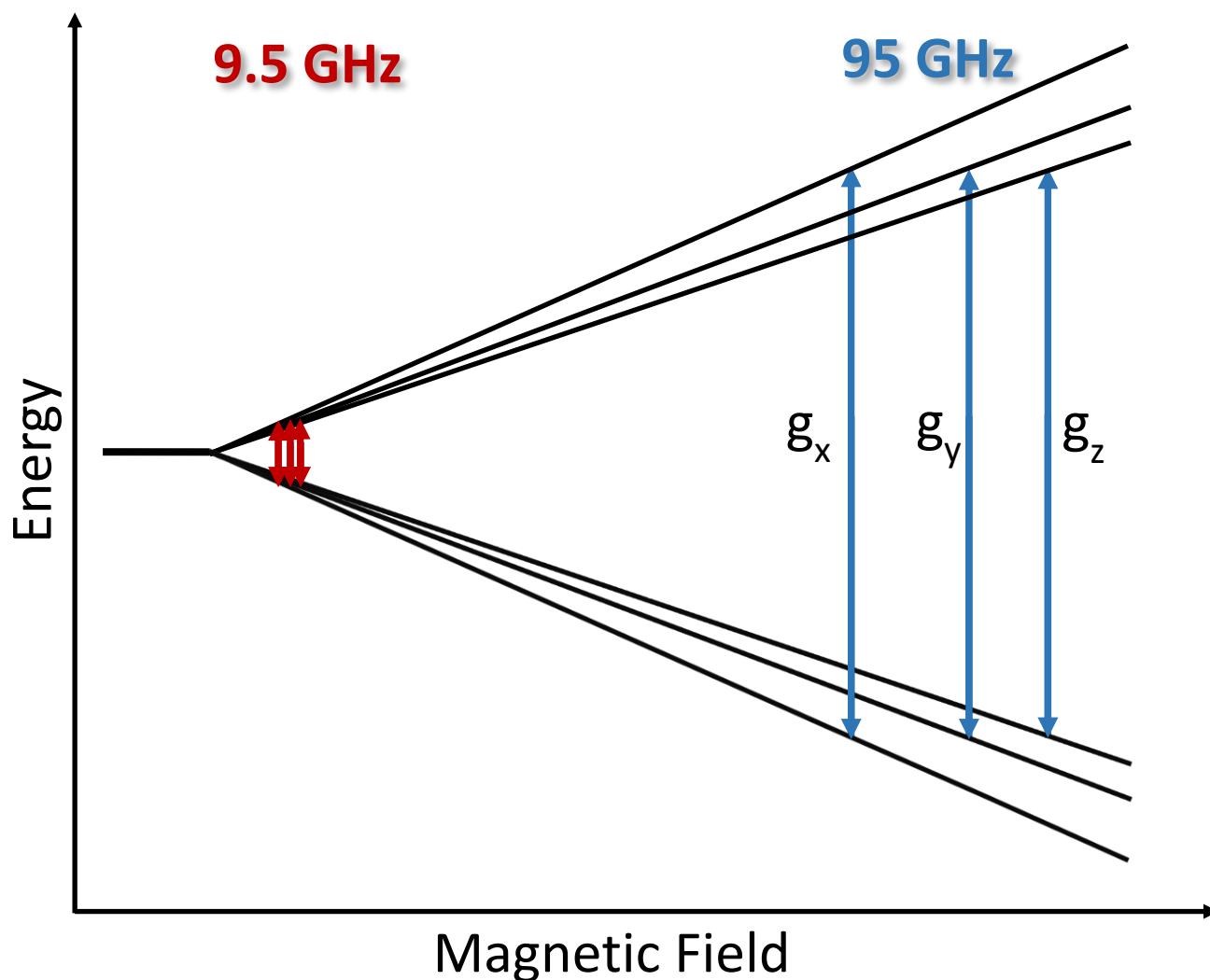


**Figure 1.6** Schematic representation of the electron spin energy levels (black lines) for a  $S = \frac{1}{2}$  system with anisotropic  $\mathbf{g}$  subjected to the Zeeman effect in the presence of an external magnetic field ( $B_0$ ). The red arrows and blue arrows represent the EPR transitions at lower and higher frequencies, respectively.

The splitting of the energy levels is proportional to the  $g$ -factor, a variable that is sensitive to the electronic properties of the molecule or ion the unpaired electron is part of, comporting a variation from  $g_e$ . The  $\mathbf{g}$  is a tensor and as such is anisotropic: The splitting of the energy levels depends on the orientation of the molecule or ion relative to the magnetic field direction. Figure 1.6 shows the splitting of the energy levels for an  $S = \frac{1}{2}$  system with an anisotropic  $\mathbf{g}$  tensor as a function of the magnetic field. At higher magnetic field the anisotropy of the  $\mathbf{g}$  tensor results in a larger separation of the transitions (arrows in Figure 1.6). This is an advantage of high-field EPR/high-frequency EPR compared to low-field EPR: In case of a small anisotropy of the  $\mathbf{g}$  tensor, only high-field EPR enables to resolve the transitions.

### 1.2.2 Electron spin – nuclear spin interaction: hyperfine interaction

The interaction between nuclear spin(s) and the applied magnetic field is analogous to the electron Zeeman (EZ) interaction, however its magnitude is only 1/658 of the EZ interaction due to the fact that the magnetic moment of a nuclear spin is much lower than the magnetic moment of an electron spin. In addition to the Zeeman interactions, one important aspect about spins is that they can interact with each other. The interaction between the magnetic dipoles of unpaired electrons and surrounding nuclei is called *hyperfine interaction*, and it is an important source of chemical information in EPR. The resulting spin Hamiltonian can be expressed as:

$$\mathcal{H} = g_e \mu_B \mathbf{S} \cdot \mathbf{B} - g_N \mu_N \mathbf{I} \cdot \mathbf{B} + \mathbf{S} \cdot \mathbf{A} \cdot \mathbf{I} \quad (1.3)$$

where  $g_N$  represents the nuclear g-factor and  $\mu_N$  is the nuclear magneton. The hyperfine interaction is given by the tensor  $\mathbf{A}$  that consists of two contributions: The isotropic part and the anisotropic part, namely  $\mathbf{A} = A_{iso} + \mathbf{T}$ .

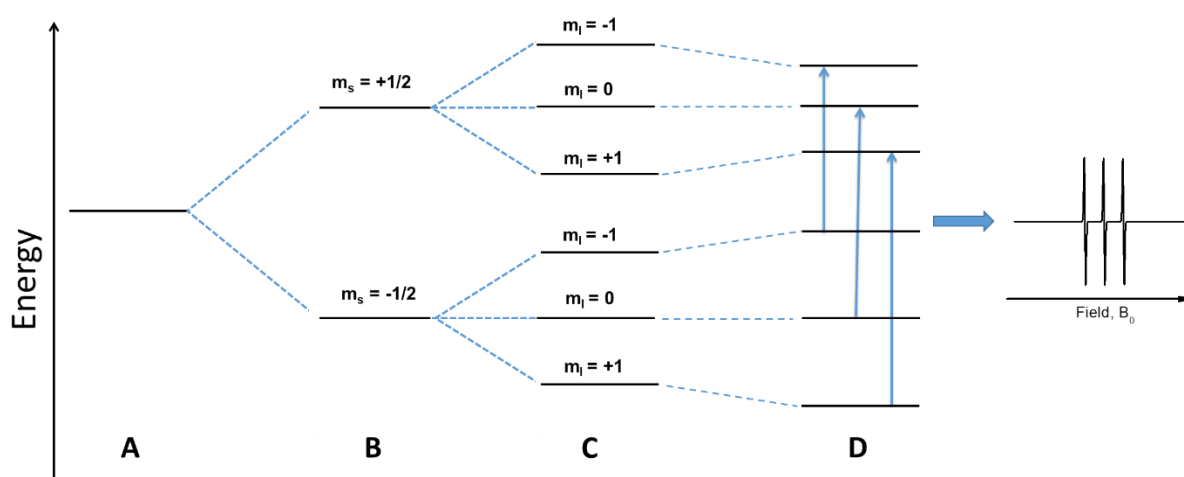


**Figure 1.7** Schematic energy levels representing the effects of the spin Hamiltonian of eq.1.3 for an electron with spin  $S = 1/2$  and its interaction with a nuclear spin  $I = 1$ . (A) When there is no external magnetic field the spin states  $m_s = 1/2$  and  $m_s = -1/2$  are degenerate. (B) In the presence of an external magnetic field, the electron Zeeman interaction separates the energy levels of the two spin states. The g-factor is considered isotropic. (C) Another splitting of the energy levels is caused by the nuclear Zeeman interaction, which creates a separation of the energy levels of the nuclear spin states  $m_I = -1$ ,  $m_I = +1$  and  $m_I = 0$ . (D) The hyperfine interaction between the electron spin and nuclear spin (considered isotropic) causes another shift of the energy levels by an amount defined by the hyperfine tensor  $\mathbf{A}$ . The possible three transitions are shown by arrows, and the resulting EPR spectrum is shown on the right.

Figure 1.7 shows the corresponding energy level scheme for a nitroxide radical, which contains an electron spin ( $S = 1/2$ ) and a nitrogen nuclear spin ( $^{14}\text{N}$ ,  $I = 1$ ). The splitting of the energy levels is due to the electron Zeeman (EZ) interaction (Figure 1.7B), also the nuclear spin splitting (NZ) must be taken into account, so that each of the energy levels are further split according to the magnetic quantum numbers of the nuclear spin. As a last step, Figure 1.7D shows how the hyperfine interaction terms applies on the formed sublevels, shifting them by an amount defined by the hyperfine tensor  $\mathbf{A}$ .

For anisotropic  $\mathbf{g}$  and  $\mathbf{A}$  tensors, the orientation of the magnetic field with respect to the molecular system or ion must be taken into account. The  $\mathbf{g}$  tensor is characterized by three principal values,  $g_{xx}$ ,  $g_{yy}$ , and  $g_{zz}$ , each corresponding to a particular orientation of the molecule in the magnetic field  $B_0$  as shown in Figure 1.8 for a nitroxide radical. The principal values of the tensor  $\mathbf{A}$  are  $A_{xx}$ ,  $A_{yy}$  and  $A_{zz}$ . For nitroxide spin labels the difference between  $A_{xx}$  and  $A_{yy}$  is small and the hyperfine tensor can be considered to be axially symmetric. The value of  $A_{zz}$  is highly sensitive to the polarity of the environment and can give precious information about the surroundings of the spin label<sup>44</sup>.

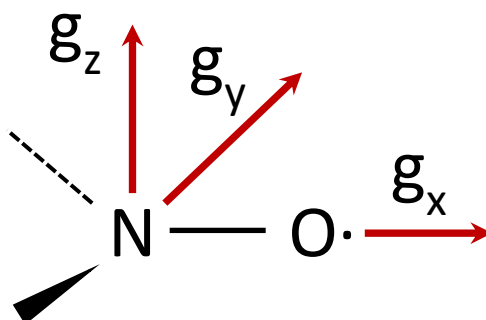


**Figure 1.8** Structure of a nitroxide radical. The unpaired electron (black dot) localizes on the N-O bond. Principal directions of the  $\mathbf{g}$  tensor are shown (red arrows).

### 1.2.3 Spin-label EPR

Spin labels are paramagnetic probes that can be attached to systems that do not contain a paramagnetic center. In nature, most bio-macromolecules do not contain paramagnetic centers, therefore they are EPR silent. With the development of site-directed spin labeling<sup>45–47</sup>, EPR has become a powerful technique to investigate local structure and dynamics of proteins, to map distances between amino acid residues in polypeptides, and to understand the three-dimensional structure of bio-macromolecular complexes.

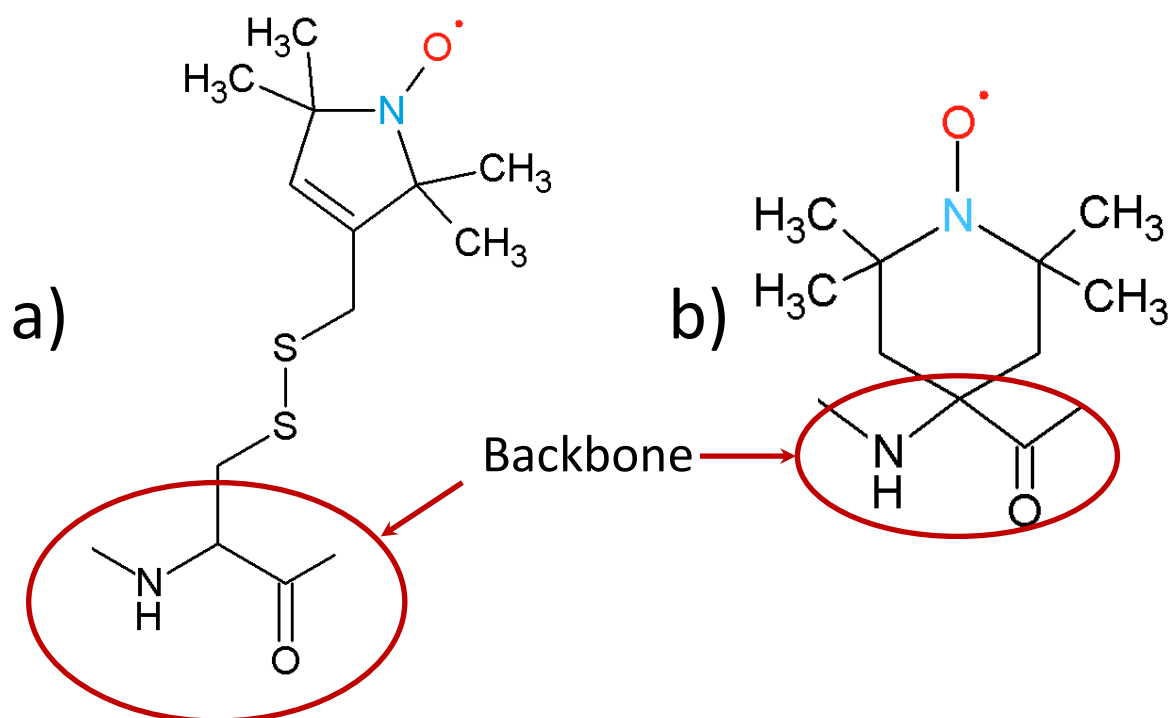


**Figure 1.9** a) Molecular structure of the MTSL spin label attached to a cysteine side-chain. b) Molecular structure of the TOAC spin label. The backbone of the peptide is shown as well.

The most commonly used spin labels are nitroxide derivatives with a stable unpaired electron. The stability of the nitroxide radical is mostly given by the steric effect of the methyl groups adjacent to the nitroxide. Figure 1.9 shows the structure of the two nitroxide spin labels used in the research described in this thesis: the MTSL spin label [(1-oxyl-2,2,5,5-tetramethylpyrroline-3-methyl)-methanethiosulfonate], and the TOAC spin label (2,2,6,6-tetramethyl-N-oxyl-4-amino-4-carboxylic acid). The MTSL spin label attaches to a protein by a covalent bond between the -SH group of the cysteine and the methanethiosulfonate of MTSL, whereas the TOAC spin label is placed directly into the backbone of the protein.

#### 1.2.4 Spin-label dynamics: The rotational correlation time

The cw-EPR in solution experiments on nitroxides are sensitive to the mobility of the label with respect to the external magnetic field, which gives rise to changes in the shape of the EPR spectrum. Any dynamic process on the timescale determined by the **g** and **A** tensor anisotropy affects the shape of the lines, giving information related to the structure and mobility of the protein<sup>45–47</sup>. The rotational motion of the paramagnetic species is characterized by the *rotational correlation time* ( $\tau_r$ ), which is the average time it takes for a molecule to rotate one radian, i.e. the longer  $\tau_r$  the lower is the mobility of the nitroxide.



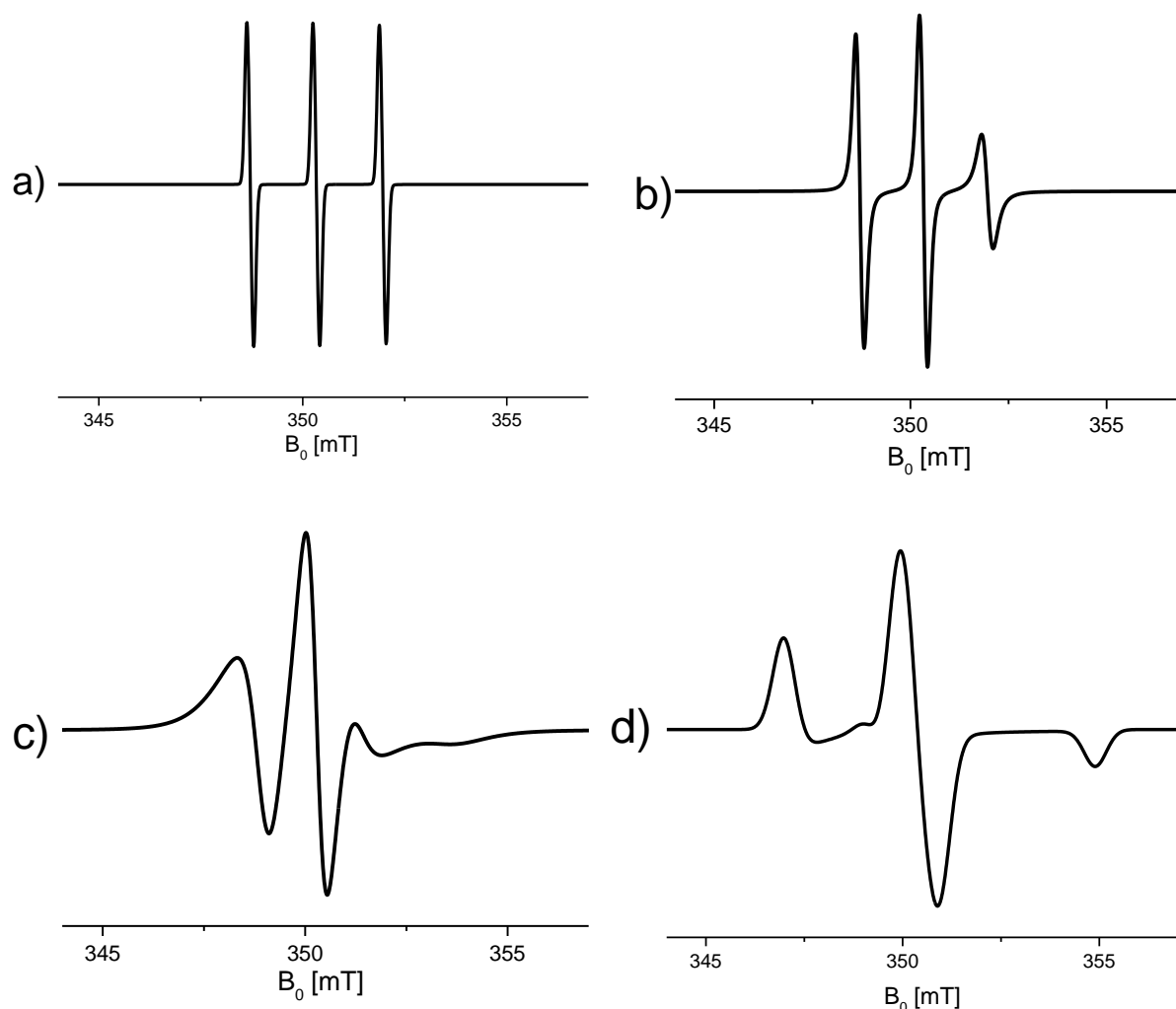


**Figure 1.10** Simulated cw-EPR spectra to show the effect of the rotational correlation time of a nitroxide spin label on the lineshape of the spectra. a)  $\tau_r = 0.003$  ns, b)  $\tau_r = 0.5$  ns, c)  $\tau_r = 3.16$  ns and d) frozen solution. The spectra a) and b) were simulated with the algorithm “garlic”, c) with the algorithm “chili” and d) with the algorithm “pepper” using EasySpin<sup>48</sup>. The  $\mathbf{g}$  tensor is [2.0086 2.0059 2.0020], and the hyperfine tensor is [13 13 110.7] MHz. The linewidth parameter for a), b), c) spectra is 0.12 mT, and for spectrum d) is 0.65 mT.

Figure 1.10 shows the effect of the mobility of the spin label on the lineshape of the EPR spectra by a set of simulations. If the radical is completely free to move in solution the EPR spectrum has three narrow lines as shown in Figure 1.10a. The lines are spaced by the isotropic nitrogen hyperfine interaction ( $A_{iso}$ , see subsection 1.2.2), which is due to the hyperfine interaction of the unpaired electron ( $S = \frac{1}{2}$ ) with the  $^{14}\text{N}$  nuclear spin ( $I = 1$ ). With increasing  $\tau_r$  the linewidth and intensity starts to vary: The slower the motion ( $1 < \tau_r < 10$  ns), the broader the lines become, and the less intense the high field and low field lines appear (Figure 1.10 b,c). In the slow-motion regime the lines start to change position. For slow motion ( $\tau_r > 10$  ns), the spectrum approaches that of a completely immobilized spin label and the anisotropy is fully observable (Figure 1.10d). In Chapters 2,3,4 and 6 of this thesis, we have used the lineshape changes in nitroxide-spin-label spectra to identify the formation and structure of amyloid systems.

### ***1.2.5 Distance determination by EPR: Dipole-dipole interaction***

An important part of modern EPR is the structure determination of biological systems, which is based upon the measurement of the distances between spin-labels. Such distances are derived from the dipole-dipole interaction between the unpaired electrons of the spin-labels. The dipole-dipole interaction ( $\nu_{dd}$  in MHz units) between two spins, A and B, is inversely proportional to the cube of the distance and is given by:

$$\nu_{dd} = -\frac{\mu_0 \hbar}{8\pi^2} \frac{g_A g_B}{r_{AB}^3} (3\cos^2\theta - 1) \quad (1.4)$$

where  $\mu_0$  is the magnetic permeability in vacuum,  $g_A$  and  $g_B$  are the isotropic g factors of the two spins A and B,  $\hbar$  is the reduced Planck's constant,  $r_{AB}$  is the distance between the two spins, and  $\theta$  is the angle between the magnetic field and the vector that connects the two spins.

### ***1.2.6 Double electron-electron resonance***

The double electron-electron resonance (DEER) technique, also called pulsed electron double resonance (PELDOR), is a method to measure the dipole-dipole interaction between unpaired electrons for distances larger than 2 nm (Figure 1.11a). This technique allows the detection of the modulation of the echo intensity, which is caused by the dipole-dipole interaction between spins.<sup>49</sup>

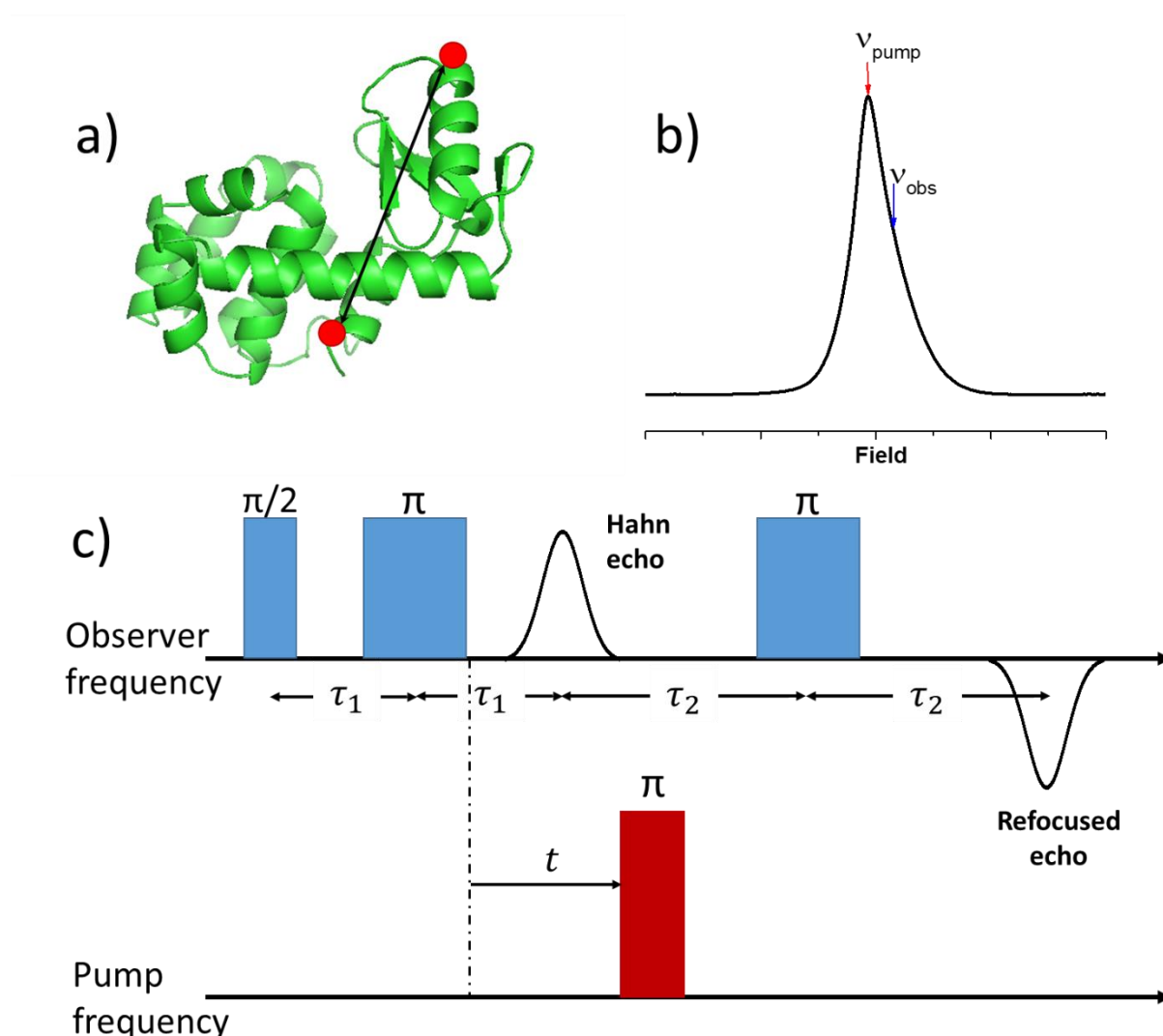


**Figure 1.11** Schematic representation of double electron-electron resonance (DEER) spectroscopy. A) Protein with two spin labels A and B (red dots). b) Field swept Hahn echo of a Gd(III) spin tag. Arrows show the frequency positions for the observer and pump pulses. c) Pulse sequence of the DEER experiment consisting of the refocused echo sequence at the observer frequency ( $\nu_{\text{obs}}$ ) and the pump pulse at the pump frequency ( $\nu_{\text{pump}}$ ). The delay times  $\tau_1$  and  $\tau_2$  are fixed. The delay time  $t$  varies and we follow the variation of the amplitude of the refocused echo in function of  $t$ .

The pulse sequence of a standard DEER experiment is shown in Figure 1.11c. Two different microwave frequencies are applied (Figure 1.11b), the so-called pump and observer frequencies. At the observer frequency three pulses are employed to selectively monitor a refocused echo of one of the paramagnetic centers (A). The  $\pi/2$  and  $\pi$  pulses rotate the magnetization of the spins by  $90^\circ$  and  $180^\circ$  respectively, resulting in a refocused echo (Figure 1.11c). An additional inversion pump pulse ( $\pi$ ) between the second and third pulse at the observer frequency is applied with a frequency resonant with the second paramagnetic center (B) that selectively flips the spin B. This stimulated spin-flip induces a sudden change in the precession rate of the magnetization of spin A which leads to a nonperfect refocusing of the A spins, as a function of the dipolar coupling

between spins A and spins B ( $\nu_{dd}$ ). By variation of the time at which the inversion pulse is applied, the dephasing of the magnetization of spin A is changed to induce a periodic modulation of the A-spin refocused echo intensity, which is called the DEER time trace (Figure 1.12a). Applying the Fourier Transformation to the DEER trace, a Pake Pattern is obtained from which the dipolar coupling frequency ( $\nu_{dd}$ ) can be extracted as shown in Figure 1.12b.

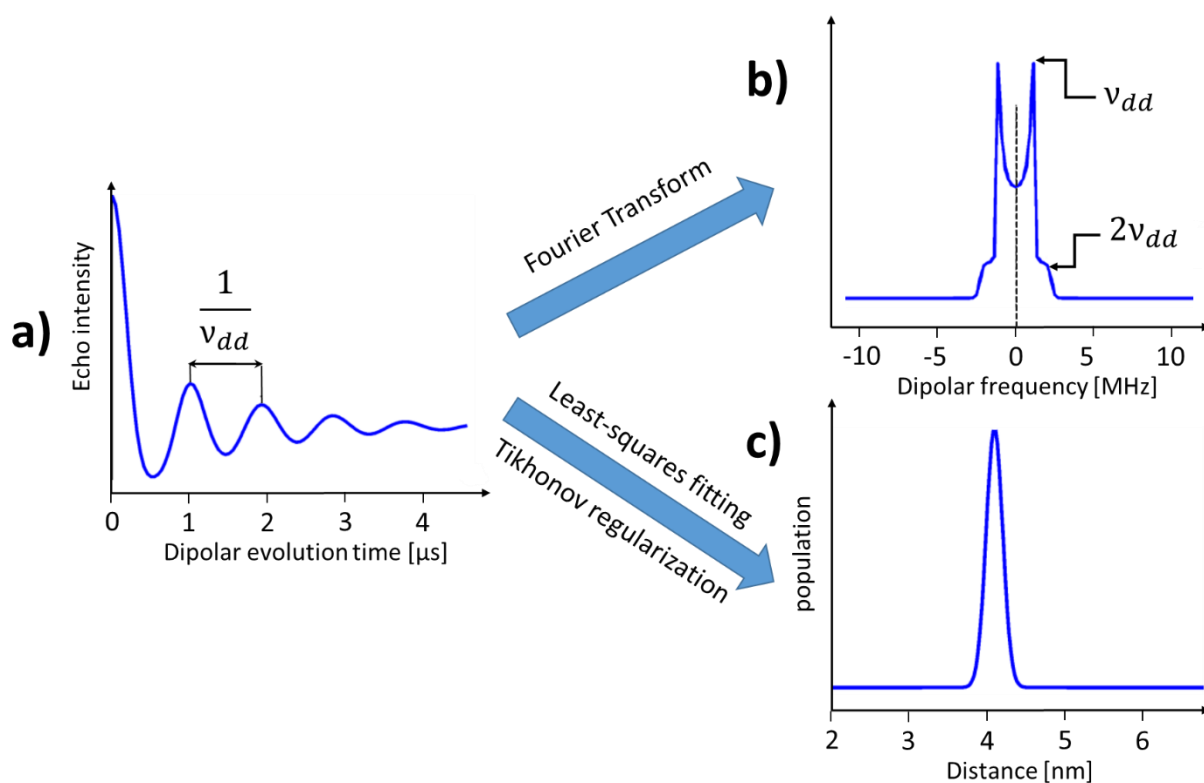


**Figure 1.12** Data analysis of a DEER trace. a) Model of a DEER trace with dipolar coupling modulation after background correction. b) Fourier transformation (Pake Pattern) of the DEER trace with peaks at  $\pm \nu_{dd}$  and edges at  $\pm 2\nu_{dd}$ . c) Distance distribution obtained by Tikhonov regularization.

Due to the flexibility of the macromolecules and conformational freedom of the spin label, the distance between spins varies in a certain range. In the case of proteins often broad distance distributions result. The overall signal of a DEER trace shows the superposition of modulations at different frequencies, rather than a single frequency. Other approaches for the analysis are regularization methods or model-based approaches, by which the distance distributions are directly fitted to the DEER time traces (Figure 1.12c)<sup>50–53</sup>. In this thesis we used the Tikhonov regularization approach.

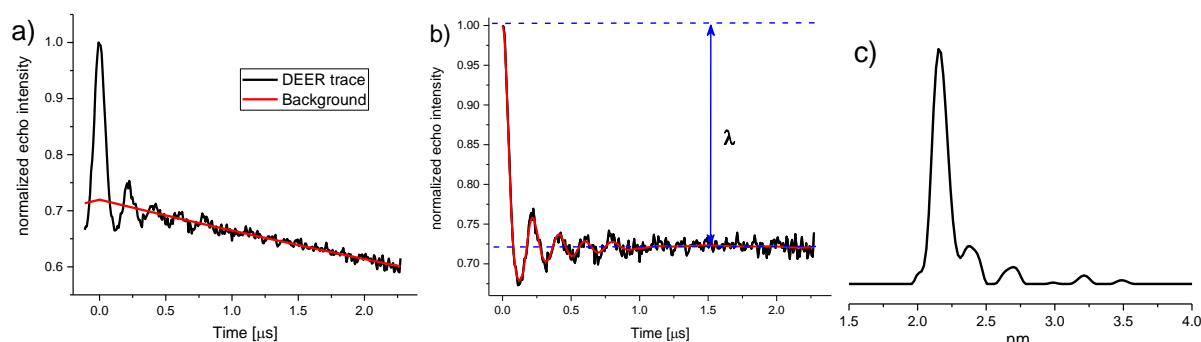


**Figure 1.13** Analysis steps of DEER time traces on a rigid doubly labeled system. a) Raw DEER time trace. Red line: Background fit. b) Background corrected DEER time trace. Red: Fitting of the modulation. Blue arrow: modulation depth ( $\lambda$ ). c) Distance distribution obtained by Tikhonov regularization method<sup>54</sup>. Small features are probably artifacts.

To determine the distance distribution between the two paramagnetic centers within the same molecule, the effects of the interaction of the spins within the same molecule must be separated from the contribution of the intermolecular interaction of the spins (background). The subtraction of the background is shown in (Figure 1.13b). The amount of coupled spins compared to the total echo intensity is given by the modulation depth ( $\lambda$ ), as shown in Figure 1.13b. The spin-spin distance obtained from the analysis of the DEER trace, shown in Figure 1.13c, represents the distribution of the distances between the paramagnetic centers obtained by Tikhonov regularization. The width of such distribution is directly related both to the flexibility of the labeled macromolecules and to the conformational freedom of the paramagnetic centers<sup>55,56</sup>.

### 1.3 Thesis outline

In Chapters 2 and 3, continuous wave (cw) EPR is employed to investigate the influence of the backbone attached TOAC spin labels on the aggregation of the amyloid peptides and its possible uses to study the structure and properties of amyloid oligomers. In Chapter 4, we examine the kinetics of aggregation of the spin-labeled  $\alpha$ S protein by continuous wave (cw) EPR. In Chapter 5 we investigate with pulsed EPR the properties of three recently developed Gd(III) labeling tags. In the final Chapter we present the EPR characterization on how TOAC influences the aggregation of A $\beta$ , and we apply it to investigate the effects of a recently discovered inhibitor of A $\beta$  aggregation.



## **2 Synthesis and first CD and EPR characterization of small amyloid peptides designed to form oligomers**

Electron Paramagnetic Resonance (EPR) is a powerful tool to study peptides. The use of 2,2,6,6-tetramethyl-N-oxy-4-amino-4-carboxylic acid (TOAC) as a spin label that incorporates directly into the backbone of peptides, is advantageous to determine peptide backbone motion. In this study we report the synthesis of three TOAC peptides modeled after K11V (KVKVLGDVIEV), an amyloid peptide that self-aggregates to oligomers with a  $\beta$ -sheet configuration [Laganowsky, A. *et al.*, *Science* **335**, 1228–1231 (2012)]. By Solid Phase Peptide Synthesis (SPPS), we prepared T0EZ with the TOAC (**Z**) at the N-terminus (**Z**KVKVLGDVIEVGG), T5EZ (KVKV**Z**GDVIEVG) and T12EZ (KVKVLGDVIEV**Z**G). We checked the aggregation propensity at room temperature in liquid solution by continuous-wave EPR and Circular Dichroism. Only T0EZ aggregates similarly to K11V; T5EZ and T12EZ do not. This suggests that TOAC at specific positions inhibits aggregation, implying that its position must be chosen carefully to avoid modifications in the properties of the peptide.

## 2.1 Introduction

Electron Paramagnetic Resonance (EPR) is increasingly used to understand the structure and behavior of proteins and peptides, see for example,<sup>47,50,57–59</sup> amongst which the difficult to study class of Intrinsically Disordered Proteins<sup>60,61</sup>, for example in relation to amyloid aggregation.<sup>61–66</sup>

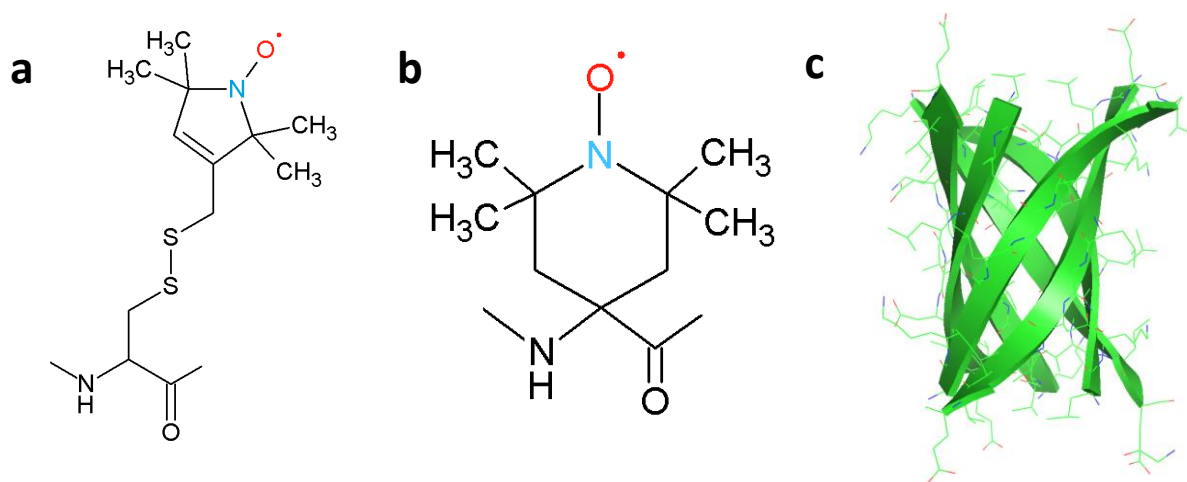


**Figure 2.1** (a) Chemical structure of MTSL attached to the Cys amino acid. (b) Chemical structure of the TOAC amino acid. (a) Ribbon configuration of the oligomer of K11V obtained by X-Ray crystallography<sup>67</sup>

To apply EPR, the protein or peptide of interest has to be spin labelled. For globular and membrane proteins the site-directed spin-label method, in which a nitroxide spin label is attached via a cysteine to the protein backbone (see Figure 2.1a),<sup>45,47,59,68,69</sup> is almost universally applied. For small peptides, the intrinsic flexibility and the long linker length of these common spin labels can be problematic. Several more rigid spin labels were proposed.<sup>70–74</sup> For peptides, the backbone-fixed  $\alpha$ -amino acid TOAC (Figure 2.1b), in which the motion of the nitroxide is closely coupled to the peptide backbone motion, is the most promising approach.<sup>63,75–83</sup> The TOAC label follows the peptide motion more faithfully than the cysteine-linked labels and therefore it would be better suited for studying the peptide behavior. Synthesis of TOAC labeled peptides can be performed by Solid Phase Peptide Synthesis (SPPS),<sup>40,84–89</sup> or organic synthesis methods.<sup>76–81,90–93</sup>

To test the suitability of TOAC in the study of amyloid-peptide aggregation, we chose the K11V peptide as a model. This peptide was shown to form stable oligomers as shown in Figure 2.1c

Here we describe the SPPS of three variants of the K11V peptide, containing the TOAC spin label in three different positions. The original K11V sequence was expanded with Glycines at the C-terminus to facilitate the synthesis, generating the “new” wild-type K13G.



## Chapter 2

To determine the aggregation propensity, we use liquid solution, room-temperature continuous-wave EPR (cw EPR). This method is sensitive to nano-second rotational motion of the nitroxide and detects aggregation by broadening of the lines of the spectrum.<sup>62,90–93</sup> Also Circular Dichroism (CD) is sensitive to aggregation, because the monomers convert from random coil to  $\beta$ -sheet oligomers (for more details, see SI). Both forms have a characteristic CD signature.<sup>94</sup>

In this chapter we report the synthesis and initial characterization of the TOAC peptides. We show that the peptide with an N-terminal TOAC aggregates similarly to the wild type, whereas the other two do not aggregate.

## 2.2 Results

**Table 2.1** Sequences of the peptides used and aggregation properties. TOAC (2,2,6,6-tetramethyl-N-oxyl-4-amino-4-carboxylic acid): position 0 for T0EZ, position 5 for T5EZ, position 12 for T12EZ. Aggregation determined by CD and EPR.

peptide	sequence	aggregation by CD	aggregation by EPR
K11V	K V K V L G D V I E V	-	-
K13G	K V K V L G D V I E V G	G YES	-
T0EZ	TOAC K V K V L G D V I E V G	G YES	YES
T5EZ	K V K V TOAC G D V I E V G	NO	NO
T12EZ	K V K V L G D V I E V TOAC G	NO	NO

Table 2.1 shows the peptide sequences. The original sequence of K11V is the model for the spin-labelled peptides.<sup>67</sup> We prepared the three TOAC variants (T0EZ, T5EZ, T12EZ) with acceptable yields and high purity. The coupling of the bulky TOAC was done under special conditions: The amount of the precursor was adjusted, a different activator (1-Bis(dimethylamino)methylene]-1H-1,2,3-triazolo[4,5-b]pyridinium 3-oxid hexafluorophosphate) (HATU) was applied and a longer coupling time was allowed (see

SI); the variants we synthesized also differ from K11V by the Glycine residues at the C-terminal part of the sequence, introduced to facilitate the synthesis.

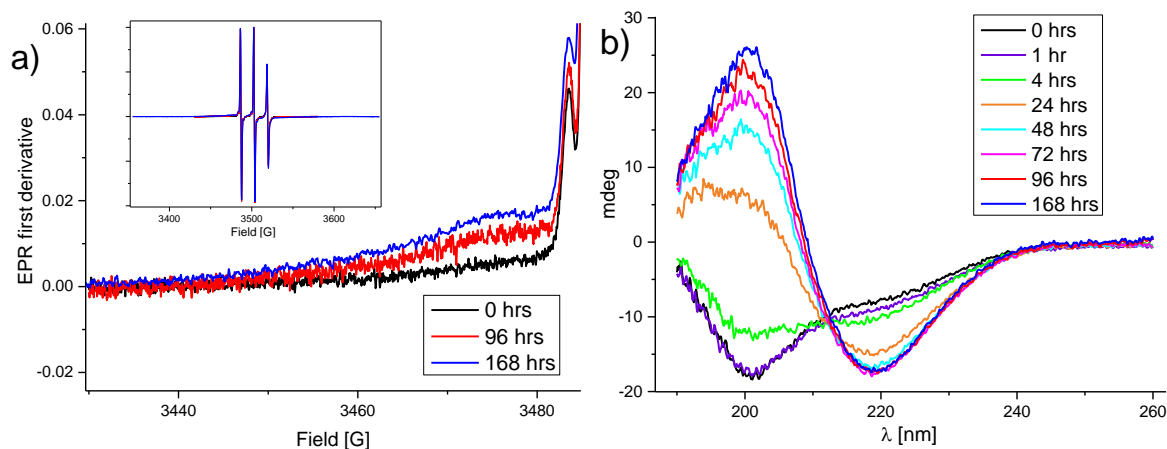


**Figure 2.2** (a) The 9 GHz spectra of T0EZ for three different aggregation times. The spectra are normalized to the maximum intensity (central line). The insert shows the full field-sweep spectra characterized by the usual three lines (derivative) for a nitroxide radical in solution; the main image shows the enlarged version of the low-field part of the spectra. At  $B_0 = 347.7$  mT : broad peak, for details see text. (b) The CD spectra of T0EZ at different aggregation times.

Figure 2.2 shows the cw-EPR and CD spectra of T0EZ for different aggregation times. Figure 2.2a focuses on the low-field region of the EPR spectra, where the changes are most obvious, the full spectra are shown as an insert. The intensity of the broad peak at 347.7 mT increases with the time of aggregation, while the intensity of the narrow lines decreases relative to that of the broad peak. The broad peak indicates the formation of T0EZ aggregates as described in the discussion.

Figure 2.2b shows the CD spectra taken during the aggregation of the same sample (see SI). At time zero the spectrum has a minimum at 201 nm, showing that the majority of the peptide is in a random-coil configuration. With increasing aggregation time, the minimum at 201 nm disappears and is replaced by a maximum at the same position. This newly developed maximum is characteristic for a  $\beta$ -sheet structure<sup>94</sup>.

The same experiments were conducted for the other two TOAC peptides (T5EZ and T12EZ). The EPR spectra for both of them presented no visible broad peaks and were devoid of changes when the sample was subjected to the conditions under which the T0EZ spectra changed. The CD spectra at time zero showed two minima at 201 nm and 219 nm, similar to the time zero spectrum of T0EZ. The shape of the CD spectra did not change over time.

## 2.3 Discussion

We have investigated a set of spin-labelled peptides that resemble the K11V peptide. The purpose of our research was to check if the variants containing the TOAC spin label could be synthesized and if they still retained their aggregating behavior. All three variants were synthesized by Solid Phase Peptide Synthesis without problems. We used preloaded resins containing Glycine to facilitate the first couplings, which results in C-terminal Glycines in the sequence. The presence of TOAC didn't significantly reduce the yield of the reaction.

One of the peptides, T0EZ, showed aggregation, according to measurements by means of EPR and CD. Aggregates show up as a broad peak in the EPR spectra, reflecting the increased rotational correlation time of the oligomers as compared to the monomers. The intensity of the broad peak increases with time, showing that the amount of aggregates increases during the aggregation time. The changes in the CD spectra are also fully consistent with the aggregation: the transition of the random coil monomers to  $\beta$ -sheet oligomers, presumably similar to the oligomers shown in Figure 2.1c, is clearly seen in the development of the CD spectra.

As T5EZ and T12EZ showed none of the spectral changes observed for T0EZ we conclude that these peptides do not aggregate. To explain why T5EZ does not aggregate, we note that in the oligomer (Figure 2.1c) the TOAC would end up in the middle of the  $\beta$ -strands of the oligomer (see Figure 2.1c). Given that TOAC has a known propensity to induce  $\alpha$ -helices or  $3_{10}$  helices,<sup>83,93</sup> and the oligomer has a  $\beta$ -sheet structure, TOAC in that position may well interfere with oligomer formation. In addition, the TOAC residues of adjacent peptides could come close to each other in the oligomers, further inhibiting oligomer formation. The absence of aggregation in the T12EZ samples is more difficult to explain and needs to be investigated further.

We demonstrated that TOAC can be introduced at specific positions of the peptide sequence using SPPS, and that, for the oligomer formation intended here, the place must be chosen carefully not to alter the properties of the peptide. We show that EPR, combined with CD, is a powerful tool to study of the aggregation of such peptides.

## 2.4 Supporting information

### 2.4.1 Synthesis and Characterization of Peptides

All chemicals were commercial products of the best quality available and, unless otherwise indicated, they were used without any further purification. The K13G peptide was purchased from tebu-bio (Heerhugowaard, The Netherlands).

9-Fluorenylmethoxycarbonyl(Fmoc)-amino acids, Fmoc-Gly-Wang Tentagel resin and the other chemicals used for the solid phase peptide synthesis were purchased from Sigma Aldrich. 2,2,6,6-Tetramethylpiperidine-N-oxyl-4-(9-fluorenylmethyloxycarbonyl-amino)-4-carboxylic acid (Fmoc-TOAC-OH) and H-Gly-Wang resin were supplied by Iris Biotech (Germany).

The peptide sequences were assembled on AB433A Peptide Synthesizer, using (0.05 mmol) of Gly-Wang resin (substitution 0.5 mmol/g). For all amino acids except TOAC we use 5 equivalents (0.25 mmol) of each AA for the synthesis. Fmoc deprotection is done 4 times (3 minutes each) by adding (2.5 mL) of a solution of 20 % piperidine (PIP) in N-methylpyrrolidone (NMP). Couplings were performed using *2-(6-Chloro-1H-benzotriazole-1-yl)-1,1,3,3-tetramethylaminium hexafluorophosphate* (HCTU) as an activator and N,N-Diisopropylethylamine (DIPEA) as base. We used 1 equivalent of HCTU and 2 equivalents of DIPEA for 1 equivalent of AA. 1 mL of a solution (0.25 M) of HCTU, (0.5 mL) of a solution 1 M of DIPEA and (0.5 mL) of NMP are added to the resin for the coupling reactions. Each coupling reaction lasted 2 hrs.

The TOAC spin label was treated differently. Only 2 equivalents of AA were added for 1 equivalent of resin. Instead of HCTU, (1-[Bis(dimethylamino)methylene]-1H-1,2,3-triazolo[4,5-b]pyridinium 3-oxid hexafluorophosphate) (HATU) was used as activator and (400  $\mu$ L) of its solution (0.5 M) were put directly inside the cartridge with the spin label together with (600  $\mu$ L) of NMP. The coupling in this case lasted 4 hrs.

For the AA introduced immediately after the TOAC we used a double coupling, keeping the same conditions as for the rest of the sequence. The Fmoc absorption at 301 nm was followed to check the status of the synthesis after each coupling.

At the end of the synthesis the resin was dried by washing it with dichloromethane (DCM). To cleave the peptide from the resin (2 mL) of a solution 95% trifluoroacetic acid + 5% water was used. A small amount of peptide was cleaved from the resin and characterized by LC-MS.

Unless otherwise indicated, the peptides were purified by semi-preparative HPLC.

Analytical HPLC separation was carried out on a LCQ Advantag Thermo Finnigan LC-MS system with UV-Vis and Ion-trap mass detectors. The column used was a C-18 Gemini (4.6

## Chapter 2

x 50 mm, 3  $\mu$ m particle size) from Phenomenex. The mobile phase A ( $H_2O$ ) and B (acetonitrile, MeCN) and C (aqueous 1 % Trifluoroacetic acid, TFA) were used for preparing binary gradients. Elution condition: A 72 % B 18 % C 10 %, linear gradient B 18-33 % in 10 min. Flow rate 1 mL/min.

Crude peptide purifications were performed on a Gilson HPLC preparative system from Phenomenex with a semipreparative Gemini C<sub>18</sub> column (10 x 250 mm) with UV-Vis detector. The mobile phase A ( $H_2O$ ) and B (acetonitrile, MeCN) and C (aqueous 1 % Trifluoroacetic acid, TFA) were used for preparing binary gradients. Elution condition: A 82 % B 18 %, linear gradient B 18-33 % in 10 min, Flow rate 5 mL/min.

The lyophilization was done on a Christ Alpha 2-4 LO lyophilizer with a Christ RVC 2-25 rotor.

All TOAC peptides had a high level of purity.

T5EZ: yield 2.0%; LC-MS (C<sub>18</sub>)  $t_R$  4.56 min; purity > 95%; Mass: calculated for C<sub>61</sub>H<sub>108</sub>N<sub>15</sub>O<sub>18</sub> [M+H]<sup>+</sup> 1339.61, found: 1339.47

T0EZ: yield 10.8%; LC-MS (C<sub>18</sub>)  $t_R$  4.68 min; purity > 95%; Mass: calculated for C<sub>69</sub>H<sub>122</sub>N<sub>17</sub>O<sub>20</sub> [M+H]<sup>+</sup> 1453.794, found: 1453.53

T12EZ: yield 1.4%; LC-MS (C<sub>18</sub>)  $t_R$  4.85 min; purity > 95%; Mass: calculated for C<sub>69</sub>H<sub>122</sub>N<sub>17</sub>O<sub>20</sub> [M+H]<sup>+</sup> 1453.794, found: 1453.60

### 2.4.2 Electron Paramagnetic Resonance

The 9 GHz, continuous-wave EPR spectra were recorded using an ELEXSYS E680 spectrometer (Bruker, Rheinstetten, Germany). The measurements were done under the following conditions: room temperature, a microwave power of 0.63 mW and a modulation amplitude of 0.15 mT at a modulation frequency of 100 kHz. The time expended on each measurement was adapted according to the spectral lineshape, i.e., the aggregation time. For the starting point of the aggregation 30 min were expended, and up to 5 h for samples at the end of the aggregation series. Glass micropipettes of a volume of 50  $\mu$ L (Blaubrand Intramark, Wertheim, Germany) were filled with 20  $\mu$ L of the sample for each measurement. The spin concentration was determined by comparing the double integral of the EPR spectra with the double integral of a reference sample (MTSL, 100  $\mu$ M).

### ***2.4.3 Circular Dichroism***

Circular Dichroism (CD) spectroscopy is a form of light absorption spectroscopy that measures the differences in the absorption of right-handed versus left-handed circularly polarized light that arise due to the chirality of a molecule. The two types of circularly polarized light are absorbed to different extents. In a CD experiment, the same intensity of left and right circularly polarized light at a certain wavelength are alternately radiated into a sample. In the presence of chirality, one of the two polarized beams is absorbed more strongly than the other. The difference in absorption depends on the wavelength and it is measured as the CD spectrum. It has been shown that CD spectra between 260 and approximately 180 nm can be analyzed for the different secondary structural elements of proteins: alpha helix, parallel and antiparallel beta sheet, turn, and other. The ability of CD to give a representative structural signature makes it a powerful tool in modern biochemistry.<sup>95</sup>

The CD spectra were obtained using a J-815 CD Spectrometer (Jasco Benelux, Utrecht, The Netherlands). The measurements were carried out at room temperature under the conditions of 260 nm - 190 nm wavelength range, continuous scanning mode, a band width and a data pitch of 1 nm each, a speed of 20 nm/min and a total of five accumulations for each measurement. A 2-mm-path-length cuvette was used for measurements. A sample of 40  $\mu\text{L}$  of the aggregation solution was taken and diluted ten times in water in order not to saturate the photodetector of the spectrometer.

### ***2.4.4 Protocol of Aggregation Experiments***

Samples were prepared as follows: The powder of the TOAC EZ peptides was dissolved in Milli-Q water, in order to get a nominal peptide concentration of 500  $\mu\text{M}$ . The experiments were carried out during a week. After an initial measurement taken at the time the spin-labelled-peptide powder was diluted in water (called time-zero measurement), samples with a total volume of 560  $\mu\text{L}$  in 1.5 mL Eppendorf tubes were aggregated on a thermomixer (Thermomixer comfort) with a speed of 1000 rpm at 293 K. At each the time point, a 20  $\mu\text{L}$  sample was drawn for an EPR measurement, one of 40  $\mu\text{L}$  for CD and 10  $\mu\text{L}$  were frozen for future experiments. The time points were: one hour, four hours, one day (24 h), two days (48 h), three days (72 h), four days (96 h) and seven days (168 h).







### 3 Tracking amyloid oligomerization with monomer resolution using a 13-amino acid peptide with a backbone-fixed spin label

Amyloid oligomers are suspected as toxic agents in neurodegenerative disease, they are transient and often heterogeneous, making them difficult to detect. Here we show an approach to track the development of amyloid oligomers in situ by room temperature, continuous wave (cw) 9 and 95 GHz EPR. Three amyloid peptides with the 2,2,6,6-tetramethyl-N-oxy-4-amino-4-carboxylic acid (TOAC) spin label were synthesized by solid phase peptide synthesis: T0EZ (TKVKVLGDVIEVGG) with the TOAC (T) at the N-terminus, T5EZ, with TOAC in the middle (KVKVTGDVIEVG) and T12EZ, with TOAC at the C-terminus (KVKVLGDVIEVTG). These sequences are derived from the K11V (KVKVLGDVIEV) amyloid peptide, which self-aggregates to oligomers with a  $\beta$ -sheet configuration (Laganowsky, A. et al., Science 335, 1228–1231 (2012)). To monitor oligomerization, the rotational correlation time ( $\tau_r$ ) is measured by cw-EPR. For the backbone-fixed TOAC label that is devoid of local mobility,  $\tau_r$  should reflect the rotation and thereby the size of the peptide, resp. oligomer. For T5EZ a good match between the  $\tau_r$  measured and the size of the peptide is obtained, showing the validity of the approach. One of the three peptides (T0EZ) aggregates (circular dichroism), whereas the other two do not. Since also the respective MTSL (S-(1-oxy-2,2,5,5-tetramethyl-2,5-dihydro-1H-pyrrol-3-yl)methyl methanesulfonylthioate) labelled peptides fail to aggregate, molecular crowding due to the label, rather than the helix-inducing properties of TOAC seem to be responsible. Following in situ oligomer formation of T0EZ by the change in rotational correlation time, two oligomers are observed, a 5-6 mer and a 15-18 mer. The EPR approach, particularly 95 GHz EPR, enables to follow oligomerization one monomer at a time, suggesting that the cw-EPR approach presented is a novel tool to follow amyloid oligomerization with high resolution.

Zurlo, E., Gorroño Bikandi, I., Meeuwenoord, N. J., Filippov, D. V. & Huber, M. Tracking amyloid oligomerization with monomer resolution using a 13-amino acid peptide with a backbone-fixed spin label. *Phys. Chem. Chem. Phys.* **21**, 25187–25195 (2019).

### 3.1 Introduction

Amyloid aggregation is a central factor in amyloidogenic neurodegenerative diseases. Such diseases are widespread and so far most of them cannot be cured. One obstacle is the gap in knowledge about the physical chemistry of amyloid aggregation. Amyloid aggregation is the process in which the amyloid peptide self-assembles. The thermodynamic end-point of the aggregation is the  $\beta$ -sheet fibril, the main component of the plaques in the brains of patients, so far the main diagnostic feature for neurodegenerative disease.<sup>96,97</sup> Meanwhile, evidence is growing that amyloid oligomers, not fibrils, are the more toxic species<sup>14–19</sup>. Oligomers are aggregates of up to tens to hundred monomers. They can be on-pathway to fibrils, i.e. nuclei of fibrilization or off-pathway, meaning that they do not directly participate in fibril formation. Oligomers can differ in size, i.e. number of peptides, structure, stability and physico-chemical properties. Their transient nature and heterogeneity make the oligomers difficult to track.<sup>16,96,98</sup> Harmful oligomers are targets for drugs against neurodegenerative disease, generating a pressing need to design methods to determine the oligomers' mode of formation and structure. In particular, methods are needed to detect oligomers in situ, i.e. methods that show, which oligomers are formed, their relative concentration and how these parameters develop over time.

Here we explore the potential of liquid-solution, room temperature Electron Paramagnetic Resonance (EPR) at standard (9 GHz) and high (95 GHz) EPR frequencies to attain this goal.

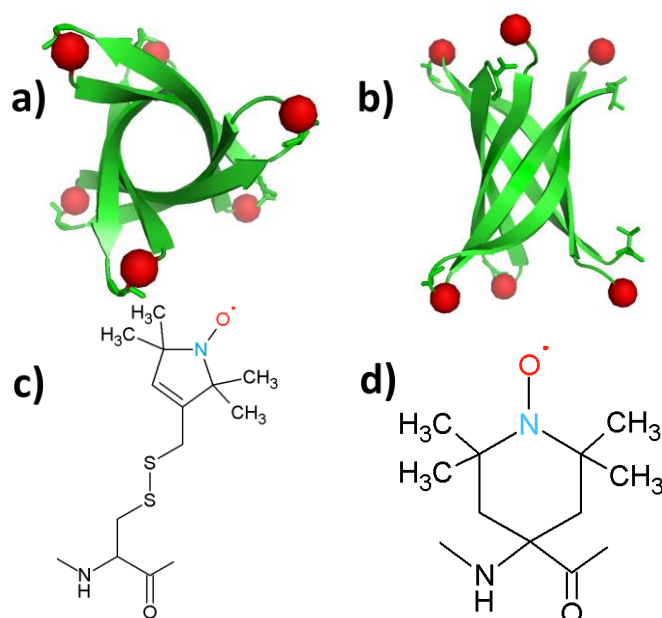


**Figure 3.1** Structure of K11V oligomer and relevant spin labels. a),b) Oligomer structure of K11V (PDB 3SGO), showing the 2,2,6,6-tetramethyl-N-oxyl-4-amino-4-carboxylic acid (TOAC) location for T0EZ (red dots). For details, see text. View in b) is rotated 90° with respect to a). c) Molecular structure of the MTSL spin label attached to a cysteine side-chain. d) Molecular structure of the TOAC spin label.

## Chapter 3

These techniques make it possible to follow oligomer formation by detecting the size of the oligomers: For continuous-wave EPR (cw EPR) in liquid solution, the spectral lineshape is a sensitive indicator for the rotational correlation time ( $\tau_r$ ) of an object, and it covers the time range from 0.03 ns to several ns<sup>47,99–101</sup>. As will be described below, this  $\tau_r$  range matches well with the  $\tau_r$  expected for the sizes of typical amyloid-forming oligomer peptides and their aggregates at room temperature in aqueous solution. Therefore, we expect to be able to track oligomer formation via the increase in  $\tau_r$ .

To perform EPR on amyloid peptides, the peptides need to be spin labeled. Conventionally, spin labels, like the S-(1-oxyl-2,2,5,5-tetramethyl-2,5-dihydro-1H-pyrrol-3-yl)methyl methanesulfonothioate (MTSL) label, are introduced via spin-label site-directed mutagenesis, which results in structures like Figure 3.1c<sup>47,59,100,101</sup>. While this approach is universal, the local mobility is a disadvantage in the study of amyloid aggregation: Rotation about the single bonds linking the nitroxide to the protein backbone dominates the motion and makes the measurement insensitive to peptide/oligomer size. We therefore use the backbone-fixed TOAC spin label (Figure 3.1d), which is incorporated into the peptide during solid phase peptide synthesis (SPPS)<sup>62,75–78,102–106</sup>. In these constructs, the nitroxide, containing the unpaired electron, is directly linked to the protein backbone, and therefore its  $\tau_r$  will follow the peptide rotation much more closely than the nitroxide in MTSL.

As model system we use the K11V peptide (Figure 3.1a,b), a short peptide, the sequence of which is derived from the  $\alpha$ B crystallin protein.<sup>67</sup> Such peptides, comprising 5-15 aminoacids have proven extremely useful for mechanistic studies. They show the essential properties of the protein they are derived from, but their smaller size is helpful to model their aggregation by MD methods, and, pioneered by the Eisenberg group, enable investigation by X-ray crystallography. The K11V peptide was shown to form toxic amyloid oligomers that could be crystallized. The X-ray structure shows a hexamer in  $\beta$ -sheet conformation, a  $\beta$ -barrel (Figure 1a,b).<sup>67</sup> Apparently, K11V forms fibrils much more slowly than other amyloid peptides, making it ideal to study oligomerization.

**Table 3.1** Sequences of peptides. The spin label TOAC (2,2,6,6-tetramethyl-N-oxyl-4-amino-4carboxylic acid) is abbreviated as *T*.

	sequence											
<b>K11V</b>	K	V	K	V	L	G	D	V	I	E	V	
<b>T0EZ</b>	<b>T</b>	K	V	K	V	L	G	D	V	I	E	V G
<b>T5EZ</b>	K	V	K	V	<b>T</b>	G	D	V	I	E	V	G
<b>T12EZ</b>	K	V	K	V	L	G	D	V	I	E	V	<b>T</b> G
<b>EZ</b>	K	V	K	V	L	G	D	V	I	E	V	G G

We synthesized four variants of the K11V peptide, a wild type analog (EZ) and three variants with the TOAC spin label in different positions (Table 3.1). We show that in spite

of the  $\alpha$ -helix inducing property of TOAC<sup>75-79,82,93</sup> one of the three TOAC constructs aggregates to oligomers. We demonstrate that our approach enables to follow aggregation in time with, in principle, monomer-size resolution.

## 3.2 Materials and methods

### 3.2.1 Synthesis and characterization of peptides

All chemicals were commercial products of the best quality available and, unless otherwise indicated, they were used without any further purification. The EZ peptide was purchased from tebu-bio (Heerhugowaard, The Netherlands).

9-Fluorenylmethoxycarbonyl(Fmoc)-amino acids, Fmoc-Gly-Wang Tentagel resin and the other chemicals used for the solid phase peptide synthesis were purchased from Sigma Aldrich. 2,2,6,6-Tetramethylpiperidine-N-oxyl-4-(9-fluorenylmethoxycarbonyl-amino)-4-carboxylic acid (Fmoc-TOAC-OH) and H-Gly-Wang resin were supplied by Iris Biotech (Marktredwitz, Germany).

The peptide sequences were assembled on AB433A Peptide Synthesizer (Applied Biosystems, Foster City, CA, USA), using 0.05 mmol of Gly-Wang resin (substitution 0.5 mmol/g). For all amino acids except TOAC we use 5 equivalents (0.25 mmol) of each AA for the synthesis. Deprotection by Fmoc was done 4 times (3 minutes each) by adding 2.5 mL of a solution of 20 % piperidine (PIP) in N-methylpyrrolidone (NMP). Couplings were performed using *2-(6-Chloro-1H-benzotriazole-1-yl)-1,1,3,3-tetramethylaminium hexafluorophosphate* (HCTU) as an activator and N,N-Diisopropylethylamine (DIPEA) as base. We used 1 equivalent of HCTU and 2 equivalents of DIPEA for 1 equivalent of AA. 1 mL of a solution of HCTU (0.25 M in NMP), 0.5 mL of a solution of DIPEA (1 M in NMP) and 0.5 mL of NMP were added to the resin for the coupling reactions. Each coupling reaction lasted 2 hrs.

The TOAC spin label was treated differently. Only 2 equivalents of AA were added for 1 equivalent of resin. Instead of HCTU, 1-[Bis(dimethylamino)methylene]-1H-1,2,3-triazolo[4,5-b]pyridinium 3-oxid hexafluorophosphate (HATU) was used as activator and 400  $\mu$ L of its solution (0.5 M in NMP) were put directly inside the cartridge with the spin label together with 600  $\mu$ L of NMP. The coupling in this case lasted 4 hrs. For the AA introduced immediately after the TOAC we used a double coupling, keeping the same conditions as for the rest of the sequence. The Fmoc absorption at 301 nm was followed to check the status of the synthesis after each coupling step.

At the end of the synthesis the resin was dried by washing it with dichloromethane (DCM). To cleave the peptide from the resin 2 mL of a solution 95% trifluoroacetic acid (TFA) + 5% water was used. A small amount of peptide was cleaved from the resin and

## Chapter 3

characterized by LC-MS. Unless otherwise indicated, the peptides were purified by semi-preparative HPLC.

Analytical HPLC separation was carried out on a LCQ Advantage Thermo Finnigan LC-MS system with UV-Vis and Ion-trap mass detectors. The column used was a C-18 Gemini (4.6 x 50 mm, 3  $\mu$ m particle size) from Phenomenex (Torrance, California). The mobile phase A (H<sub>2</sub>O), B (acetonitrile, MeCN) and C (aqueous 1 % TFA) was used for preparing ternary gradients. Elution condition: A 80 % B 10 % C 10-90 %, linear gradient B 18-33 % in 10 min. Flow rate 1 mL/min.

Crude peptide purifications were performed on a Gilson HPLC preparative system with a semipreparative Gemini C<sub>18</sub> column (10 x 250 mm) from Phenomenex with UV-Vis detector. The mobile phase A (H<sub>2</sub>O) and B (acetonitrile, MeCN) and C (aqueous 1 % trifluoroacetic acid, TFA) were used for preparing binary gradients. Elution condition: A 82 % B 18 %, linear gradient B 18-33 % in 10 min, Flow rate 5 mL/min.

The lyophilization was done on a Christ Alpha 2-4 LO lyophilizer (Salm&Kipp, Breukelen, Netherlands) with a Christ RVC 2-25 rotor. All TOAC peptides had a high level of purity as shown by single band elution and mass spectrometry.

T5EZ: yield 2.0%; LC-MS (C<sub>18</sub>)  $t_R$  4.56 min; purity > 95%; Mass: calculated for C<sub>61</sub>H<sub>108</sub>N<sub>15</sub>O<sub>18</sub> [M+H]<sup>+</sup> 1339.61, found: 1339.47

T0EZ: yield 10.8%; LC-MS (C<sub>18</sub>)  $t_R$  4.68 min; purity > 95%; Mass: calculated for C<sub>69</sub>H<sub>122</sub>N<sub>17</sub>O<sub>20</sub> [M+H]<sup>+</sup> 1453.794, found: 1453.53

T12EZ: yield 1.4%; LC-MS (C<sub>18</sub>)  $t_R$  4.85 min; purity > 95%; Mass: calculated for C<sub>69</sub>H<sub>122</sub>N<sub>17</sub>O<sub>20</sub> [M+H]<sup>+</sup> 1453.794, found: 1453.60

### ***3.2.2 Protocol for the aggregation experiments***

Samples were prepared as follows: The powder of the lyophilized spin-labelled EZ peptides was dissolved in Milli-Q water, in order to get a peptide concentration of 500  $\mu$ M by weight. Aggregation experiments were carried out during one week. After an initial measurement taken at the time the spin-labelled-peptide powder was diluted in Milli-Q water ( $t = 0$ ), samples with a total volume of 560  $\mu$ L in 1.5 mL Eppendorf tubes were aggregated on a thermomixer (Eppendorf, Thermomixer comfort, Waltham, MA USA) with a speed of 1000 rpm at 293 K. At each time point a 20  $\mu$ L sample was drawn for an EPR measurement, one of 40  $\mu$ L for CD and 10  $\mu$ L were frozen for future experiments, e.g. 95 GHz EPR and ThioT fluorescence. The time points were: one hour, four hours, one day (24 h), two days (48 h), three days (72 h) and seven days (168 h).

### 3.2.3 ThioflavinT fluorescence

The samples were monitored by the standard Thioflavin T (ThioT) fluorescence assay<sup>107</sup>. In summary, 5  $\mu\text{L}$  of sample solution were dissolved into 2 mL of a solution 5  $\mu\text{M}$  of ThioT and mixed for 30 seconds. The sample was excited at 457 nm and the fluorescence was observed in the range of 475 nm to 600 nm (Varian Cary Eclipse, San Jose, CA, USA). The fluorescence increase was measured with respect to the ThioT blank without the peptide.

### 3.2.4 EPR measurement conditions

The 9 GHz, continuous-wave EPR spectra were recorded using an ELEXSYS E680 spectrometer (Bruker, Rheinstetten, Germany). The measurements were done under the following conditions: room temperature, a microwave power of 0.63 mW and a modulation amplitude of 0.15 mT at a modulation frequency of 100 kHz. The time expended on each measurement was adapted according to the spectral lineshape, i.e., the aggregation time. For the starting point of the aggregation 30 min were expended, and up to 5 h for samples at the end of the aggregation series. Glass micropipettes of a volume of 50  $\mu\text{L}$  (Blaubrand Intramark, Wertheim, Germany) were filled with 20  $\mu\text{L}$  of the sample for each measurement. The spin concentration was determined by comparing the double integral of the EPR spectra with the double integral of a reference sample (MTSL, 100  $\mu\text{M}$ ). The spin concentrations were  $\approx 100 \mu\text{M}$  for a total concentration of peptide of 500  $\mu\text{M}$ .

The 95 GHz EPR spectra were recorded at room temperature on a Bruker ELEXSYS E680 spectrometer using a home-built probehead with a single-mode cavity specially designed for cw measurements. Acquisition parameters: microwave frequency 94.04 GHz, microwave power 0.63  $\mu\text{W}$ , modulation amplitude 1 mT, modulation frequency 6 kHz. Total measurement time: approximately 5 hours.

### 3.2.5 Simulations of EPR spectra

MATLAB (version 9.4.0.813654, R2018a, The MathWorks, Inc., Natick, MA, USA) and the EasySpin package (5.2.4) were used for simulations of the EPR spectra.<sup>48</sup> The parameters of the simulation were manually adjusted to agree best with the experimental spectra. For all simulations, an isotropic rotation of the nitroxide ( $S = 1/2$ ) was utilized. The following g-tensor values were used:  $g = [2.0086 \ 2.0059 \ 2.0020]$ . These values were

## Chapter 3

obtained from the simulation of the 275 GHz EPR spectrum of a frozen solution (100 K) of the peptide, using the “Pepper” algorithm in EasySpin, and we used these values for all other simulations. The principal values of the  $^{14}\text{N}$  hyperfine coupling tensor were  $A_{xx} = A_{yy} = 13$  MHz and  $A_{zz} = 110$  MHz.<sup>108</sup> The spectra were simulated with a superposition of three components: a fast fraction using the “Garlic” function, a medium and a slow fraction using the “Chili” function. For the 9 GHz spectra, a Gaussian component with a linewidth of 0.12 mT was used for the fast component, and 1 mT for the medium and slow components. For the 95 GHz spectra, a Gaussian line with a width of 0.5 mT was used for the fast component, whereas for the medium and slow components a mix of Gaussian and Lorentzian lineshape with a width of 0.1 mT was applied. The  $\tau_r$  of the fast component was chosen by simulating the narrow lines of the  $t = 0$  measurements and then kept constant for all other simulations. Optimal  $\tau_r$  values of the medium and slow components were derived from later time-point spectra and then kept constant for the entire series. For each time point, the relative contribution of the three components was optimized considering both 9 and 95 GHz spectra, for more details see SI.

### 3.2.6 Interpretation of $\tau_r$ values and molecular volumes

We used the Stokes-Einstein equation to interpret the  $\tau_r$  values. This implies a spherical approximation for the particles:

$$\tau_r = \frac{4\pi\eta\alpha^3}{3kT} = \frac{\eta}{kT} V_{EPR} \quad (3.1)$$

In Eqn. (3.1)  $k$  is the Boltzmann constant,  $T$  is the temperature (293 K),  $\eta$  is the viscosity of the solvent (1.02 cP for water) and  $\alpha$  is the hydrodynamic radius. The resulting volumes are referred to as  $V_{EPR}$  in the text.

The experimentally determined values of the volume ( $V_{EPR}$ ) have to be compared to the volumes of the peptide and its oligomers. There are two approaches to derive such estimates:

Method (i) uses the molecular weight (MW) and derives the volume assuming a certain density of the proteins using Eqn. (3.2), and we refer the volume obtained as  $V_{MW}$ . The second approach (ii) uses the dimension of the K11V oligomer (cylindrin) to derive the to-be-expected volume of the peptide. In the following we describe these two approaches.

Method

(i):

$$V_{MW} = \frac{MW}{N_A \rho} \quad (3.2)$$

## Chapter 3

Here,  $\rho$  is the protein density,  $N_A$  is Avogadro's constant and  $V_{MW}$  is the way we will address the volume obtained by this approach. To determine the number of monomers in the oligomers, the apparent molecular weight corresponding to  $V_{EPR}$  is calculated according to:

$$MW_{app,i} = V_{EPRi} N_A \rho \quad (3.3a)$$

$$n_i = \frac{MW_{app,i}}{MW_{T0EZ}} \quad (3.3b)$$

and the number of monomers in species  $i$ ,  $n_i$ , by dividing by the MW of the peptide T0EZ,  $MW_{T0EZ}$ .

The density of proteins of  $MW > 20$  kDa is generally assumed to be  $\rho = 1.35$  g/cm<sup>3</sup>,<sup>109</sup> however also other values were reported for smaller proteins, such as 1.50 g/cm<sup>3</sup>,<sup>110</sup>. In the SI, the influence of different  $\rho$  values is discussed and the resulting spread in  $n_i$  is included in the error estimation. The molecular weight of a monomer of T0EZ and of T12EZ is 1452.60 g/mol and for T5EZ 1338.47 g/mol.

Method (ii) uses the dimension of the oligomer of the K11V peptide that had been determined by X-ray crystallography<sup>67</sup>.

$$V_{XR} = \frac{\pi r^2 h}{6} \quad (3.4)$$

The volume of the oligomer is approximated as a cylinder of radius  $r$ , 11 Å, and a height,  $h$ , of 22 Å. The volume obtained agrees well with the volume obtained by HYDRONMR, see SI. The volume of the monomer obtained by Eqn. (3.4) is called  $V_{XR}$ .

## 3.3 Results

To determine the aggregation of the different TOAC constructs, Circular Dichroism (CD) spectroscopy was performed for samples taken at different time points of the aggregation. Initially all constructs display random coil CD spectra and T0EZ shows increasing  $\beta$ -sheet character over time, whereas T5EZ and T12EZ remain unchanged. More details of CD spectra on T0EZ are given in the SI (see also SI chapter 2), including the analysis using BeStSel<sup>111,112</sup>. To test for the formation of fibrils, ThioT fluorescence<sup>107</sup> was measured. None of the samples showed ThioT activity. This is to be expected as ThioT fluorescence requires linear cross-beta sheet structures of minimally six peptides in a row<sup>113</sup>, a requirement that the highly curved  $\beta$ -sheet in the  $\beta$ -barrel oligomer (Figure 3.1) does not fulfill. Therefore, the absence of ThioT fluorescence shows only that no fibrils are formed, however it does not exclude oligomers. For T0EZ these findings are consistent with a  $\beta$ -sheet oligomer: It displays  $\beta$ -sheet structure in CD and does not show



## Chapter 3

ThioT fluorescence, which excludes that  $\beta$ -sheet fibrils are formed. In the following, we first describe the EPR properties and the aggregation behavior of T0EZ and then the properties of the other two constructs, T5EZ and T12EZ.

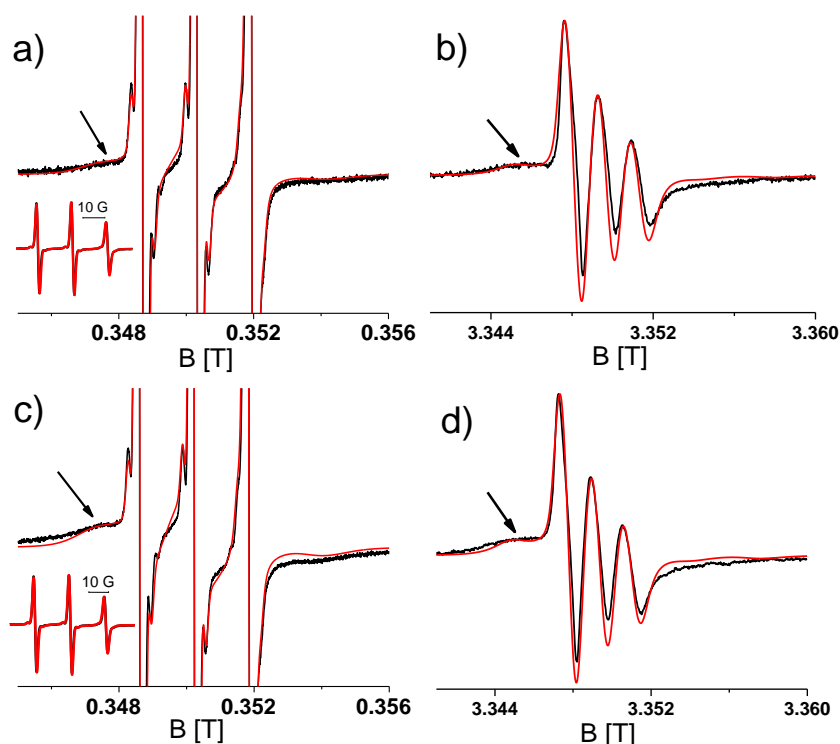


**Figure 3.2** Room temperature 9 and 95 GHz EPR spectra of T0EZ at different time points of aggregation. a) c) 9 GHz EPR spectra. Full spectra: Inset. Zoomed-in spectra: Amplitude expanded ten-fold with respect to inset. b) d) 95 GHz spectra. Spectra a) and b): Start of aggregation ( $t = 0$ ). c) and d): At 48 hours of aggregation. Black: Experimental spectra. Red: Simulated spectra. Note that at 95 GHz the signal appears at around ten times higher field  $B_0$ .

Figure 3.2 shows the EPR spectra of T0EZ at 9 and 95 GHz obtained at two time points of aggregation; at the start (Figure 3.2a and b) and after 48 hours of aggregation (Figure 3.2c and d), the spectra of all time points are collected in Figure S3.1. The 9 GHz EPR spectra are dominated by three narrow lines (see inset) of a nitroxide in fast rotation. The arrow marks an additional broad component, representing a component with lower mobility. In the 95 GHz EPR spectra (Figure 3.2b and 3.2d), taken at around ten times higher field, this component is better separated from the three-line pattern than at 9 GHz EPR. The spectra at the two time points differ mostly in the relative amplitude of the broad with respect to the narrow component. The broad component has a higher amplitude in Figure 3.2c and d than that in Figure 3.2a and b. To quantitate the changes in the EPR spectra, we performed spectral simulations.

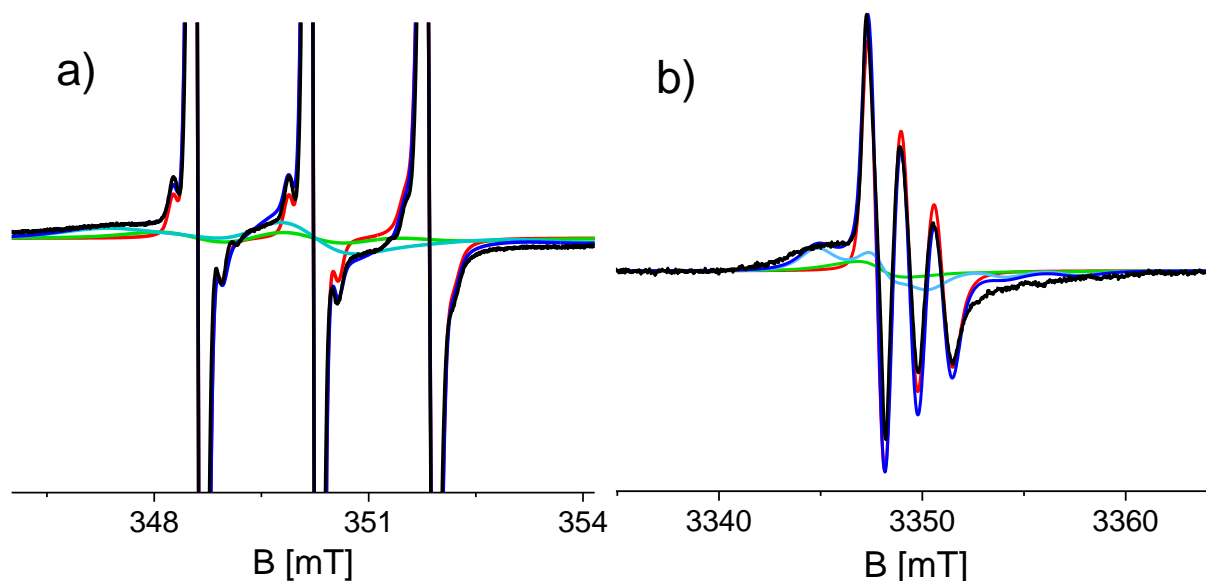


**Figure 3.3** Spectral components used in the simulation of the 9 and 95 GHz EPR spectra of T0EZ ( 48 hours of aggregation). Experimental spectra (black), fast component (red), medium component (green), slow component (light blue). Total simulation (dark blue). For details see text.

Simulations required minimally three components with different rotational correlation times ( $\tau_r$ ). Figure 3.3 shows the shape of these components for the spectra shown in Figure 3.2c and d, i.e. at 48 hours of aggregation. The contribution with the longest  $\tau_r$  (light blue) gives rise to the broad features marked in Figure 3.2 by the arrows. The  $\tau_r$  values are given in Table 3.2. To simulate the entire series of time points, the  $\tau_r$  of each component was kept constant and only the relative amount of the components was varied throughout the time series. Furthermore, the 9 and 95 GHz EPR spectra for the same time point were simulated with the same relative amounts of the components. The higher resolution of 95 GHz EPR makes it easier to detect the slow components. Compare Figure 3.2b and d (95 GHz) with 3.2a and c (9 GHz). The slow and medium components are related to aggregates and the amount by which they contribute to the spectra in time increases as shown in Figure 3.4.

**Table 3.2** . Rotational correlation times of T0EZ from the simulation of the EPR spectra, and corresponding molecular volumes ( $V_{EPR}$ ). Using monomer volumes from different sources (see text), the number of the peptides in the oligomer is derived.

Components	$\tau_r$ [ns]	$V_{EPR}$ [nm <sup>3</sup> ] <sup>a</sup>	Number of monomers in aggregate	
			From MW <sup>b</sup>	From XR <sup>c</sup>
<b>Fast</b>	$0.16 \pm 0.004$	$0.65 \pm 0.02$	-	-
<b>Medium</b>	$2.00 \pm 0.20$	$8.08 \pm 0.81$	$5 \pm 1$	$6 \pm 1$
<b>Slow</b>	$6.31 \pm 0.70$	$25.49 \pm 2.83$	$15 \pm 2$	$18 \pm 2$

a) From Stokes-Einstein (Eqn. 1).

b) From protein density (Eqn. 2) using  $\rho = 1.35 \text{ g/cm}^3$ , for further uncertainties in these numbers, see text.

c) From X-ray crystallography (Eqn. 3) , for further uncertainties in these numbers, see text.

### Chapter 3

Using the Stokes-Einstein equation (Eqn. 3.1) the  $\tau_r$  values can be related to the volumes of the observed species (Table 3.2). These volumes suggest that the medium fraction is a pentamer or hexamer, the slow fraction a 15-18 mer.

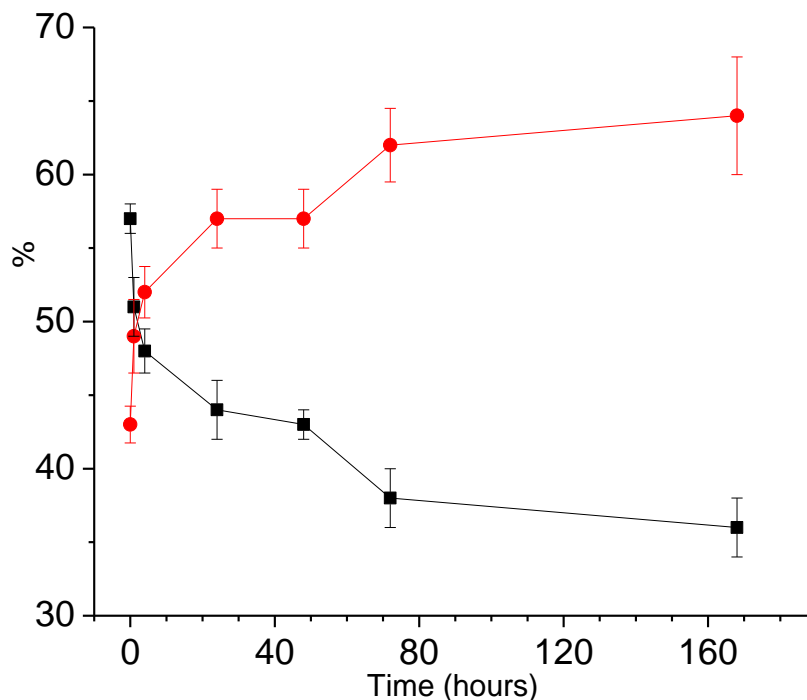


**Figure 3.4** Aggregation of T0EZ as a function of time. Amount of aggregates (red, slow and medium EPR components combined); amount of monomers (black, fast EPR component). The lines are a guide to the eye.

Figure 3.4 shows that the amount of combined slow and medium component increases for the first 70 hours of aggregation, afterwards it stays constant within the error margins, indicating that a steady state is reached. Also at the earliest time points some aggregates are present.

**Table 3.3** The rotational correlation times of the monomers of T0EZ, T5EZ and T12EZ. Molecular volumes ( $V_{MW}$ ) monomers calculated from the molecular weight (MW) using the protein density equation (Eqn. 3.2).

Peptides	$\tau_r$ Monomers [ns]	$V_{EPR}$ [nm <sup>3</sup> ]	$V_{MW}$ [nm <sup>3</sup> ]
T0EZ	$0.16 \pm 0.004$	$0.65 \pm 0.02$	$1.78 \pm 0.17$
T5EZ	$0.40 \pm 0.02$	$1.61 \pm 0.07$	$1.65 \pm 0.15$
T12EZ	$0.31 \pm 0.02$	$1.25 \pm 0.06$	$1.78 \pm 0.17$

Finally, in Table 3.3, the  $\tau_r$  values of all TOAC-EZ constructs in their monomeric state are given. The peptides T0EZ and T12EZ have the same composition, T5EZ has one amino-acid residue less. Thus from the volume of the peptide one would expect that T0EZ and T12EZ have longer  $\tau_r$  values than T5EZ, however the opposite is true. This suggests that the TOAC in T0EZ and T12EZ has residual freedom to move making the observed  $\tau_r$  shorter than expected from the molecular weight.

## 3.4 Discussion

In this study we use cw, room temperature EPR at 9 and 95 GHz to determine the size-development of amyloid oligomers in time. The size of the aggregates can be tracked in situ, in the aggregation solution. The method is demonstrated with an amyloid peptide based on K11V<sup>67</sup> into which we incorporated the backbone-fixed spin label TOAC.

### 3.4.1 Is TOAC a good monitor for peptide size?

Even though TOAC is directly linked to the peptide backbone (Figure 3.1d), local backbone motion could still uncouple it partly from the peptide-oligomer-overall rotation. To assess this factor we consider the  $\tau_r$  values for the monomeric peptides (Table 3.3). The  $\tau_r$  values are related to the volume of the object via the Stokes-Einstein relation (Eqn. 3.1) resulting in  $V_{\text{EPR}}$ . This volume is compared to the molecular volume of the peptides obtained from the molecular weight (Eqn. 3.2),  $V_{\text{MW}}$ . In Table 3.3 these volumes are given. For T5EZ,  $V_{\text{EPR}}$  is close to the  $V_{\text{MW}}$ , showing that for this peptide,  $\tau_r$  is a good measure for the peptide size. The peptides T0EZ and T12EZ have smaller  $V_{\text{EPR}}$  values than T5EZ, although their molecular volumes are larger. This shows that the motion of the spin label at the N- and C-terminus is partially uncoupled from that of the peptide, in other words, the backbone section that the TOAC is attached to displays local mobility. Comparing all three peptides, the mobility is higher at the N-terminus than at the C-terminus (T0EZ has a shorter  $\tau_r$  than T12EZ), and smallest in the center (T5EZ). The case of T5EZ shows that the concept of using TOAC to monitor the molecular volume works well, at least in a situation where the TOAC is well embedded in the object. The  $\tau_r$  values of all TOAC constructs are longer than those of the MTSL analogues, see SI Table S3.2, as expected, given that in MTSL the nitroxide is not rigidly linked to the protein backbone.

### 3.4.2 Influence of TOAC position on the aggregation of the EZ peptides

Two of the three TOAC constructs (T5EZ and T12EZ) do not aggregate. For T5EZ, with the TOAC in the middle of the  $\beta$ -sheet region, two factors combine to inhibit aggregation: Crowding in the middle of the  $\beta$ -barrel (see Figure S3.3) and the  $\alpha$ -helix-inducing properties of TOAC, which could inhibit the formation of the  $\beta$ -sheet and thereby of the oligomer. To test whether the  $\alpha$ -helix-inducing character of TOAC is the dominant factor inhibiting aggregation, we also tested the MTSL-labelled counterparts (see SI). Also, the

equivalent constructs to T5EZ and T12EZ with an MTSL label failed to aggregate. As MTSL labels do not break  $\beta$ -sheets, it seems evident that crowding is more important than  $\beta$ -sheet breaking. More puzzling is the question why the TOAC at the C-terminus inhibits aggregation, whereas at the N-terminus it does not. Here the difference in the  $\tau_r$  values of T0EZ and T12EZ could give a hint. Apparently, the N-terminus has a higher local mobility than the C-terminus, and that, in turn, may enable TOAC at the N-terminus to avoid molecular crowding in the oligomer, enabling T0EZ to aggregate to oligomers.

### ***3.4.3 Oligomerization of T0EZ as followed by EPR***

Having established that TOAC enables to track molecular size, i.e. the number of peptides per oligomer, we use it to analyse the aggregation of T0EZ. The size and the amount of the oligomers increases with time (EPR) (Figure 3.4 and S3.2), the aggregates have  $\beta$ -sheet structure (CD) and do not convert to fibrils on the time scale of the experiment (ThioT). With respect to the size of oligomers, an initial fraction of smaller oligomers (medium fraction by EPR), some of them present even at the earliest time point taken, and a later fraction with larger aggregates (slow fraction) are observed (Figure S3.2). These are two distinct populations, as two spectral components, the medium and the slow, are needed to represent them. The number of monomers in the two fractions, penta-to-hexamers and 15-18 mers (see Table 3.2), has a large uncertainty as several approximations enter in the estimation. In the SI these are described and evaluated quantitatively. The impact of some approximations can be determined quantitatively: The two different ways to estimate monomer volumes (Table 3.2), show that for the smaller oligomers (medium EPR fraction) differences of one monomer unit and for the larger oligomers (slow EPR fraction) differences of three monomer units result. Other factors can be qualitatively assessed: The local mobility of the TOAC in the oligomer leads to an underestimation of the size of the oligomer, thus the oligomer size determined by is a EPR a lower limit (for details, see SI). Overall, due to the approximations described in the SI, the relative oligomer sizes are more reliable than the absolute values. To determine the absolute number of monomers in the oligomers, dedicated experiments are possible (see below).

The oligomers are most likely heterogeneous, i.e. the two oligomer fractions do not consist exclusively of oligomers of one particular size. A homogeneous population would have a distinctive lineshape as shown in Figure S3.6, and it is likely that also the superposition of two homogenous populations would still give spectra that are better resolved than those experimentally observed. More detail could be obtained by increasing the time resolution, i.e. by measuring more time points. Such experiments could also reveal, if the oligomers grow by adding monomers or whether smaller oligomers assemble into the larger ones, however such experiments are beyond the scope of the present study.

Additional EPR experiments could determine the number of monomers in specific oligomers<sup>114,115</sup>, as an independent check point, however, these methods rely on frozen solutions and thereby lack the power of the in situ measurement we present here.

### ***3.4.4 Aggregation of T0EZ***

The investigation presented gives clear evidence that the aggregation of T0EZ proceeds in several steps. It reveals an initial fraction, the EPR medium fraction, which, considering the approximations described in the SI, may be an hexamer similar to that observed by Laganowsky et al.<sup>67</sup>. The  $\beta$ -barrel structure is confirmed by CD, its hexameric nature fits well with the rotation correlation time derived from EPR. The exact shape, e.g. the antiparallel arrangement of the peptides (Figure 3.1) would have to be confirmed by more extensive EPR investigations, see below. While these oligomers are the end point of aggregation under the conditions employed in Laganowsky et al.<sup>67</sup>, the present study shows a further growth of the aggregates over time, to larger oligomers, as proven by the size observed by EPR (15 – 18 peptides). The absence of ThioT activity rules out that these latter objects are fibrils, in particular, it shows that the oligomers do not have the non-curved  $\beta$ -sheets required for ThioT binding. Laganowsky et al. show that K11V forms fibrils when exposing it to vigorous shaking at 50 °C over a period of 7 days. The lower temperature of the present experiments was chosen to enhance oligomers, therefore, in the present study, high temperature and vigorous shaking were avoided. Our finding of two different types or groups of oligomers that differ in size suggests that the respective oligomers can have different physiological/disease effects and that their properties must be studied individually for a full understanding of their relevance.

Also other studies have shown that oligomers can increase in size over time<sup>116,117</sup>. In particular, ion-mobility mass spectrometry (IM-MS) showed that other short amyloid peptides, when investigated under conditions that are not optimized for crystallization also go through a series of oligomers, the size of which increases over time.<sup>118,119</sup>

Overall we observe the aggregation of T0EZ into oligomers with a  $\beta$ -sheet structure. The absence of ThioT fluorescence confirms that, at least within the time scale investigated (12 days), no fibrils are formed. Therefore, these oligomers are unlikely to be seeds for fibrilization and should be considered off-pathway oligomers. More detail could be determined by kinetic analysis as pioneered by the Knowles group<sup>117</sup>. The approach of the present study is of course not limited to this particular peptide: Other short peptides, especially those that aggregate to fibrils, could be investigated. In these cases, besides the end-product, the fibrils that should be ThioT active, on- and off-pathway oligomers are expected. To compare the properties of these oligomers to those occurring in the EZ oligomers would give further insight into the aggregation process that from the physical-chemistry point of view is still far from understood.

## 3.5 Conclusions and outlook

Here we show that peptides with TOAC at strategic positions combined with high-field EPR open a new way to study amyloid aggregation: The real-time measurement of rotational motion reveals directly the size of the oligomer at specific time points. While, in the model system we investigate, only two chief fractions are observed that differ by approximately 12 monomers, the approach itself can follow the development with single-monomer resolution in the otherwise difficult to differentiate<sup>43</sup> oligomer size distribution from two to 15 monomers, see SI. Our approach is therefore one of the few methods presently available to track oligomers as they develop. In contrast to IM-MS, a method that provides the molecular mass and information about the outer size of the oligomers after gas-phase ionization, the high-field EPR approach presented here determines the oligomers in solution, avoiding chemical separation, vacuum-desorption and gas-phase, ionization steps. It therefore perfectly complements existing methods and is an excellent new tool in the quest for molecular information on amyloid aggregation. We show here that the approach can be applied to one particular peptide, however, the principle shown is universal for other peptides of interest, as long as they are amenable to SPPS to incorporate the TOAC, either for the full peptide or a fragment that can be fused to a protein that provides the full-length sequence of interest. We also demonstrate that in spite of adverse properties of TOAC, aggregating peptides can be generated. Of course, the presence of TOAC and its eventual effects on the aggregation should be tightly monitored. These disadvantages clearly are outweighed by the merits of the TOAC approach, as can be seen in the poor size differentiation obtained from the conventionally labelled peptides in the SI.

Finally, once the intermediates are identified and their size development over time is established by the approach presented here, the structure of each of the identified states can be investigated: By distance determination using EPR via spin-spin interaction<sup>58</sup> and other techniques, inter- and intramolecular interactions can be determined, yielding structural constraints for modelling. Small angle X-ray scattering (SAXS) can identify overall shape, CD and FTIR can yield internal structure.

Furthermore, for many systems the present detail would already yield new insights: On- and off-pathway oligomers could be tracked in their time development<sup>97</sup>. These experiments would identify states that warrant more detailed investigation such as determining their individual mode of toxicity and applying further structural methods.

## 3.6 Supporting information

### 3.6.1 Supplementary figures

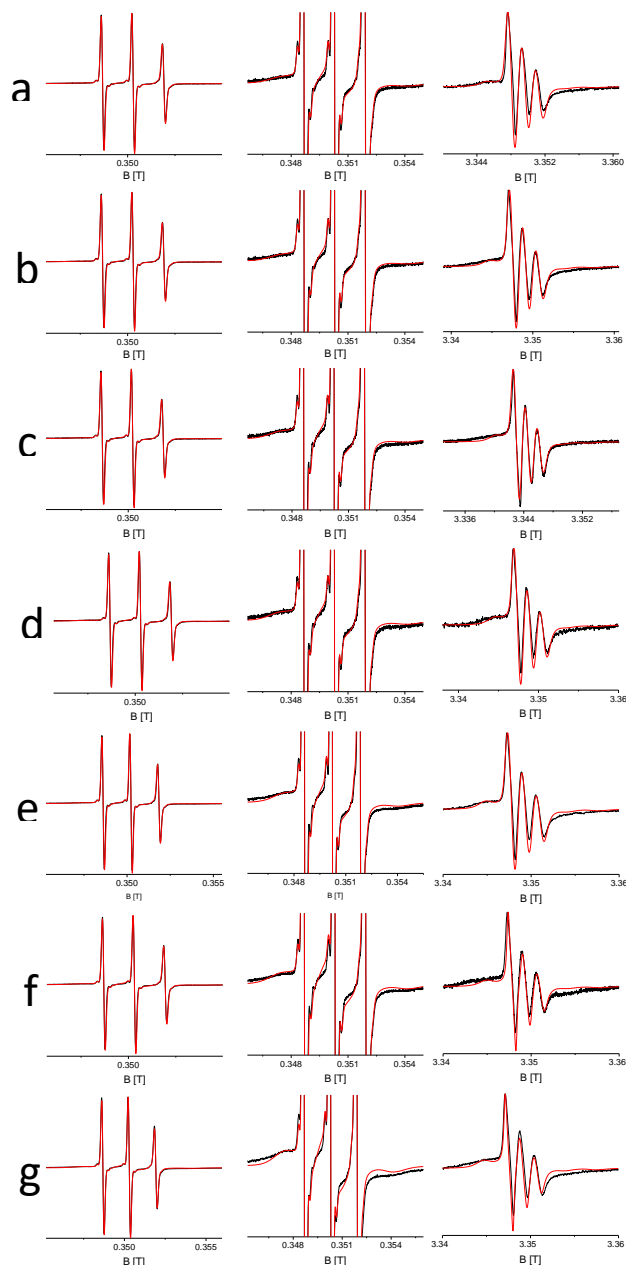


**Figure S3.1** Room temperature 9 and 95 GHz EPR spectra of T0EZ for the entire time point series taken during aggregation. Left: 9 GHz EPR, full spectra. Central: 9 GHz EPR spectra, amplitude expanded ten-fold. Right column: 95 GHz spectra. Spectra a) 0 hrs, b) 1 hr, c) 4 hrs, d) 24 hrs, e) 48 hrs, f) 72 hrs, g) 168 hrs. Black: Experimental spectra. Red: Simulated spectra. Remaining experimental conditions and detailed description: See main text.



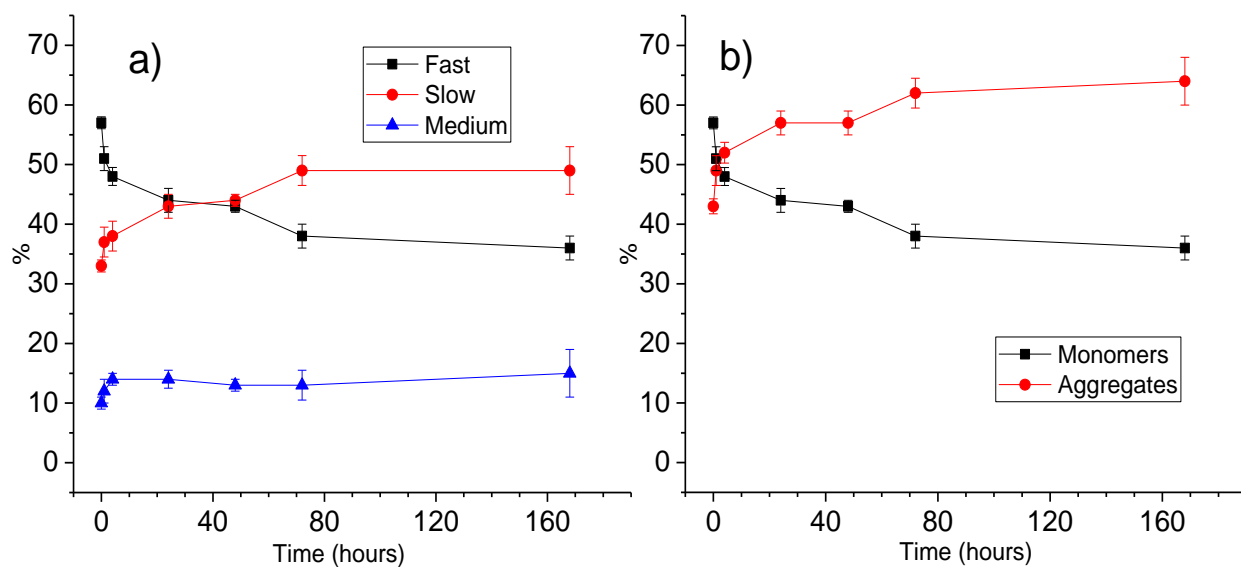


**Figure S3.2** a) Amount of the fast, medium and slow components in the EPR spectra of T0EZ as a function of the aggregation time: fast (black), medium (blue) and slow (red). b) From Figure 3.4 in the main text: Slow and medium components combined (red). The lines are a guide to the eye.

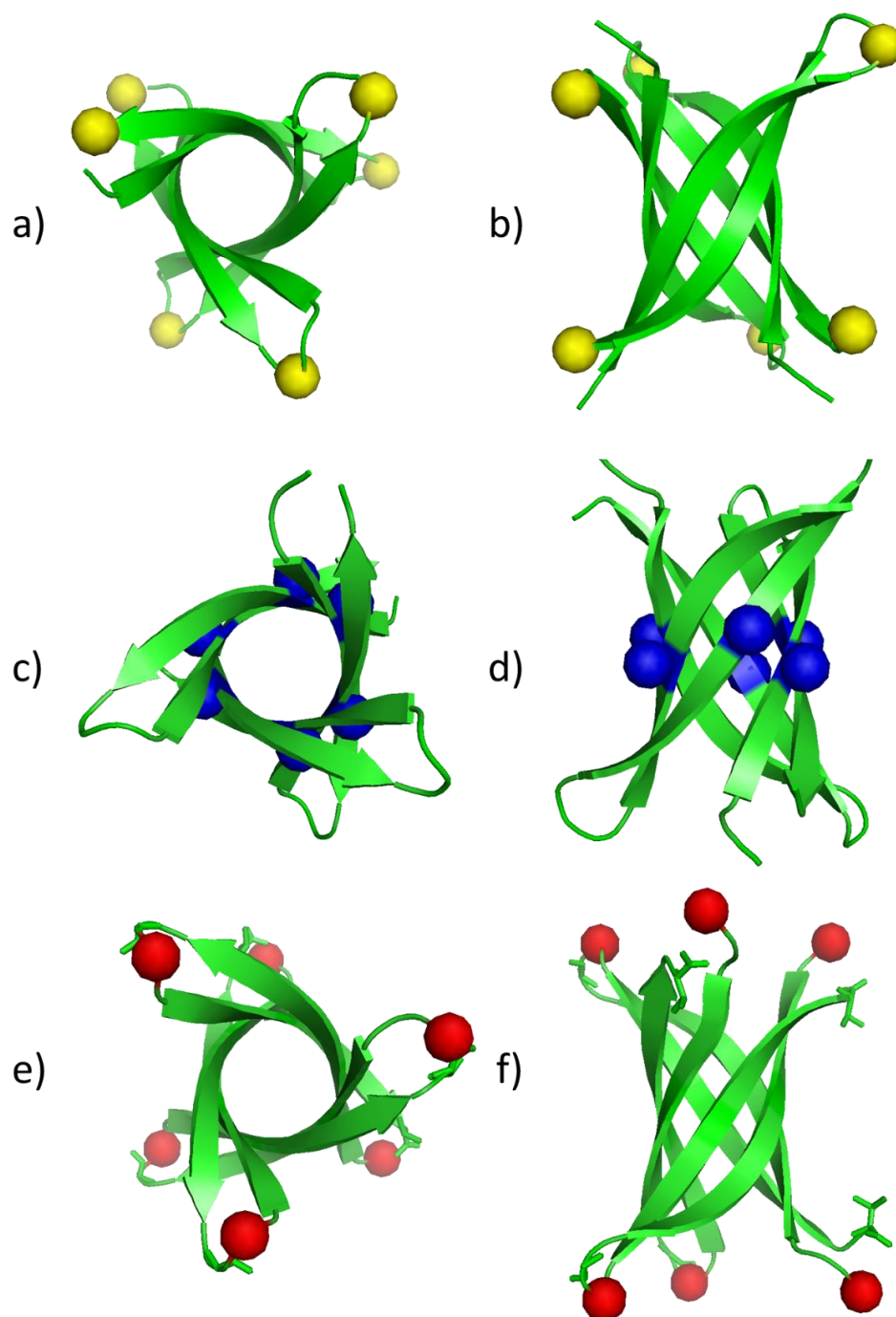


**Figure S3** Location of TOAC spin label expected for T0EZ, T5EZ and T12EZ, given the structure of the K11V oligomer (PDB 3SGO)<sup>67</sup>. a) T12EZ-TOAC: yellow spheres. b) view in a) rotated by 90°. c) T5EZ-TOAC: blue spheres. d) view in c) rotated by 90°. For reference also for T0EZ, the TOAC location is shown: e) T0EZ-TOAC: red spheres. f) view in e) rotated by 90°, see also Figure 3.1a) and b).

### 3.6.2 Supplementary materials and methods

#### 3.6.2.1 Circular dichroism

The CD spectra were obtained using a J-815 CD Spectrometer (Jasco Benelux, Utrecht, The Netherlands). The measurements were carried out at room temperature under the conditions of 260 nm - 190 nm wavelength range, continuous scanning mode, a band width and a data pitch of 1 nm each, a speed of 20 nm/min and a total of five accumulations for each measurement. The 40  $\mu$ L samples for each aggregation time point were diluted ten times in milli-Q water. A 2-mm-path-length cuvette was used for measurements.

### 3.6.3 Supplementary data

#### 3.6.3.1 Circular dichroism of T0EZ aggregation

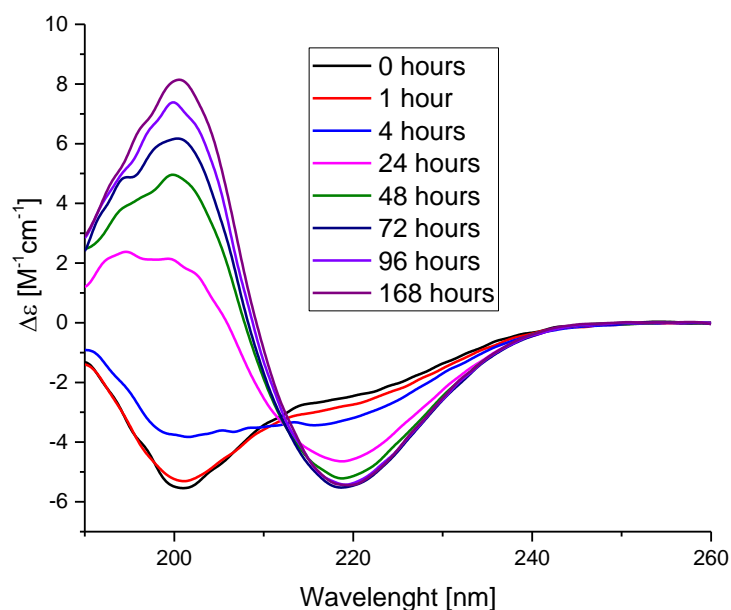


**Figure S3.4** Development of the CD spectra of T0EZ measured at different time points of aggregation at room temperature. The spectra have been smoothed by 15 points FFT filter by Origin® for better visualization. At time zero the spectrum (black) presents a lineshape of a random coil structure. After 168 hours the spectrum (wine) shows a lineshape of a  $\beta$ -sheet secondary structure.

Figure S3.4 shows the T0EZ circular dichroism (CD) spectra measured over the time course of aggregation. In Figure S3.4 there is a gradual progression of the lineshape from random coil to a  $\beta$ -sheet configuration. The negative feature at 200 nm, characteristic for random coil, becomes positive through time which is a sign of  $\beta$ -sheet structure

formation. The negative peak with increasing amplitude around 218 nm is also characteristic of  $\beta$ -sheet. The development suggests an increase of  $\beta$ -sheet character over time, which is expected for  $\beta$ -sheet oligomers.

To obtain the secondary structure composition of the sample according to the CD spectra we use the BeStSel program designed to decompose the CD spectra of proteins. Figure S3.5 shows the results for the 190 nm to 260 nm wavelength range. As CD averages the secondary structure per residue over time whereas EPR yields the composition per peptide, a 1 : 1 correspondence of the percentage contribution cannot be expected. Nevertheless, the methods show the same trend: Decay of random coil (CD) and monomer content (EPR) and an increase in  $\beta$ -sheet (CD) and oligomers (EPR). Numerically, random coil and EPR fast fraction agree for the samples up to 20 hours, after that the agreement is better when the random coil and turn fractions from the CD analysis are added. The model of K11V predicts anti-parallel arrangements of the strands in the K11V oligomer, so the parallel  $\beta$ -sheet component in the CD analysis is surprising. As also the attribution of secondary structure elements in CD spectra within BeStSel is not completely established, additional structural information about the species occurring during oligomerization would be needed to clarify this point. Distance measurements by EPR<sup>59,120,121</sup> could provide this kind of information, however, it is beyond the scope of the present investigation.

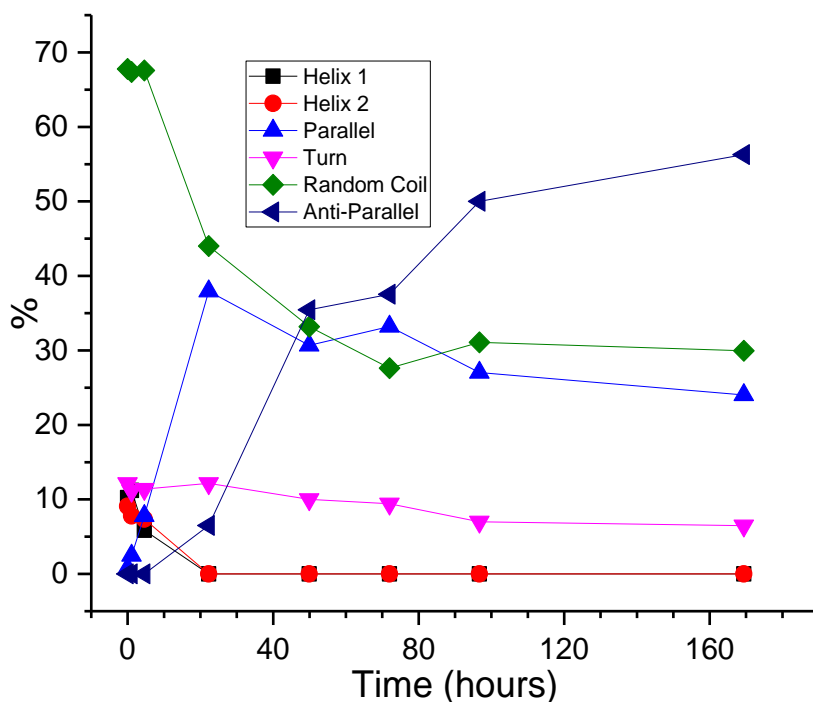


**Figure S3.5** Analysis of the CD spectra in Figure. S4 using BeStSel software<sup>111,112</sup>, showing the amount of the secondary structures of T0EZ over time derived from the CD spectra. Helix 1 (black) and helix 2 (red) are the different helical conformations. Random coil (green) is considered as mainly being the “Others” component of BeStSel. BeStSel provides three antiparallel  $\beta$ -sheet components, left-twisted (Anti1), relaxed (Anti2) and right twisted (Anti3), which are added up here as Anti-Parallel (navy). For the first 4 hours, when Anti1 and Anti2 were zero, the value of Anti3 (having a basis spectrum similar to that of the disordered structure), was added to the random coil. Parallel (blue) is the parallel  $\beta$ -sheet structure. Turn (pink) is the beta-turn structure. The lines are a guide to the eye.

### 3.6.3.2 Activity of TOAC and diamagnetic dilution

Low spin label activity in peptides results in diamagnetic dilution. Protonation by strong acids (TFA) used during peptide synthesis to cleave the peptide from the resin (see Materials and Methods) is known to reduce and thereby inactivate the nitroxide of TOAC at least partially<sup>84</sup>.

Two experiments show that this is also the case for T0EZ: The concentration of the peptide determined from the weight of the lyophilized powder is five times higher than the spin concentration determined by EPR, as described in Materials and Methods, showing that only 20 % of the TOAC is active in the peptide. To confirm that TOAC is inactivated by TFA, a sample of T0EZ in DMSO was incubated for 3 hours by adding 10 % of a solution of NH<sub>3</sub> in water (Sigma-Aldrich 28-30 %). After incubation, the EPR signal had increased by a factor of four, confirming that acid-deactivation by TFA is the most likely origin of low spin concentration of the as-synthesized T0EZ.

While usually undesired, here we use the as-synthesized T0EZ without activation because the low activity of TOAC provides a convenient – and otherwise difficult to realize – way to diamagnetically dilute spins. During aggregation the peptide with a paramagnetic, active TOAC will be incorporated randomly with the inactive peptides into the aggregates, which is referred to as diamagnetic dilution. Diamagnetic dilution increases the spin-spin distance, generating spectra devoid of spin-spin interactions, if (i) the ratio of inactive vs active labels is sufficiently large considering the expected distance and (ii) if the species with active spin labels are randomly distributed in the structure.

$$z = \frac{n!}{(n-p)!p!} \cdot a^p \cdot (1-a)^{n-p} \quad (\text{S3.1})$$

To estimate if condition (i) is fulfilled, we analyze the spin proximity in the cylindrin hexamer.<sup>67</sup> Eqn. S3.1 defines which fraction of hexamers  $z$  contains a given number  $p$  of active TOAC labels. In Eqn. (S3.1)  $z$  is the population of spin-labelled oligomers,  $p$  is the number of active spin labels in the oligomer,  $n$  is the number of monomers in the aggregate and  $a$  is the fraction of active spin labels.

For a  $p$  of 2 Table S3.1 shows that 26 % of the hexamers are expected to contain two labeled peptides. In this fraction the distances between the two spin centers is expected to be either 15 Å or 25 Å<sup>67</sup>. This corresponds to a dipolar interaction of 2.45 MHz and 0.53 MHz, i.e. 0.09 mT to 0.02 mT. Such a broadening would be undetectable given the width of the spectral lines, allowing us to neglect any influence of spin-spin interactions in the analysis. A random distribution of active and inactive peptides (assumption (ii)) is likely as both types of peptides only differ in the protonation state of the nitroxide, so they have almost identical chemical structures.

**Table S3.1** Number of spin-labelled peptides with active nitroxides expected for hexameric oligomers.

$p$	$z \%$
0	$23.0 \pm 2.0$
1	$38.0 \pm 3.0$
2	$26.0 \pm 2.0$
3	$9.8 \pm 0.8$
4	$2.0 \pm 0.2$
5	$0.2 \pm 0.1$

### 3.6.3.3 Simulations of EPR spectra: Quality of the fits

As described in the main text, the overall strategy was to simulate the spectra with a common set of parameters, using the smallest number of components that fit the entire time series, to avoid overfitting the data. Here we discuss this approach in more detail and describe its consequences for the simulations. Three components, the fast, medium and slow, were sufficient. For each individual time point, the 9 and 95 GHz EPR spectra were fitted with the same composition of these three components, finding the optimum that agrees best for both spectra. Relaxing these constraints or introducing other mobility models, such as anisotropic rotation models<sup>122–124</sup>, improves the simulation of the individual spectra, but introduces additional parameters that may result in overfitting the spectra. The results of the three-component simulations are displayed in Figure S3.1, in which the simulated spectra are shown in red. For aggregation times up to 24 hours, the agreement of simulation and experiment is very good for 9 and 95 GHz spectra, whereas later time-point spectra show some deviation: As a representative for deviations, we discuss the spectra in Figure S3.1f): The experimental 95 GHz spectrum has intensity at the low field side of the spectrum ( $B_0 = 3.340\text{--}3.345$  T) and the high field side of the spectrum ( $B_0 = 3.353\text{--}3.357$  T) that is not covered by the simulation. This spectral intensity would correspond to a very slow/immobilized component in the spectrum that is not compatible with the 9 GHz EPR spectrum. The appearance of such a slow component in the 95 GHz spectra could derive from instrumental effects: The overall baseline stability in 95 GHz EPR is worse than in 9 GHz, so part of this broad component could be attributed to such instabilities. They would have a stronger impact on the later time spectra, because the amplitude of the narrow, three-line spectrum is less, causing an apparent increase in amplitude of baseline artefacts (note that in Figure S3.1 the spectra are amplitude scaled to the narrow component). Secondly, the samples for 95 GHz EPR had to be stored frozen before the measurements, whereas most of the 9 GHz EPR spectra were measured directly after the samples were drawn from the aggregation mixture. It cannot be excluded that freezing affects the sample. We therefore considered this spectral intensity in the 95 GHz EPR spectra as less important and focused more strongly on the 9 GHz EPR spectra of this particular time point. Apparently, for this time point the

optimum solution for both 9 and 95 GHz EPR spectra limits the degree of agreement of simulation and experiment that can be reached.

### 3.6.3.4 Comparison of $\tau_r$ in TOAC versus MTSL-labelled EZ peptides

**Table S3.2** Experimentally determined rotational correlation times of monomeric EZ peptides from 9 GHz and 95 GHz EPR. MXEZ: construct with MTSL at the same position as the TOAC in TXEZ. Molecular volumes from EPR ( $V_{\text{EPR}}$ ) and molecular weight ( $V_{\text{MW}}$ ) are also given (see main text).

Peptides	$\tau_r$ Monomers [ns]	$V_{\text{EPR}}$ [nm <sup>3</sup> ] <sup>a</sup>	$V_{\text{MW}}$ [nm <sup>3</sup> ] <sup>b</sup>
<b>T0EZ</b>	0.16 ± 0.004	0.65 ± 0.02	1.78
<b>T5EZ</b>	0.40 ± 0.02	1.61 ± 0.07	1.65
<b>T12EZ</b>	0.31 ± 0.02	1.25 ± 0.06	1.78
<b>M0EZ</b>	0.14 ± 0.01	0.56 ± 0.03	1.89
<b>M5EZ</b>	0.18 ± 0.003	0.73 ± 0.01	1.69
<b>M12EZ</b>	0.15 ± 0.004	0.59 ± 0.02	1.89
<b>K11V</b>			1.47
<b>EZ</b>			1.61

a) From Stokes-Einstein (Eqn. 3.1).

b) From protein density ( $\rho = 1.35 \text{ g/cm}^3$ ) (Eqn. 3.2).

Table S3.2 gives the values of  $\tau_r$  of the monomeric EZ peptides obtained from the simulations of the 9 GHz and 95 GHz EPR spectra. In addition to the values for T0EZ, T5EZ and T12EZ (Table 3.3 main text) also values for the MTSL-labelled EZ peptides are given. The MTSL-EZ peptides contain the spin-labelled cysteine at the N-terminus (M0EZ), at position 5 (M5EZ) and at position 12 (M12EZ), for sequences see Table 3.1 in the main text. All MTSL-constructs have shorter  $\tau_r$  than the TOAC counterparts, reflecting a higher local mobility of the MTSL label than the TOAC label. The difference in  $\tau_r$  is largest for T5EZ and M5EZ. The  $\tau_r$  value for T0EZ is half of that of T12EZ, as discussed in the main text. This shows that the backbone mobility is higher at the N-terminus than at the C-terminus of the EZ peptide. The rotational correlation times of M0EZ and M12EZ are the same within the experimental error, showing that local mobility, i.e. rotation about the single bonds linking the nitroxide to the backbone, masks backbone-mobility differences.

We tested the MTSL-labelled peptides for aggregation the same way as for the TOAC counterparts. The M0EZ peptide aggregated similarly to T0EZ. Similar to T5EZ and T12EZ, also M5EZ and M12EZ failed to aggregate. As MTSL labels do not break  $\beta$ -sheets, this finding shows that the inhibition of aggregation from crowding of the spin labels is more important than  $\beta$ -sheet breaking propensity of the TOAC.

### 3.6.3.5 Approximations used in oligomer size estimation

As described in the main text, the Stokes-Einstein relation establishes that  $\tau_r$  is proportional to the volume of the aggregate and, together with the protein density, it gives an estimate for the number of monomers in the aggregate. Utilizing this approach involves several approximations, the impact of which we describe in the following. Some of these approximations can be tested against the known structure of one of the oligomers expected for the EZ peptides: The hexamer cylindrin<sup>67</sup>. For this oligomer the X-ray structure is known and the rotational correlation times can be calculated from first principles by HYDRONMR<sup>125</sup>.

**Table S3.3** Size of oligomers from different methods and effects of approximations. Number of monomers in oligomer  $n_i$  and rotational correlation times ( $\tau_r$ ) are also given.

EPR component	$\tau_r$ from EPR [ns]	$\tau_r$ from HYDRONMR [ns]	method (i)		method (ii)
			$\rho = 1.35 \text{ g/cm}^3$	$\rho = 1.50 \text{ g/cm}^3$	
medium	$2.00 \pm 0.20$	$5.78^{\text{a}}$	4.52	5.03	5.81
slow	$6.31 \pm 0.70$	n.a.	14.27	15.88	18.31

a)  $\tau_1 = 4.96 \text{ ns}$ ;  $\tau_2 = 6.20 \text{ ns}$ ;  $\tau_3 = 6.16 \text{ ns}$

#### **Influence of protein density on values of $n_i$ (method (i))**

The protein density impacts  $n_i$  as seen in Table S3.3, comparing the two columns headed method (i). A value of  $\rho = 1.35 \text{ g/cm}^3$  (left column) is generally accepted for typical folded proteins ( $\text{MW} > 20 \text{ kDa}$ )<sup>110</sup> yielding the parameters that are also given in the main text, however, for proteins with progressively smaller MW, the density is increasing due to a larger relative impact of the hydration shell at lower protein volumes<sup>109</sup>. Thus a larger density ( $\rho = 1.5 \text{ g/cm}^3$ ) appears appropriate under some circumstances, and the resulting values are given in the right column<sup>110</sup>. Comparing the two columns, the oligomer sizes differ by 0.5 (medium fraction), resp. 1.5 (slow fraction) monomer units, showing that for the medium fraction the size approaches a pentamer. As the slow EPR fraction suggests a molecular weight of 23 kDa, the higher density does not seem appropriate for that fraction, showing that  $n_i$  for that fraction should be closer to a 14-mer than a 16-mer.

#### **Using monomer volume for cylindrin (method (ii))**

Method (ii) uses the volume of the monomer derived from the volume of the hexameric oligomer as obtained from x-ray crystallography<sup>67</sup>. It does not require the protein density. It results in a hexamer for the medium and a 18-mer for the slow fraction.



***Influence of the spherical approximation on  $n_i$*** 

The Stokes-Einstein relation (Eqn. 3.2, main text) implies a spherical object. For non-spherical objects the volumes derived from the Stokes-Einstein relation do not reflect the volume of the object accurately, as described here. Also, the lineshape of the EPR spectra can show systematic variations from those of a spherical object, and rather than by a single  $\tau_r$ , the isotropic  $\tau_r$  ( $\tau_0$ ), the anisotropic  $\tau_r$  values  $\tau_1$ ,  $\tau_2$  and  $\tau_3$  should be used.

The impact of any deviation of the shape of the oligomers from a sphere on the volume is estimated considering the theory of axially symmetric rotational ellipsoids. Axially symmetric rotational ellipsoids are described by the axis system  $a$ ,  $b$ ,  $c$ , where  $a$  is the semi-axis along the symmetry axis and  $b$  and  $c$  are perpendicular to it. For  $a > b$ , a prolate, and for  $a < b$ , an oblate ellipsoid results. The relation between  $\tau_r$  and the volume of such particles is described by Perrin et al.<sup>126</sup>, Koenig et al.<sup>127</sup> and summarized by Marsh and Horvath<sup>128</sup>. For cylindrin<sup>67</sup>, where the radius of the cylinder (11 Å) is equal to the half-height of the cylinder (total height 22 Å),  $b/a = 1$  results and Figure 1 of Koenig<sup>127</sup> shows that  $\tau_1$ , the rotation correlation time about the symmetry axis  $a$ , is 1.4 times larger than  $\tau_r$  of a sphere of the same volume ( $\tau_0$ ). Along the two equivalent axes  $\tau_r \approx \tau_0$ . The averaged  $\tau_r$  for such an ellipsoid could therefore be 1.3 times longer than that of a sphere. Thus the volume of the cylindrical ellipsoid would be 1.3 smaller than that of a sphere. For the smaller oligomers (medium  $\tau_r$  fraction from EPR) the number of monomers in the oligomers would reduce from five to four. The effect of other aspect ratios on  $\tau_r$  can be obtained from Figure 1 in Koenig<sup>127</sup>. In all cases, the  $\tau_r$  values of non-spherical objects are larger than those of a sphere of equivalent volume, suggesting a systematic over-estimation of the particle size in the spherical approximation. As the anisotropy of the rotation should be visible in the EPR spectra, EPR experiments at higher field/frequency values would help to determine the degree of anisotropy. Such experiments are beyond the scope of the present study.

***Influence of local mobility on oligomer size***

If the motion of the nitroxide is faster than that of the oligomer, the oligomer size determined by  $\tau_r$  would be smaller than the real value, an effect referred to as local mobility of the nitroxide. For proteins labelled conventionally with the MTSL label, Figure 3.1d, this is a severe problem. The nitroxide TOAC, Figure 3.1c, is part of the protein backbone, which will suppress local mobility effects considerably. The  $\tau_r$  of one of the EZ peptides (T5EZ) matches its volume (see Tab 3.3, main text) showing that local mobility at the center of the peptide is negligible, also, this  $\tau_r$  is significantly longer than that of M5EZ, emphasizing that the  $\tau_r$  of TOAC peptides is more closely correlated with the size of the object than for peptides labelled with MTSL. As described in the main text, the N-terminus of T0EZ must be somewhat flexible, so we cannot exclude that the size of the oligomer is somewhat underestimated. We are not aware of studies that have quantitatively analysed this point, in contrast to the situation for MTSL where extensive studies were performed by the Hubbell group<sup>47,129–133</sup>.

### ***Hydrodynamic simulations by HYDRONMR***

For K11V, the structure of one oligomer is known, so the  $\tau_r$  value for this structure can be calculated by HYDRONMR. The obtained  $\tau_r$  values give insight into the anisotropy of the rotation and absolute  $\tau_r$  values for the hexamer. In Tab. S3.3 these values are given: the anisotropy is relatively small and agrees well with an axially symmetric prolate object. The absolute isotropic  $\tau_r$  value is longer than calculated by methods (i) and (ii). Clearly, HYDRONMR provides a more realistic representation of the structure of the oligomer and of the hydration layer. The empirically derived protein densities take hydration into account, however, without considering the surface details of the protein and methods (i) and (ii) imply spherical approximation. The impact of the respective approaches for oligomers of the type observed here are difficult to assess. We observe that the  $\tau_r$  of the hexamer cylindrin from HYDRONMR is significantly longer than that of the medium fraction. There are two possible interpretations: Either, the medium fraction is due to a smaller oligomer than the cylindrin, or the faster  $\tau_r$  value observed experimentally is due to local mobility.

### ***Final assessment***

As far as the effect of the approximations of the approaches described can be quantified, the errors introduced are 1-1.5 monomer units per oligomer (e.g. method (i)). Some approximations lead to systematic deviations: Deviation of the oligomer from a sphere causes the oligomer size to be overestimated, local mobility causes the opposite effect and one could hope for some cancellation of errors. Conservatively, an estimate of 2-3 monomers units results for the absolute number of monomers in the oligomers, however, as several factors causing these uncertainties may be similar for some or all oligomers, relative sizes are more reliable and qualitative size distinctions can be made. In the main text, Discussion section, specialized experiments based on pulsed EPR and other techniques are described that can determine accurate oligomer sizes, however, most of these cannot be applied in situ. The present approach provides the overview of the entire aggregation process and can identify states of interest, e.g. how many distinct oligomer states there are, and what the relative sizes of oligomers are. Once established, these states can be investigated more quantitatively by the methods referred above.

### 3.6.3.6 Can single monomer resolution of oligomer size be attained?

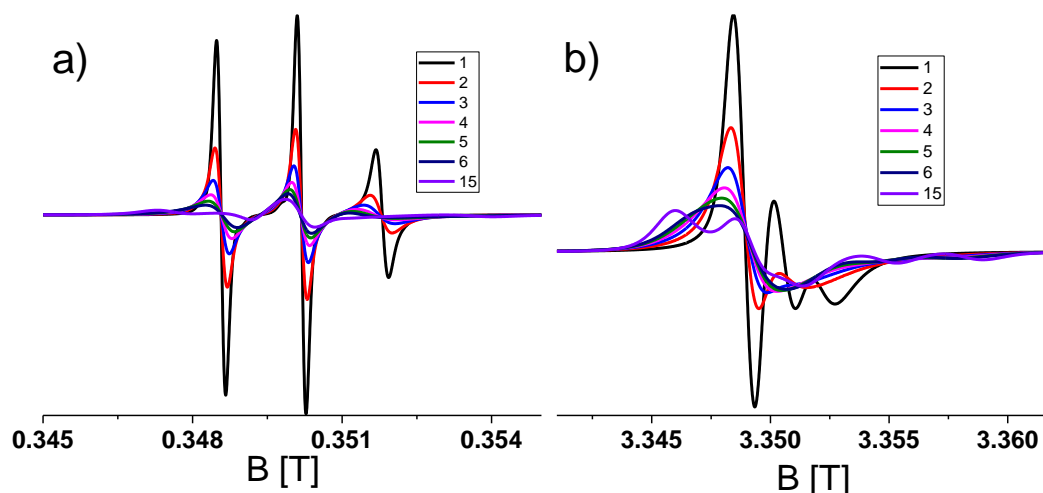


**Figure S3.6** Simulations of EPR spectra of T0EZ for the expected volumes of different sized oligomers, one monomer at a time. The  $\tau_r$  values were calculated based on the  $V_{MW}$  using the same parameters as for the simulations of the experimental spectra (see Material and Methods in the main text). a) Simulations of 9 GHz spectra of a molecule with rotational correlation times ranging from 1.8 ns (black) to 26.7 ns (purple). b) Simulations of 95 GHz spectra for the same rotational correlation times.

Figure S3.6 shows the 9 GHz and 95 GHz EPR spectra expected for oligomers of different sizes in single-monomer increments. Sizes range from 1 to 15 mer aggregates. Peptide volume used:  $V_{MW}$  of T0EZ. Especially in the 95 GHz EPR spectra, the differentiating power of the method is high: Monomers are clearly set off from dimers, and up to hexamers individual species can clearly be distinguished in the low- and high-field region of the spectra. Similarly, resolving oligomers from hepta- to 15 mers should be possible, but it is not shown here for clarity.



## **4 In situ kinetic measurements of $\alpha$ -synuclein aggregation reveal large population of short-lived oligomers**

Knowledge of the mechanisms of assembly of amyloid proteins into aggregates is of central importance in building an understanding of neurodegenerative disease. Given that oligomeric intermediates formed during the aggregation reaction are believed to be the major toxic species, methods to track such intermediates are clearly needed. Here we present a method, electron paramagnetic resonance (EPR), by which the amount of intermediates can be measured over the course of the aggregation, directly in the reacting solution, without the need for separation. We use this approach to investigate the aggregation of  $\alpha$ -synuclein ( $\alpha$ S), a synaptic protein implicated in Parkinson's disease and find a large population of oligomeric species. Our results show that these are primary oligomers, formed directly from monomeric species, rather than oligomers formed by secondary nucleation processes, and that they are short-lived, the majority of them dissociates rather than converts to fibrils. As demonstrated here, EPR offers the means to detect such short-lived intermediate species directly in situ. As it relies only on the change in size of the detected species, it will be applicable to a wide range of self-assembling systems, making accessible the kinetics of intermediates and thus allowing the determination of their rates of formation and conversion, key processes in the self-assembly reaction.

## 4.1 Introduction

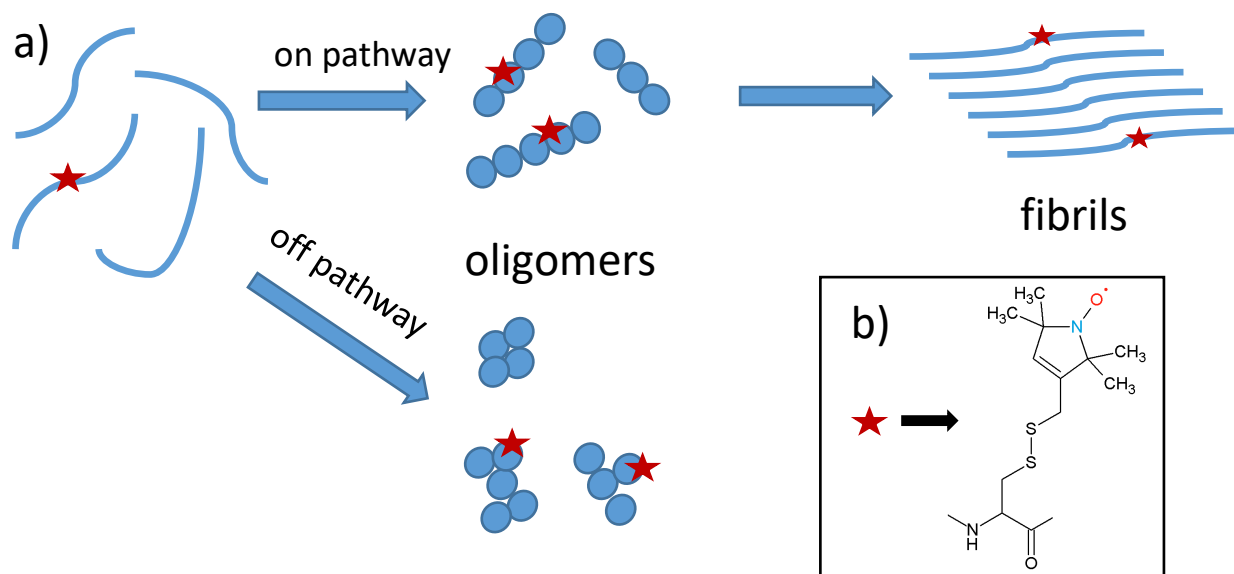


**Figure 4.1** a) Overall reaction pathways and intermediates of  $\alpha$ -synuclein aggregation shown schematically. Blue spheres: monomers within oligomers (shapes of oligomers are arbitrary). Red stars: R1 nitroxide spin label (see b). b) Molecular structure of the R1 spin label attached to the protein.

The function of the  $\alpha$ -synuclein protein ( $\alpha$ S) is associated with its ability to bind to the membranes of intracellular vesicles and thought to involve membrane remodeling and vesicle trafficking. It mainly localizes at the synaptic terminus where it plays a role in synaptic transmission.<sup>134</sup> The binding of  $\alpha$ S to membranes may directly contribute to membrane remodeling by generating curvature or indirectly by acting as a non-conventional chaperone for the SNARE protein synaptobrevin.<sup>135</sup> Additionally the propensity of  $\alpha$ S to connect vesicles plays a role in vesicle trafficking at the synapse by controlling the distal synaptic vesicle pool.<sup>136</sup>

While the exact functions of the  $\alpha$ S protein only now start to become clear, its association with Parkinson's disease has been well documented. The *in vitro* aggregation of  $\alpha$ S revealed that besides the cross- $\beta$  fibrils, which represent the end-point of the amyloid aggregation, oligomers are also formed.<sup>137–143</sup> Several works have shown that these oligomeric species are toxic to cells<sup>38,39</sup>, however, most studies rely either on fluorescently labelled  $\alpha$ S species, use kinetically trapped oligomers which may not constitute intermediates of the aggregation reaction, or involve biochemically isolated oligomers and indirect detection.<sup>144–147</sup>

While these approaches are invaluable for structural and toxicological studies, they cannot detect the oligomers *in situ*, to reveal how the oligomers develop in the aggregating solution. Also labelling and isolation may cause a significant modification of the protein or oligomer structure. Thus, there is need for methods to detect such intermediates, directly in solution during the aggregation reaction, without the need for large fluorescence labels. Here we present an approach that closes this gap: *In situ*

continuous wave electron paramagnetic resonance (EPR). This method measures the rotational diffusion time of spin labelled objects in liquid solution at room temperature. Sensitivity of the EPR lineshape of nitroxide spin labels to time scales in the nano-second regime ensures that the aggregates of interest (see Figure 4.1) are well covered. To apply the method, the  $\alpha$ S is labelled with the spin label shown in Figure 4.1b. This label is attached to a cysteine at position 56, which was introduced by site selective mutagenesis, resulting in the construct R1- $\alpha$ S, where R1 stands for the spin label. The spin label itself, see Figure 4.1b, is significantly smaller than commonly used fluorescent labels. The scarceness of unpaired electrons makes the method background free.

We use this methodology to reveal the appearance of an intermediate aggregated species. We present a kinetic model that explains the development of intermediates and fibrils.

## 4.2 Material and methods

### 4.2.1 Protein expression and labeling

Mutagenesis, protein expression and purification were performed as described previously.<sup>148,149</sup> The mutated protein was spin labeled following a standard protocol. The  $\alpha$ S56 (cysteine mutant in position 56) was reduced with a six-fold molar excess per cysteine with DTT (1,4-dithio-D-threitol) for 30 minutes at room temperature. Removal of DTT was done by passing the samples twice through a Pierce Zeba 5 ml desalting columns. Immediately afterwards, a ten-fold molar excess of the MTSL spin label [(1-oxyl-2,2,5,5-tetramethylpyrroline-3-methyl)-methanethiosulfonate] was added (from a 25 mM stock solution in DMSO) and incubated for one hour in the dark at room temperature. After this, free spin label was removed by two additional desalting steps. Protein samples were applied onto Microcon YM-100 spin columns to remove any precipitated and/or oligomerised proteins and then diluted in buffer (10 mM Tris-HCl, pH 7.4). The initial protein concentration was 250  $\mu$ M, the spin label concentration was 2.5 mM. Due to the high reactivity of the MTSL and the easily accessible cysteine, near stoichiometric labeling was achieved under these conditions.<sup>150</sup> Samples were stored at -80 °C.

### 4.2.2 Sample preparation

Three aliquots of a stock solution of spin-labeled  $\alpha$ -synuclein (concentration between 150  $\mu$ M and 250  $\mu$ M) were diluted in 1.5 mL of buffer each (10 mM Tris-HCl, pH 7.4), to a final concentration of 10  $\mu$ M. The solutions also contained 90  $\mu$ M wild-type  $\alpha$ -synuclein for diamagnetic dilution. The experiments were carried out over five days. After an initial

## Chapter 4

measurement was taken at the time the spin-labelled protein was diluted ( $t = 0$ ), the samples were allowed to aggregate in 2 mL Eppendorf tubes on a thermomixer (Eppendorf, Thermomixer comfort) with a speed of 1000 rpm at 37 °C. At each time point, 40  $\mu$ L samples were drawn from the aggregation solution and kept in the fridge at 4 °C. From these, samples for EPR and Thioflavin T (ThT) fluorescence measurements were made. At the beginning samples were collected every 3 hours, at later times the intervals were longer (see text).

### 4.2.3 EPR measurement conditions

The 9 GHz, continuous-wave EPR spectra were recorded using an ELEXSYS E680 spectrometer (Bruker, Rheinstetten, Germany). The measurements were done under the following conditions: room temperature, a microwave power of 0.63 mW and a modulation amplitude of 0.25 mT at a modulation frequency of 100 kHz. The time expended on each measurement was adapted according to the spectral lineshape, i.e., the aggregation time, and they could last from 3 to 8 hours. Glass micropipettes of a volume of 50  $\mu$ L (Blaubrand Intramark, Wertheim, Germany) were filled with 20  $\mu$ L of the sample for each measurement. The spin concentration was determined by comparing the double integral of the EPR spectra with the double integral of a reference sample (MTSL, 100  $\mu$ M). The spin concentrations were  $\approx 10$   $\mu$ M for a total protein concentration of 100  $\mu$ M.

### 4.2.4 Simulations of EPR spectra

MATLAB (version 9.4.0.813654, R2018a, The MathWorks, Inc., Natick, MA, USA) and the EasySpin package (5.2.4) were used for simulations of the EPR spectra.<sup>48</sup> The parameters of the simulation were manually adjusted to agree best with the experimental spectra. For all simulations, an isotropic rotation of the nitroxide ( $S = 1/2$ ) was utilized. The following g-tensor values were used:  $g = [2.00906 \ 2.00687 \ 2.00300]$ . These values were obtained in previous experiments<sup>151</sup> and we used these values for the simulations presented here. The spectra were simulated with a superposition of four components: two fast fractions using the “Garlic” function and a medium and a slow fraction using the “Chili” function. The principal values of the  $^{14}\text{N}$  hyperfine coupling tensor were  $A_{xx} = A_{yy} = 13$  MHz and  $A_{zz} = 110$  MHz. For the slow component  $A_{zz} = 106$  MHz was used instead. A Gaussian component with a linewidth of 0.12 mT was used for all simulations. The spectrum obtained at  $t = 0$  could be simulated with a single component, the fast fraction. The  $\tau_r$  obtained at  $t = 0$  was kept constant for all other simulations. From  $t = 3$  hours a new component appeared,  $\tau_r = 0.24$  ns which we attribute to free spin label. Its contribution to the spectra never exceeded 10 %. Optimal  $\tau_r$  values of the medium and



slow components were derived from later time-point spectra and then kept constant for the entire series. For each time point, the relative contribution of the four components was optimized considering all time points.

### 4.2.5 Fitting of kinetics

The EPR measurements yield, after processing, the monomer-equivalent concentrations of monomers, intermediates and fibrils at different time points. We fit a minimal model of the aggregation of  $\alpha$ S into fibrils that additionally includes the formation of oligomers of size  $n$  directly from monomers with rate constant  $k_o$ . Oligomer dissociation proceeds at rate constant  $k_d$ . Oligomers can be converted to fibrils by rate constant  $k_c$ . Fibrils grow by addition of monomers to their ends with rate constants  $k_+$  and we allow for the presence of secondary processes, i.e. the possibility of fibrils to multiply in a monomer-independent manner, e.g. by fragmentation, by rate constant  $k_2$ . We do not include oligomeric species formed by a secondary process. More detailed descriptions of these kinetic models can be found for example in Meisl et al.<sup>152–154</sup>

Invoking conservation of mass,  $m_{tot} = m(t) + M(t) + O(t)$ , the aggregation process can be described by the following set of differential equations:

$$P'(t) = k_c O(t) + k_2 (m_{tot} - n O(t) - m(t))$$

$$M'(t) = 2k_+ P(t)m(t)$$

$$m'(t) = -2k_+ P(t)m(t) - nk_o m(t)^n + nk_d O(t)$$

$$O'(t) = k_o m(t)^n - (k_c + k_d)O(t)$$

Where  $M(t)$  is the monomer-equivalent concentration of fibrils,  $P(t)$  and  $O(t)$  are the number concentrations of fibrils and of oligomers, respectively and  $m(t)$  is the free monomer concentration. These equations were numerically integrated and fitted to the data by least squares minimization. We assumed a monomer-concentration independent secondary mechanism, such as fragmentation, based on previous studies of  $\alpha$ S<sup>155</sup> aggregation into amyloid fibrils and the fact that vigorous shaking tends to induce fragmentation<sup>156</sup>. Additionally, given that the experiments were only recorded at a single initial monomer concentration, they do not provide strong constraints on the reaction orders<sup>154</sup>. The data provide constraints for a number of parameters: oligomers are in fast equilibrium with monomers, thus the equilibrium constant,  $k_o/k_d$  can be determined accurately but only an approximate lower bound can be given for the individual rates (corresponding to the requirement that the oligomerization reaction proceed fast enough to be in effective equilibrium relative to monomer depletion). Equally, the rates of elongation, the secondary process and conversion are interdependent (as is the case in all unseeded aggregation reactions) and thus only the products  $k_+k_c$  and  $k_+k_2$  can be

constrained. Finally, the data show only a weak dependence on the reaction order of the oligomerization reaction,  $n$ .

## 4.3 Results

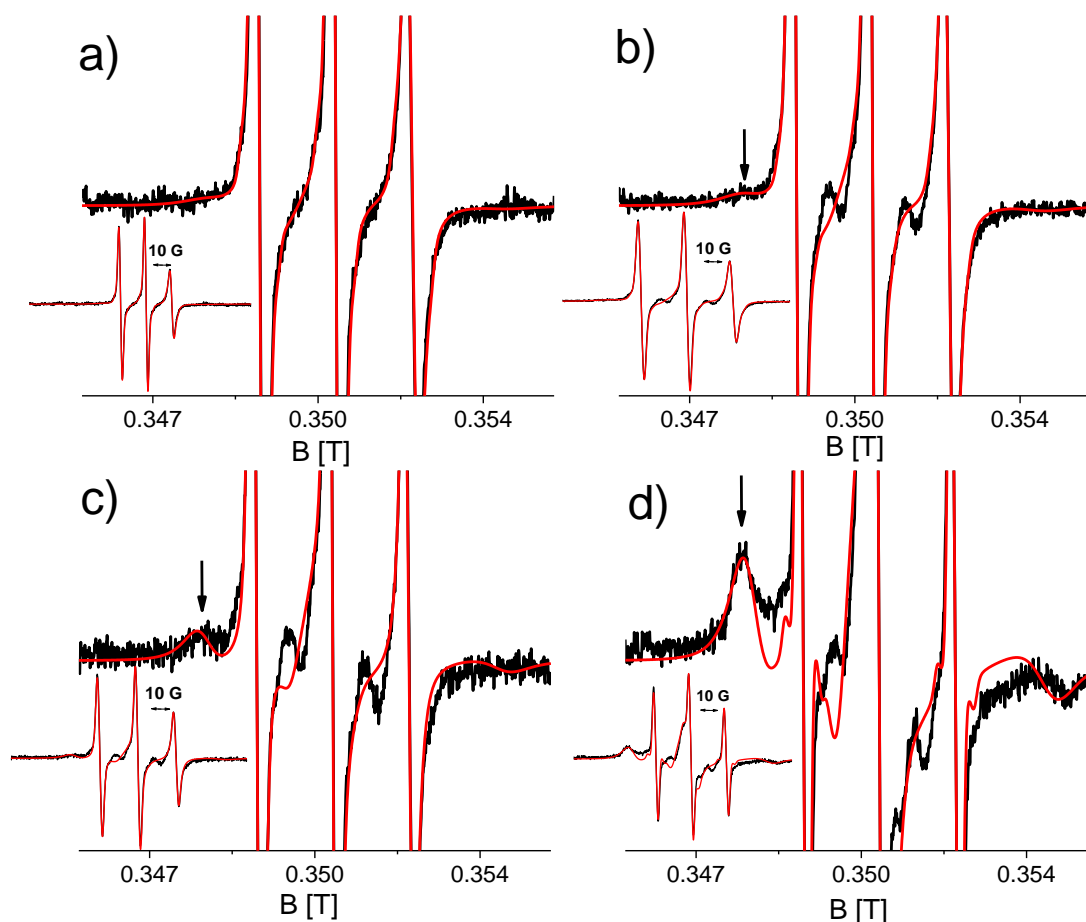


**Figure 4.2** Room temperature EPR spectra of  $\alpha$ -synuclein at different time points of aggregation. Full spectra: Inset. Zoomed-in spectra: Amplitude expanded four-fold with respect to inset. a) Start of aggregation ( $t = 0$ ). b) 9 hours of aggregation. c) 24 hours of aggregation. d) 42 hours of aggregation. Black: Experimental spectra. Red: Simulated spectra. Arrow: feature of broad spectral component (see text).

The aggregation of 100  $\mu$ M  $\alpha$ -synuclein was monitored at pH 7.4 and 37  $^{\circ}$ C under rapid shaking (1000 rpm), over the course of 120 hours. Figure 4.2 shows the development of the EPR spectra of R1- $\alpha$ S over time for four selected time points. The spectra at the start of the aggregation and after nine hours of aggregation (9 h) are dominated by the three narrow lines typical of nitroxides in fast rotational motion.

Starting at nine hours a new component with a broader linewidth (marked by an arrow) develops, that increases in amplitude with time. Its lineshape is due to a nitroxide with a slower rotation and shows that a fraction of R1- $\alpha$ S becomes more immobilized as the

## Chapter 4

aggregation progresses. Line broadening by spin-spin interaction can be excluded, because the R1- $\alpha$ S was diluted in a 1 : 9 ratio with wt- $\alpha$ S, which increases the distance between the spins of the nitroxides sufficiently to suppress spectral effects of their interaction (diamagnetic dilution).

**Table 4.1** Rotation correlation time ( $\tau_r$ ) of R1- $\alpha$ S in the three fractions observed by EPR.

	fast	medium	slow
$\tau_r$ (ns)	0.40	4.00	10

By spectral simulation<sup>48</sup> three components can be extracted, referred to as the fast, medium and slow components. Their respective rotation correlation times ( $\tau_r$ ) are given in Tab. 4.1, and their lineshape is shown in Figure S4.2. The  $\tau_r$  value of the fast fraction agrees with the  $\tau_r$  values of monomeric  $\alpha$ S with the spin label at the position of R1- $\alpha$ S.<sup>157</sup> The amount by which each fraction contributes to the spectra is shown in Figure 4.3.

The magnitude of  $\tau_r$  relates to the size of the aggregated species, where, qualitatively, a longer  $\tau_r$  corresponds to a larger species, see for example M. Hashemi Shabestari et al.<sup>65</sup>. Therefore, the medium fraction can be attributed to smaller aggregates than the slow fraction.

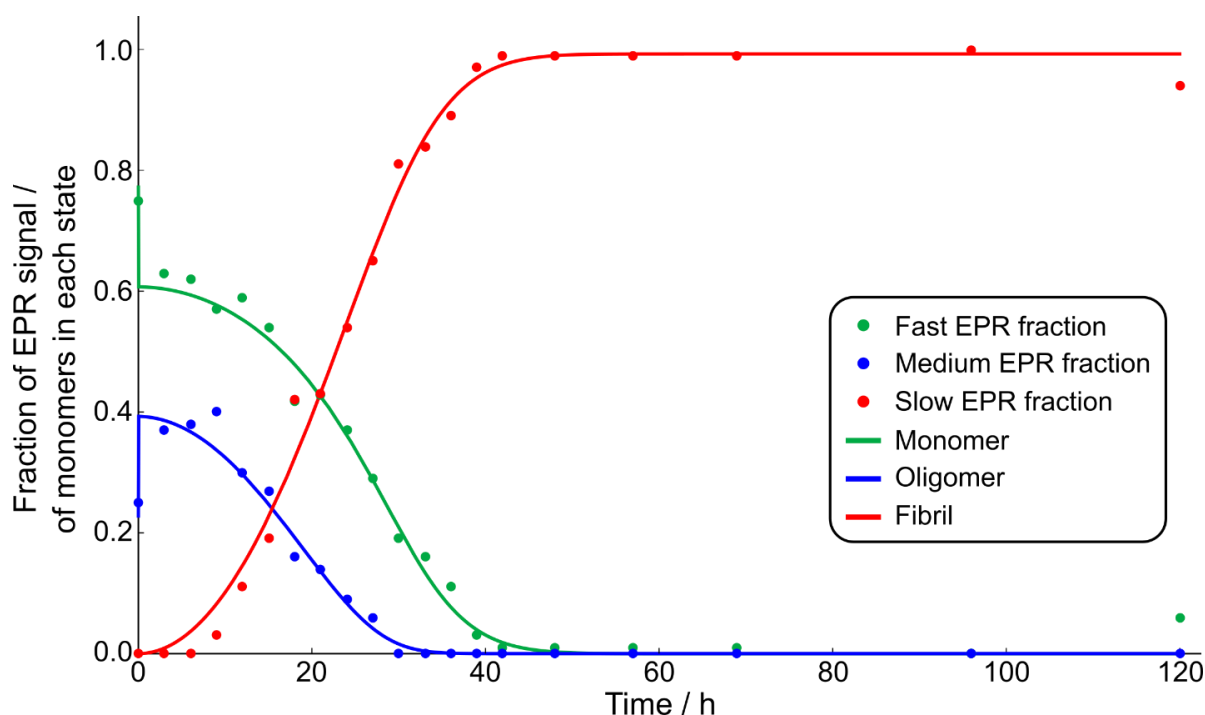


**Figure 4.3** Aggregation of  $\alpha$ -synuclein as a function of time derived from EPR. Amount of fast fraction (green dots) caused by monomers. Amount of medium fraction (blue dots) assigned to oligomers. Amount of slow fraction (red dots) assigned to fibrils. The solid lines are the fractions of monomer, oligomer and fibrils predicted from the best fit of the model, with an oligomer size of  $n=3$ .

## Chapter 4

The fast component decays to zero within the first 40 hours. The medium fraction increases to a maximum value of 40 % within the first 10 hours and then decays. At 30 hours, this component has fully decayed. The medium fraction disappears before the monomer fraction is depleted. The slow fraction appears after 12 hours, it increases to reach 100 % at 40 hours, and then remains at its plateau level until the end of the measurements, at 120 hours.

The kinetics of monomer, fibrillar and oligomeric fractions determined in this way were used in a kinetic analysis to determine the mechanism of aggregation and the respective reaction rates. The minimal model that was able to describe the data included an oligomeric species, formed directly from monomer, that can convert to growth-competent fibrils in a unimolecular reaction. Fibrils grow by addition of monomer and existing fibrils can lead to the formation of new fibrils via a secondary process, but they do not significantly affect the production of oligomers.

### 4.4 Discussion

Methods to determine the time course of amyloid aggregation are important as intermediates of aggregation are believed to be key toxic species<sup>38,39,158–160</sup>. Here we focus on  $\alpha$ S, an amyloid protein related to Parkinson's disease, whose physiological role is yet to be determined.

Under the conditions investigated here,  $\alpha$ S is expected to fibrilize slowly, i.e. over the course of days. We track the aggregation of  $\alpha$ -synuclein in situ by EPR lineshape changes, which reflect the mobility of the spin label in R1- $\alpha$ S.

Following the time course of the process over the period of 5 days, three distinct fractions are observed: A fast fraction is due to monomeric R1- $\alpha$ S. The fast fraction decays with time and at 40 hours has disappeared. The second fraction, with medium mobility, grows with time with a maximum early in the aggregation reaction followed by a decay. The transientness of this species suggests that this fraction represents oligomers which are higher in energy than the fibrillar end product of the aggregation reaction. The slow fraction appears after a lag time and then grows to a plateau value that is close to the full population.

#### ***4.4.1 Relation of the EPR derived fractions to the aggregation state of $\alpha$ S***

The contribution to the overall EPR signal reflects the relative number of  $\alpha$ S proteins in this particular aggregation state. Thus, the fraction with a fast rotational correlation time

corresponds to the fraction of total  $\alpha S$  that is in the monomeric state. This signal shows a decay over time as monomers are being converted into aggregates. In addition to the monomeric species, two types of aggregates can be distinguished by EPR, those with a slow rotational correlation time, corresponding to large aggregates and those with a medium rotational correlation time, corresponding to intermediate aggregate sizes. The time dependence (Figure 4.3) shows that intermediate-sized aggregates are formed initially, their time course closely resembling that of the monomer after the initial measurement. The larger aggregates are only formed at a later stage.

It is not possible to derive the exact size of the aggregate, because of the local mobility of the spin label, i.e. the rotation about the single bonds that link the pyrrolidine ring to the protein backbone (Figure 4.1 b), see M. Hashemi Shabestari et al.<sup>65</sup> for a more detailed discussion. In the present context, a lower limit of the size of the aggregate can be estimated from the ratio of the  $\tau_r$  values of the aggregates with respect to the monomer, showing that the medium fraction comprises minimally ten monomers, the slow fraction at least 25 monomers. We have discussed the factors entering such estimates in detail in M. Hashemi Shabestari et al.<sup>65</sup>

The exponential increase of ThT activity appears around 35 hours (Figure S4.1), consistent with the medium fraction consisting of non-fibrillar aggregates. The slight discrepancy between the appearance in time of the large aggregate fraction as measured by EPR and the ThT fluorescence (Figure S4.1) is likely due to the poor sensitivity of ThT for structures with less beta-sheet content (see SI). Thus, we will refer to the medium fraction as oligomeric and the slow fraction as fibrillar.

Based on these observations we propose the following reaction scheme: Oligomers of size  $n$  form directly from monomers with rate constant  $k_o$  and dissociate with rate constant  $k_d$ . They can be converted to fibrils by rate constant  $k_c$ . Fibrils in turn grow by addition of monomers to their ends with rate constants  $k_+$  and we allow for the presence of a monomer-concentration independent secondary process, such as fibril fragmentation, by rate constant  $k_2$ . Based on the EPR data, the oligomeric species appear to be in fast equilibrium with monomers on the timescale of the aggregation reaction. Indeed, we find that the rates of oligomer formation and dissociation are fast with  $k_d > 1 \text{ h}^{-1}$  and only their equilibrium ratio being well constrained. Therefore, monomeric and oligomeric species should be considered part of the same ensemble of reactants for the purposes of a kinetic description. In other words, whether new fibrils are formed directly from monomers or by conversion of oligomeric intermediates is thus not distinguishable based on these kinetic measurements alone. The data are best fit by an oligomer reaction order of  $n=3$  (see Figure 4.3), but the dependence of the goodness of fits on this reaction order is weak, and reasonable fits can be achieved also with  $n=10$ , the lower limit predicted for the oligomer size based on our EPR data alone (see Figure S4.3). It is worth noting that a kinetic analysis as presented here yields reaction orders, rather than oligomer sizes directly. In the simplest interpretation, i.e. when the reaction modelled is a single elementary step, the reaction order is equivalent to the oligomer size. However, in more

## Chapter 4

complex reactions, e.g. when heterogeneous nucleation on a surface is involved, reaction orders can be significantly smaller than the oligomer size. Assuming  $n = 3$ , the best fit yields  $k_d > 1 \text{ h}^{-1}$  and  $k_o/k_d = 5.8 \times 10^7 \text{ M}^{-2}$ ,  $k_+k_2 = 55 \text{ M}^{-1}\text{h}^{-2}$  and  $k_+k_c = 130 \text{ M}^{-1}\text{h}^{-2}$ . Note that only the combined rates of nucleation and elongation can be constrained; this is a result of the fact that measurements of the mass concentration of aggregates in the absence of seeds are determined only by a product of these rates, rather than the individual rates.<sup>22</sup> Typical elongation rates are on the order of  $10^6 \text{ M}^{-1}\text{h}^{-1}$ ,<sup>161</sup> thus conversion,  $k_c$ , is likely to be orders of magnitude slower than dissociation,  $k_d$ . A key result is that the oligomers are formed directly from monomer, also in the absence of fibrils, and thus constitute primary oligomers, rather than secondary oligomers, i.e. they are potential intermediates of primary nucleation, not of secondary nucleation, as observed for example in the aggregation of A $\beta$ 42, one of the main proteins that aggregate in Alzheimer's disease. Furthermore, the fast oligomer dissociation rate compared to rate of conversion of oligomers into fibrils, as well as the fact that oligomers are in equilibrium with monomers, indicates that most oligomers dissociate before they can convert into fibrils. In Cremades et al.<sup>10</sup> two types of oligomers were identified, type A and type B. Type A oligomers are smaller and dissociate more readily than type B ones and both types dissociate more slowly than the oligomeric species we observe here. Thus, while the dynamics of the oligomer fraction observed here more closely resembles that of type A than type B oligomers of Cremades et al.<sup>10</sup>, the majority of oligomers we detect do not appear to be present in single molecule experiments. While the different label may play a role, the fact that our technique requires neither dilution nor separation is likely to be the main source of the observed differences. Given our finding of a fast dissociation rate, we would expect the oligomeric species we detect here in-situ to dissociate significantly upon dilution, which is required to obtain single molecule data. The in-situ measurement by EPR allows us to detect these meta-stable species which are too short-lived to be measured by other techniques.

## 4.5 Conclusion

We have demonstrated the power of EPR to measure the presence of oligomeric species over the time course of the aggregation reaction, without need for dilution, size exclusion or other techniques that could potentially alter the size distribution. We find that a large population of non-ThT active intermediates form during the aggregation of  $\alpha$ S at pH 7.4 and 37 °C. These oligomeric species are in fast exchange with the monomer pool and thus the data are consistent with them being intermediates on the primary nucleation pathway. They are not consistent with the detected species being secondary oligomers, i.e. formed via a process that is catalyzed by existing fibrils, which is believed to be the main source of oligomers during the aggregation of A $\beta$ 42. Oligomers are short lived on the timescale of the aggregation reaction and most disappear by dissociation, not by conversion to fibrils. We envision that this combination of non-disruptive oligomer

detection and kinetic analysis will be applicable to study the effect of a range of conditions on the oligomer formation reaction of  $\alpha$ S and other amyloid forming proteins.

## 4.6 Supporting information

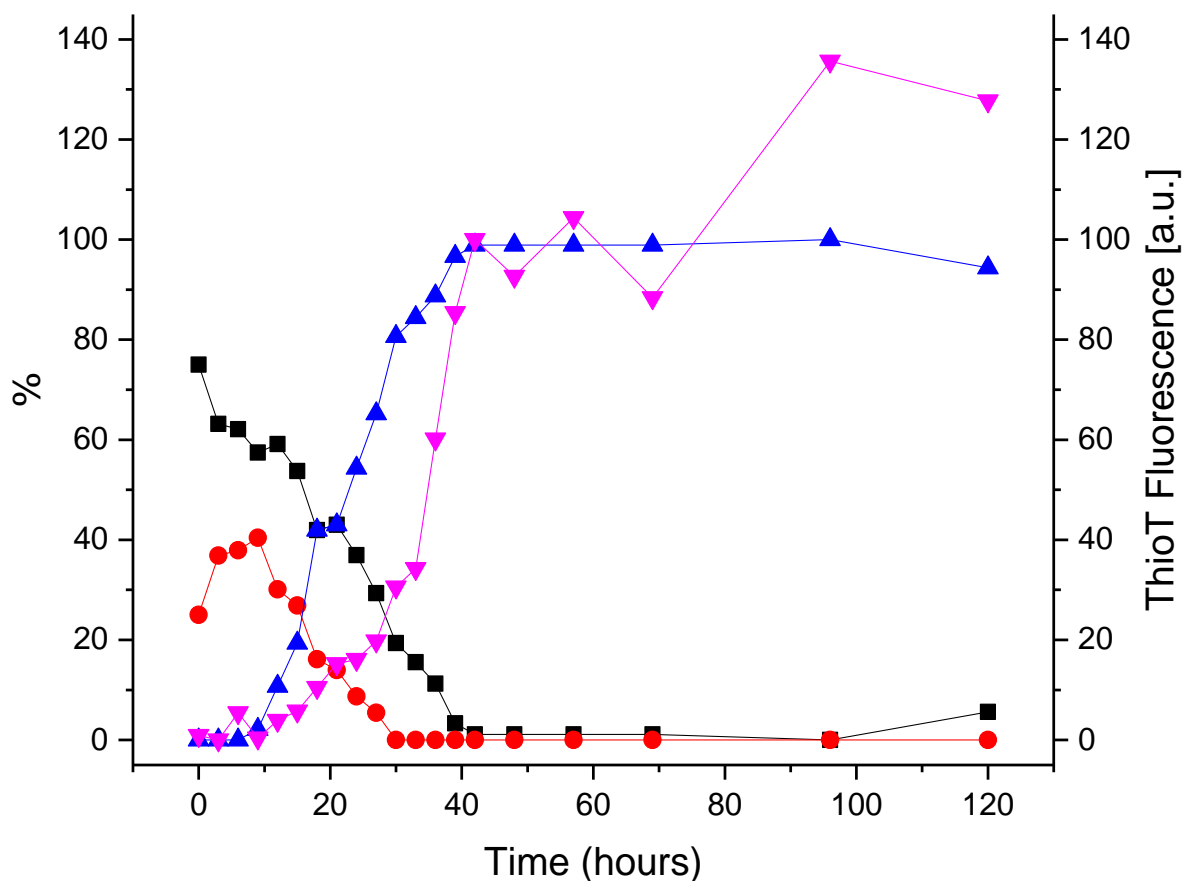


**Figure S4.1** Aggregation of  $\alpha$ -synuclein as a function of time. Amount of fast fraction (black) caused by monomers. Amount of medium fraction (blue) assigned to oligomers. Amount of slow fraction (red) assigned to fibrils. Amount of fibrils derived from ThT fluorescence (pink, normalized to 100 at time 42 hours, the presumed plateau value). A 10 % component of free spin label was subtracted from the spectra from 3 to 120 hours. The lines are a guide to the eye.

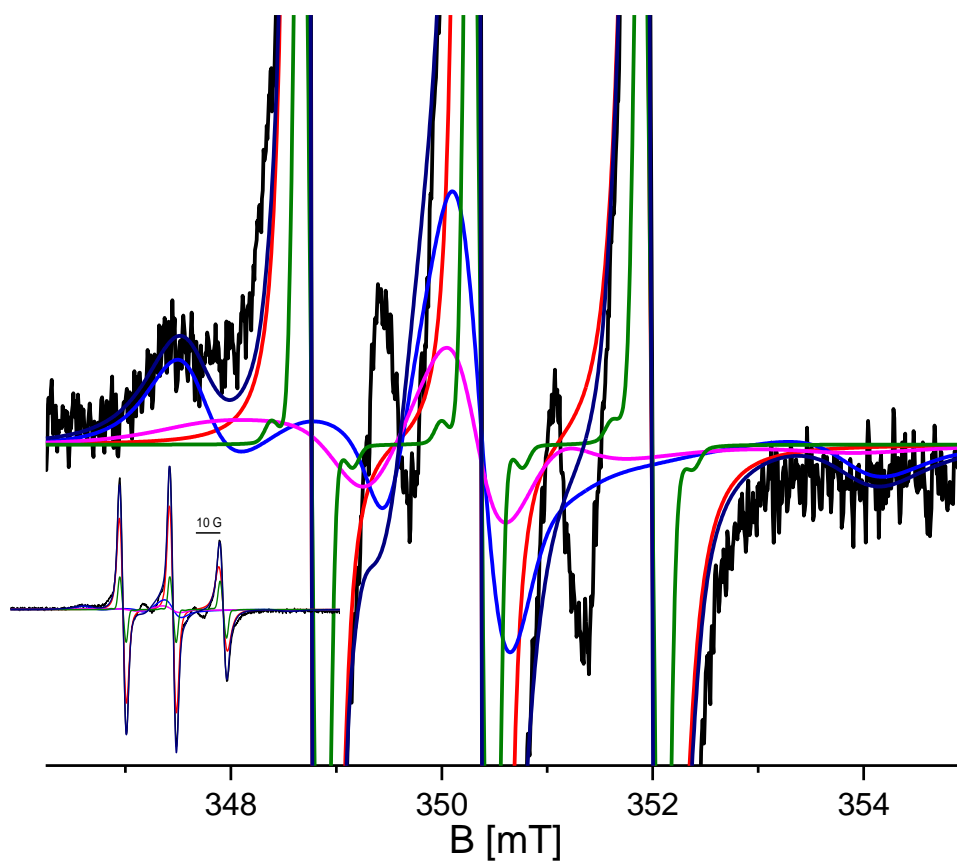


**Figure S4.2** Spectral components used in the simulation of the EPR spectra of  $\alpha$ -synuclein (18 hours of aggregation). Full spectra: Inset. Zoomed-in spectra: Amplitude expanded ten-fold with respect to inset. Experimental spectra (black), fast component (red), medium component (pink), slow component (blue), free spin label (green). Total simulation (navy). For details see text.



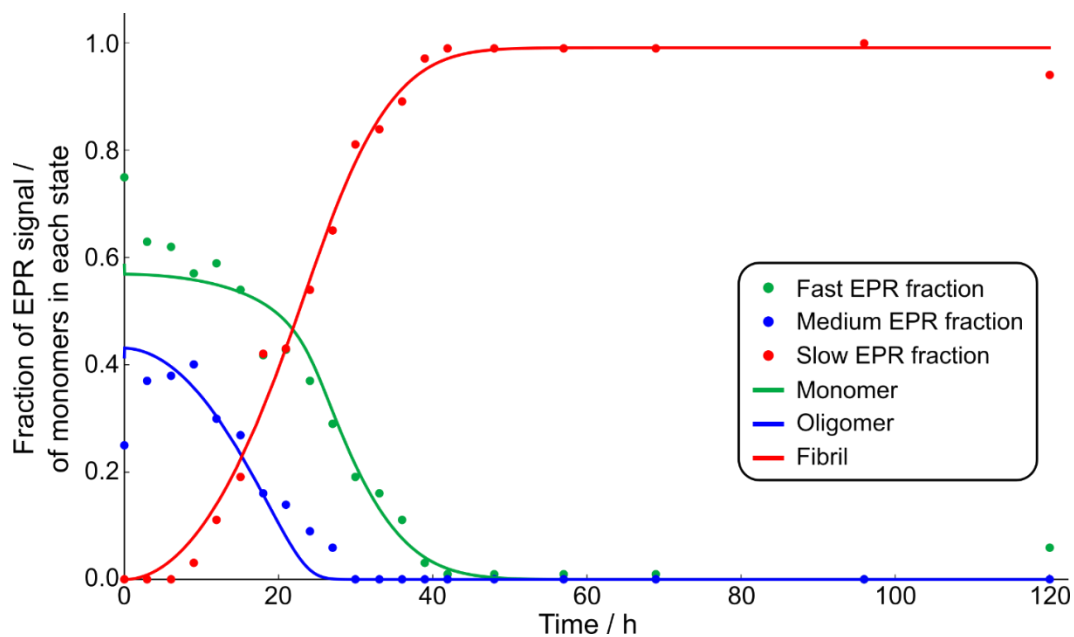


**Figure S4.3** Fits of the EPR data as in Figure 4.2, but with the oligomer size set to  $n=10$ . While the fibrils time course matches equally well with the data as for  $n=3$ , the fits to the monomer and oligomer populations are significantly worse.



## 5 A two-armed probe for in-cell DEER measurements on protein

The double electron-electron resonance (DEER) technique combined with site-directed spin labeling (SDSL) is a popular method for bio-molecular structure studies. The application of DEER to protein systems within living cells puts rigorous restraints on the spin-label. The probe needs to be immobilized relative to the protein and both the linkage and the paramagnetic center need to be stable under the reducing conditions of the cell. Here, three two-armed Gd(III) complexes, Gd(III)-CLaNP13a/b/c, which differ in the length of the arms that links the Gd(III) chelating cage to the protein, were synthesized. Rather than the disulphide linkage employed for protein attachment in most other CLaNP molecules, thioether linkage is used here. We doubly labeled the N55C/V57C/K147C/T151C variant of T4Lysozyme and performed paramagnetic 95 GHz DEER on these constructs. DEER experiments for spin-labeled variants of T4 lysozyme were performed in buffer, in cell lysate and in *D. discoideum* cells. A narrow distance distribution was detected for all constructs. The DEER derived distances are on the order of 4.5 nm and are in agreement with the expected values based on the metal ion positions derived from paramagnetic NMR results. The results indicate that the probes are mostly rigid relative to the protein due to the dual attachment sites. The thioether linkages make the probes suitable for in-cell protein studies.

## 5.1 Introduction

The studies about the structure of proteins are most commonly performed *in vitro* on isolated and purified protein samples. However, the proteins in a natural environment are subjected to much more complex conditions, for example due to the interaction with a vast range of other molecules and proteins or under other factors that are strongly dissimilar from an aqueous solution. Therefore, recent studies are focused into finding alternative ways to investigate the activity of the proteins in environments which resemble the natural ones, for example in cell lysate or directly within a cell. Electron Paramagnetic Resonance (EPR) is a technique which has seen an increase of interest due to its ability to study these systems under such conditions<sup>56,162,163</sup>.

Double electron-electron resonance (DEER) spectroscopy, also known as pulsed electron-electron double resonance (PELDOR), is a pulsed EPR method that measures, through the dipolar electron-electron coupling between two paramagnetic species, distances in the range of 1.5–8 nm, and up to 16 nm under special perdeuterated conditions<sup>55,58,163–166</sup>. This technique is characterized by high precision and reliability, and beyond mere mean distances, DEER yields distance distributions, which provide information about conformational distributions and dynamics. Because most cell components are diamagnetic, EPR-based distance determination inside cells is virtually background-free. DEER spectroscopy is the commonly used technique to perform such *in-cell* distance determination<sup>167–170</sup>. It must be taken into account that in most cases the proteins of interest are also diamagnetic, thus it is important to find suitable tags to be added to perform EPR.

Conventionally, DEER measurements are performed between two nitroxide spin labels ( $m_s = \pm 1/2$ ) that have been attached to biological molecules either by site-directed spin labeling or by chemical modification, however such labels have problems due to their reactivity and the strongly reducing environment to which they are subjected in natural cells<sup>167</sup>. Therefore, in recent years, research was focused into developing new probes where both the spin-label itself and the bond linking the probe to the protein are resistant to reduction and as rigid as possible.

Complexes of Gd(III) ( $S = 7/2$ ) with chelating ligands are ideal candidates for *in-cell* EPR<sup>171,172</sup> at high frequencies (e.g., 95 GHz), and feature low toxicity, high stability, suitable spin relaxation times and no orientation selection. The most efficient Gd(III) spin label should exhibit a chemically stable conjugation to the protein in biological environment, a high binding constant to the metal ion to prevent leakage of Gd(III) from the complex especially in *in-cell* environments, a narrow central transition ( $m_s = \pm 1/2$ ) and a long phase memory time for sensitivity in relation to long-distance measurements, and a rigid ligand to bind it to the protein for high-distance resolution. Considering the last point, the labeling site should be carefully chosen to ensure that the tag efficiently attaches to the protein and its rigidity does not interfere with the protein structure and

functionality. Previous research has shown that in a maleimide functional group conjugated to a cysteine residue the C-S bond between the cysteine and the maleimide group, unlike a commonly used disulphide bridge, was resistant to reduction<sup>168,169</sup>, although the flexibility of the linker gave rise to a wide distance distribution. Different strategies have been applied to reduce the mobility of the tag, such as using more rigid attachment groups or attaching the probe via two arms linkers to the protein.<sup>173-175</sup>

In this study we investigated the properties of three recently developed Gd(III) labeling tags, Gd-CLaNP13i (i = a,b,c) attached to the Bacteriophage T4-Lysozyme mutant T4Lys N55C/V57C/K147C/T151C. Such tags have the characteristic of using the maleimide group for attachment to the protein and of being equipped with two arms clamping the Gd(III) to achieve higher rigidity.

In the present work, we demonstrate the excellent performance of these new tags in *in-vitro*, cell lysate, and *in-cell* DEER measurements. The experiments showed a stable conjugation of the labels to the protein, a high binding constant of metal even under *in-cell* conditions, and high rigidity of the clamp resulting in narrow distances distributions which agrees with expected distances.

## 5.2 Materials and methods

1-(2-aminoethyl)-1H-pyrrole-2,5-dione, 1-(3-aminoethyl)-1H-pyrrole-2,5-dione, 1-(4-aminoethyl)-1H-pyrrole-2,5-dione and cyclen were purchased from Abosyn Chemical Inc. and CheMatech. Gd(OAc)<sub>3</sub>·4H<sub>2</sub>O, Yb(OAc)<sub>3</sub>·4H<sub>2</sub>O, N-(tert-butoxycarbonyloxy)succinimide and methyl 2-bromoacetate were purchased and used without further purification. Solvents were purchased from Honeywell, BIOSOLVE or Aldrich and directly used for synthesis. ATTO-647 maleimide was obtained from ATTO-TEC GmbH. Superdex 75 columns and Sephadex G-25 PD10 desalting columns were purchased from GE Healthcare. Reactions were followed by liquid chromatography-mass spectrometry (LC-MS), TLC analysis on silica gel (F 1500 LS 254 Schleicher and Schuell, Dassel, Germany) in which compounds were visualized by UV and/or ninhydrin, KMnO<sub>4</sub>. Flash chromatography was performed on Screening Devices silica gel 60 (0.04-0.063 mm). A Waters preparative RP-HPLC system, equipped with a Waters C18-Xbridge 5 µm OBD (30 x 150 mm) column and an Akta Basic FPLC (GE Healthcare Inc.) were used for purification. A LCQ liquid chromatography mass spectrometry system and a Finnigan LTQ Orbitrap system were used for high-resolution mass spectrometry and protein conjugation analysis. A Thermo Scientific™ NanoDrop 2000 spectrophotometer was used for protein concentration measurements.

### 5.2.1 Protein expression and purification

T4Lys mutant K147C/T151C was produced as described in previous work.<sup>176</sup> The tetra-cysteine mutant N55C/ V57C/K147C/T151C was generated by the Quikchange method (Agilent). After confirming the successful mutations by DNA sequencing, the gene was expressed in *Escherichia coli* BL21 (DE3). Transformed cells were incubated overnight at 37°C on LB agar plates with kanamycin and chloramphenicol (100 µl/mL and 34 µl/mL, respectively). Single colonies were transferred to 2 mL LB medium with kanamycin and chloramphenicol and incubated at 37°C, 250 rpm for 6 h. The precultures were used to inoculate 50 mL (1:1000) for overnight incubation in minimal medium (M9, 37°C, 250 rpm). The 50 mL culture was diluted 100 times and incubated at 37 °C, 250 rpm. When the OD<sub>600</sub> value reached 1, gene expression was induced by addition of 1 mM isopropyl β-D-thiogalactoside (IPTG). The temperature was reduced to 30 °C and the cells were harvested 18h after induction by centrifugation. The T4Lys N55C/V57C/K147C/T151C was purified according to the method described by Georgieva et al.<sup>177</sup> with some modifications. Cells were lysed using a French press and cleared by centrifugation (45 min, 2500 rpm). The supernatant was loaded on a 5 mL HiTrap CM column equilibrated with 25 mM Tris pH 7.5. The column was washed with 0-40% linear gradient of buffer B (25 mM Tris pH 7.5, 500 mM NaCl). T4Lys N55C/V57C/K147C/ T151C was eluted in one step with 100 % buffer B.

### 5.2.2 DEER sample preparation

The samples for in vitro and in lysate DEER measurements contained 100-150 µM of Gd(III)-CLaNP13 labeled N55C/V57C/K147C/ T151C T4Lys in 20 mM sodium phosphate, pH = 5.5, 150 mM NaCl, 20% (v/v) glycerol, *E. coli* cell lysate (20% (v/v) glycol) and *D. discoideum* cell lysate (20% (v/v) glycol). The sample for in-cell DEER measurement was obtained by incubating *D. discoideum* medium with the protein labelled with Gd(III)-CLaNP13b at a concentration of 115 µM for 90 mins. The cells were recovered, and washed three times in medium to remove excess protein, and to concentrate the cell suspension. The sample was cooled to approx. 4 °C on ice, and 10% (v/v) DMSO was added to the medium to prepare the cells for freezing and EPR measurement.

### 5.2.3 EPR measurements conditions

The 95 GHz DEER measurements were recorded using an ELEXSYS E680 spectrometer (Bruker, Rheinstetten, Germany) with a home-built probe head. The measurements were done at a temperature of 10 K. The DEER spectra were recorded using the standard four pulse DEER sequence<sup>178</sup>. The pump pulse duration was 40 ns and the observer pulses durations were 32 and 64 ns, respectively. The pump pulse power was adjusted to invert the echo maximally. The separation between the pump and observer frequencies ( $\Delta\nu$ ) was 60 MHz, with the pump pulse adjusted to irradiate at the maximum of the EPR spectrum. To make optimum use of the resonator bandwidth, the pump and observer frequencies were set to 30 MHz higher and lower frequencies respectively with respect to the resonance frequency of resonator. The full sequence for the observer was  $\pi/2$ - $\tau$ - $\pi$  - $\Delta t$ -  $\pi$  -echo with a delay time  $\tau$  of 360 ns and time steps for DEER evolution of 8 ns. The DEER data were analyzed with the program DeerAnalysis 2018.<sup>56</sup>

Since the modulation depth depends strongly on the precise setup of the experiment, e.g. choice of pump and observer frequency relative to the resonance frequency of the EPR resonator, this parameter can differ from experiment to experiment on the order of 25%. The *in-cell*/DEER experiment had been setup for a higher signal to noise ratio rather than for higher modulation depth due to instrumental issues. Also it must be noted that the experiment lasted less than 8 hours, instead in most cases in-cell measurements are taken for a longer period of time<sup>179-181</sup>.

## 5.3 Results

### 5.3.1 Design and synthesis of Gd(III)-CLaNP13.

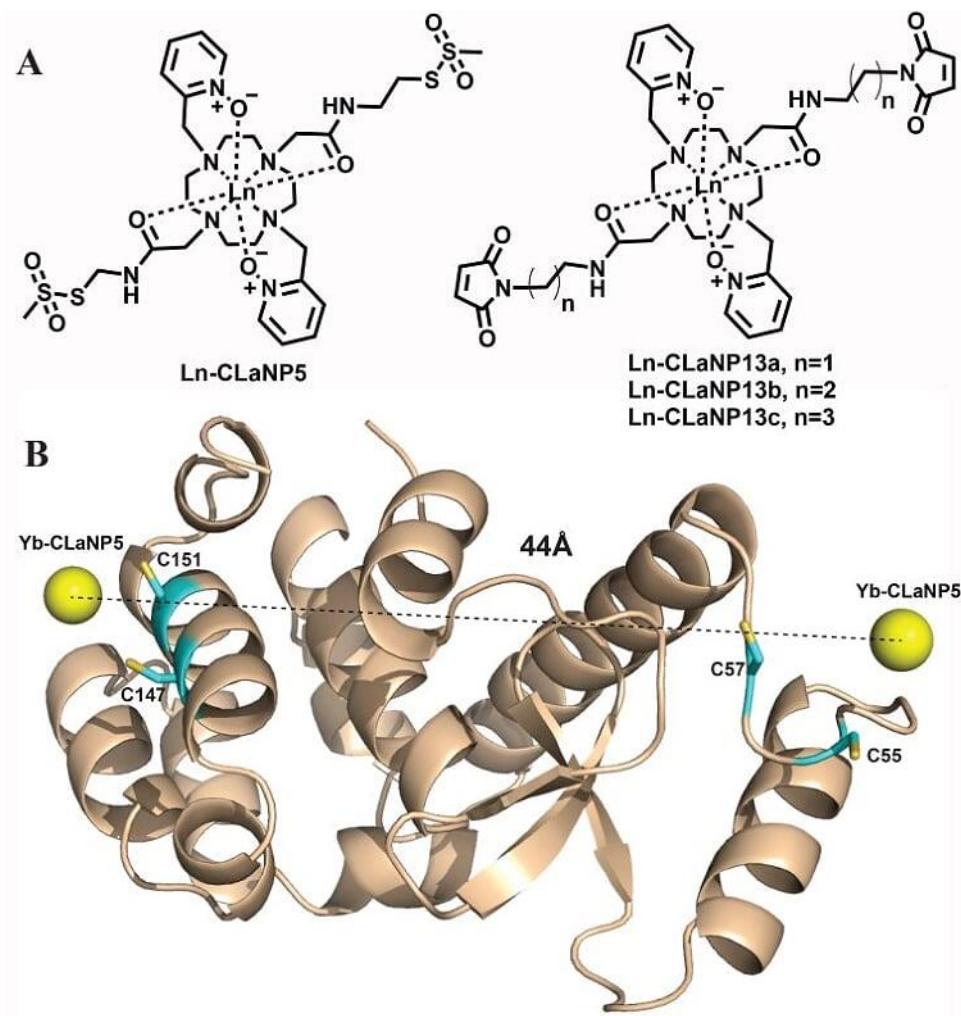


**Figure 5.1** Visual representation of the Gd(III) tags from the chemical point of view and in protein. A) Structures of Ln(III)-CLaNP5 and Ln(III)-CLaNP13; B) Model of the structure of T4Lys based on PDB entry 3dke<sup>182</sup> with two Cys pairs for the attachment of two probes. The positions of the metals are based on PCS analysis using Yb(III)-CLaNP5 as a paramagnetic probe. The backbone is drawn in ribbon representation. The Cys residues used for attachment have been modelled into the structure and are shown in sticks. The metal ions are shown as yellow spheres.

The caged lanthanoid NMR probe CLaNP5 is a well-studied two-armed Ln(III) probe for paramagnetic NMR spectroscopy on proteins. The cyclen based molecule is equipped with two pyridine N-oxide coordination arms that reduce the arm rotation (Figure 5.1). Using CLaNP5 as a building block, Gd-CLaNP13 was designed, in which the arms for protein attachment were functionalized with maleimide groups. The length of the spacer was varied from 2 to 4 methylene groups (Figure 5.1). Maleimide can readily and



specifically react with the thiolate group of a cysteine side chain, forming a carbon-sulfur bond, which is not prone to reduction.

### 5.3.2 Protein labeling

A  $^{15}\text{N}$  enriched variant of T4 lysozyme (T4Lys) with the substitutions K147C/T151C was used to determine optimal conditions for protein labeling on the basis of LC-MS and NMR results. The best result for double maleimide reactions with the cysteines was using a buffer with pH 7.8, at 4 °C for 6 h. To test whether free thiolates remained after the reaction, iodoacetamide was added. The LC-MS results, obtained by Dr. Bogdan Florea, yielded masses that match those expected for probes attached via two arms, assuming that one or two water molecules remained bound to the protein-probe complex. No peaks with additional mass of 58 Da were detected, which would be expected for protein with one-arm attached probe and an additional acetamide group linked to the second cysteine sulfur atom, and also no free protein was detected, suggesting that the protein labelling efficiency was more than 95%. In the MS spectrum of the CLaNP13a, a very small peak (20552 Da) is observed that represents T4Lys with two probes bound, each via a single arm (Figure S5.1). After attachment of the first maleimide group, the reaction with the second will generally be efficient because it is intramolecular. The limited length of the linker in CLaNP13a may allow for some competition with the second-order reaction of the protein-probe complex with a second probe molecule. However, according to the MS spectrum (Figure S5.2), the fraction of this species is not easy to detect.

### 5.3.3 Results of EPR experiments

For the EPR experiments, the quadruple cysteine mutant T4Lys N55C/V57C/K147C/T151C was labeled with Gd(III)-CLaNP13, variants a, b or c (Figure 5.1A), the resulting constructs are referenced to as Gd13iT4L with i:a,b,c. In the following we will describe the experimental results. We refer to investigations of the protein constructs in buffer as “in vitro”.

The echo detected EPR spectrum of the Gd13bT4L is shown as an inset in Figure 5.2 and in Figure S5.4. All three constructs have similar spectra. Specifically, they consist of a central narrow line due to the  $m_s = -\frac{1}{2} \leftrightarrow +\frac{1}{2}$  transition that is superimposed on a broad background due to all other transitions. The width of the central transitions for the different tags are shown in Table 5.1, and it can be noticed that Gd13bT4L has the narrowest central transition of the three.

## Chapter 5

**Table 5.1** Characteristics of EPR spectra of the Gd constructs used. Given is the full-width at half maximum (FWHM) from the central transition ( $m_s \pm 1/2$ ) in the field-swept electron-spin echo (FSESE) of the Gd-CLaNP13a,b,c labeled proteins.

Sample	MHz
Gd13aT4L	144.63 $\pm$ 1.91
Gd13bT4L	113.42 $\pm$ 4.41
Gd13cT4L	135.94 $\pm$ 2.42

### 5.3.4 Results of distance measurements

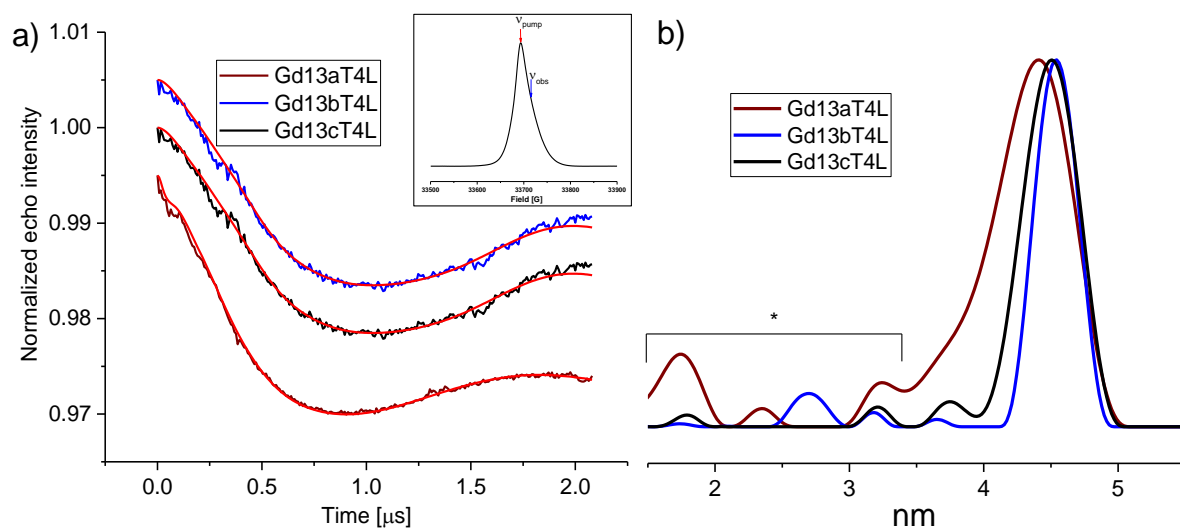


**Figure 5.2** DEER data of T4Lysozyme N55C/V57C/K147C/T151C labeled with Gd-CLaNP13a,b,c to form Gd13aT4L, Gd13bT4L, Gd13cT4L respectively. a) Background corrected DEER traces. Traces are shifted vertically for clarity. Measurements were performed at 10 K for 6 to 12 hours. Red lines: fits obtained with the distance distributions shown in b) obtained after Tikhonov regularization ( $\alpha = 1000$ ). Peaks marked with an asterisk do not contribute significantly to the data, as determined by the DeerAnalysis suppression tool<sup>66</sup>. Inset: 95 GHz field-swept electron-spin echo spectrum (FSESE) of the central transition region, position of the pump and observer frequencies are shown.

The DEER data of all three Gd13iT4L ( $i = a.b.c$ ) constructs are depicted in Figure 5.2. Figure 5.2a shows the data after background removal and Figure 5.2b the derived distance distributions. The raw DEER data are shown in Figure S5.5. The distances in all three constructs are close to 4.5 nm with Gd13aT4L having the shortest distance at 4.41 nm.

## Chapter 5

**Table 5.2** Distances between Gd-atoms in Gd13iT4L ( $i = a, b, c$ ). Given is the maximum of the distance distribution and the full-width at half maximum (FWHM) of the distance distribution obtained with Tikhonov regularization ( $\alpha = 1000$ ) of the Gd-CLaNP13a,b,c labeled proteins

Sample	Distance [nm]	Width [nm] <sup>a</sup>
Gd13aT4L	$4.41 \pm 0.03$	$0.67 \pm 0.20$
Gd13bT4L	$4.54 \pm 0.02$	$0.39 \pm 0.08$
Gd13cT4L	$4.51 \pm 0.02$	$0.50 \pm 0.11$

<sup>a</sup> The full-width at half maximum (FWHM)

The modulation depth, in the order of 2 %, is typical for 95 GHz DEER on Gd (III) samples: Usually depths between 2 % and 5 % are observed.<sup>167</sup>

The stability of the label in more complex environmental conditions was checked by incubating Gd13iT4L in *Escherichia coli* lysate for a total time of 24 hours. The DEER traces are similar and the distance distributions are identical within the noise to the in vitro samples (see Figure S5.6). No systematic decay of the modulation depth was observed over the period of 24 hours. Since the uncertainty in the modulation depth is in the order of 25%, we cannot exclude that a decay in that order occurs over time, even though we do not find systematic changes in modulation depth.

### 5.3.5 In-cell DEER

To investigate whether the label is stable in the cell, we measured DEER of Gd13bT4L in *Dictyostelium discoideum* (*D.discoideum*) cells. Fluorescence microscopy on an ATTO-647-maleimide tagged T4Lys K147C/T151C variant shows that the protein enters the cells, and that protein outside the cell was efficiently removed by washing with PBS. The bright fluorescent spots observed within the cell indicate that the protein is likely to be contained within vesicles such as endosomes. The DEER trace in Figure 5.3, therefore, results from Gd13bT4L incorporated into the cells. Cells thawed after the DEER experiments were shown to be viable by live-cell microscopy (see SI)

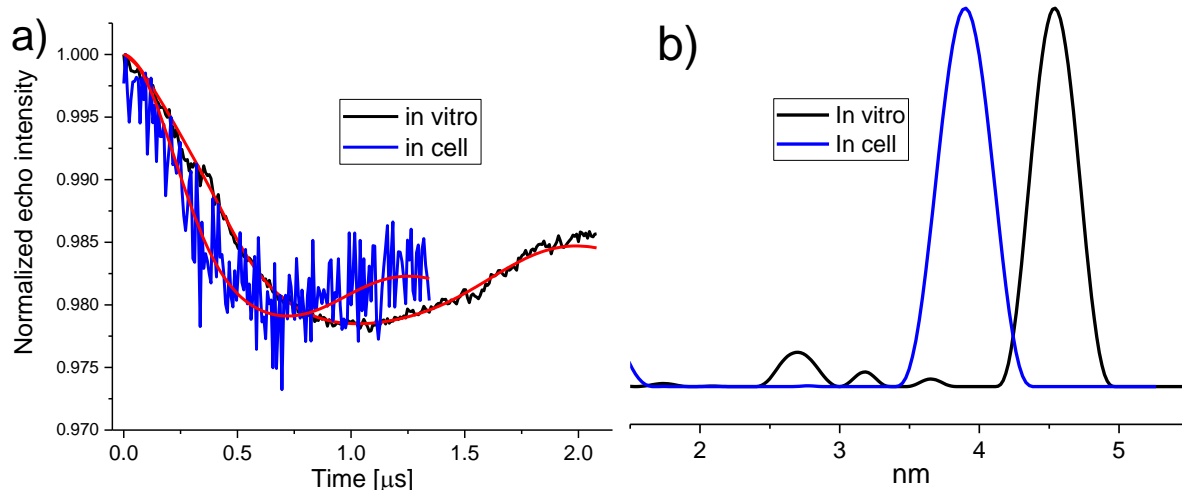


**Figure 5.3** Comparison of DEER traces of the protein *in vitro* and in *Dictyostelium discoideum* (Dicty) cells for the Gd-CLaNP13b tagged T4Lys N55C/V57C/ K147C/T151C *in vitro* (black) and in Dicty cells (blue). a) Background corrected DEER traces. Red lines: fits obtained with the distance-distributions calculation shown in b) obtained by Tikhonov regularization ( $\alpha = 1000$ )

The trace in Figure 5.3a has a clear DEER modulation, with a minimum at 0.6  $\mu\text{s}$ , which is also visible in the raw data (Figure S5.5d). Also, the width of the distribution is clearly in agreement with a fully intact doubly linked CLaNP. This proves that the Gd-CLaNP13 is stable in a cellular environment. The maximum of the distance distribution (Figure 5.3b) is at a shorter distance, 3.9 nm, than observed for Gd13bT4L *in vitro* and in *E. coli* cell lysates (see Figure S5.6). Further DEER experiments on Gd13bT4L in *D. discoideum* cell lysate and medium (for details, see SI) resulted in distance distributions that are dominated by a distance of 4.5 nm (see Figure S5.7). The possible origins of the shorter distance between the two Gd(III) ions in Gd13bT4L in *D. discoideum* cells compared to the one *in vitro* are discussed below.

## 5.4 Discussion

Here we report the synthesis of double-armed, rigid CLaNP tags linked by maleimide linkers to a protein to generate a Gd(III) spin label that is stable under in-cell conditions. Having two arms and a rigid CLaNP design should further improve the accuracy of DEER distance measurements. Three tags were obtained, Gd-CLaNP13a,b,c, which were synthesized in good yields and had high labelling efficiencies when attached to the protein T4L. All tags show clear DEER modulations with the expected modulation depth, confirming the reliable double labelling of the protein, inferred from mass spectrometry. Partial labelling by only one tag/protein would reduce the modulation depth, tags attached by only one arm should lead to broader DEER distance distributions and less pronounced modulation, neither of which is observed to any significant degree. The differences in distances for the three linkers are not monotonous with the linker length, suggesting that the linker takes on particular conformations, or that Gd(III) interactions with the protein surface could differ for the three linkers, leading to different distances. All distances (Table 5.2) agree well with the distance of 4.4 nm inferred from paramagnetic NMR data using the CLaNP-5 probes as mimics of CLaNP-13 (see Figure 5.1). Both the DEER time traces and distance distributions are similar for the three Gd13iT4L ( $i = a, b, c$ ) tags. (Figure 5.2). The width of the distance distribution, albeit small, is not exceptionally small considering the results of Gd(III) DEER experiments performed on proteins with singly linked probes.<sup>167,173,181,183</sup> Perhaps part of the width of the distribution observed in the present study is due to a distribution of conformations of the protein loop to which the Gd(III) at residues 55 and 57 is attached.

Having thus established that the constructs show the expected properties *in vitro*, we proceeded to study their resistance to cellular environments. In *E. coli* lysate, over a period of 24 h, no deterioration was detected within experimental limits, placing an upper limit of any possible decay at 25 % (see SI), a value that is largely determined by the experimental uncertainty. Prompted by the stability of the tags Gd13bT4L both *in vitro* and in *E. coli* lysate, in cell measurements were performed. *D. discoideum* was selected, because it is known for its high uptake of extracellular components.<sup>184</sup> The uptake was verified by fluorescence microscopy (see SI). The protein appears to be concentrated inside small vesicles, and there the estimated concentration is around 5  $\mu$ M. The cells were shown to be viable after DEER experiments (see SI). The DEER results of Gd13bT4L in cells are promising: The modulation depth of 1.5 % is smaller than observed *in vitro* and in *E. coli* lysate, but the difference is close to the error margins of the data (Figure 5.3a). We attribute the lower signal-to-noise ratio of the DEER trace of Gd13bT4L in the *D. discoideum* cells (Figure 5.3a) to the lower protein concentration and the 40 % shorter accumulation time compared to *in vitro* experiments. The distance distribution (Figure 5.3b) has a width that is similar to that of Gd13bT4L *in vitro*, showing that the

## Chapter 5

protein has a well-defined structure, and that the spin label remains bound. The maximum of the distance distribution for the in-cell DEER measurement is 3.90 nm, which is smaller than the 4.54 nm for the in vitro sample. So, while this initial experiment confirms that the probe is stable in cells, the difference in distance is puzzling. T4Lysozyme is known to undergo conformational changes, and by FRET experiments, distance changes in the order observed here, around 0.5 nm, were reported.<sup>185</sup> Also, a number of protein structures of T4L in different states are known. Nevertheless, we did not yet find any studies that match the distance of Gd13bT4L measured in *D.discoideum*. Initial experiments exposing Gd13bT4L to *D.discoideum* lysate and medium components did not pinpoint the origin of the distance change between in cell and in vitro. The protein is clearly not evenly distributed over the cytosol but rather is present in vesicles like endosomes, in which the local conditions, such as pH, could differ from those used in vitro. Although specific changes in structure of proteins in the cell have been reported before<sup>186</sup> and they are ultimately the motivation for in-cell work, for the present set of experiments it is too early to speculate on such an effect.

In conclusion, a new set of rigid Gd(III)-CLaNP has been synthesized that perform well in a cellular environment, showing that the Gd(III)-CLaNP13a,b,c are promising new candidates for in-cell Gd(III) work.

## 5.5 Supporting information

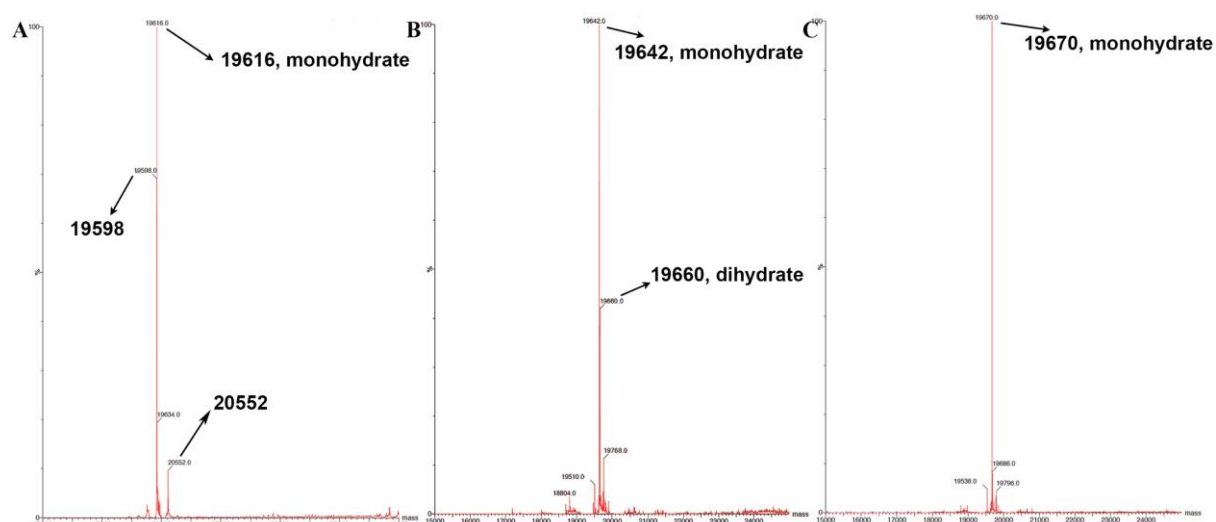


**Figure S5.1** ESI-TOF MS spectra of CLaNP13a (A), CLaNP13b (B) and CLaNP13c (C) linked to  $^{15}\text{N}$  enriched T4lys T147C/N151C mutant.

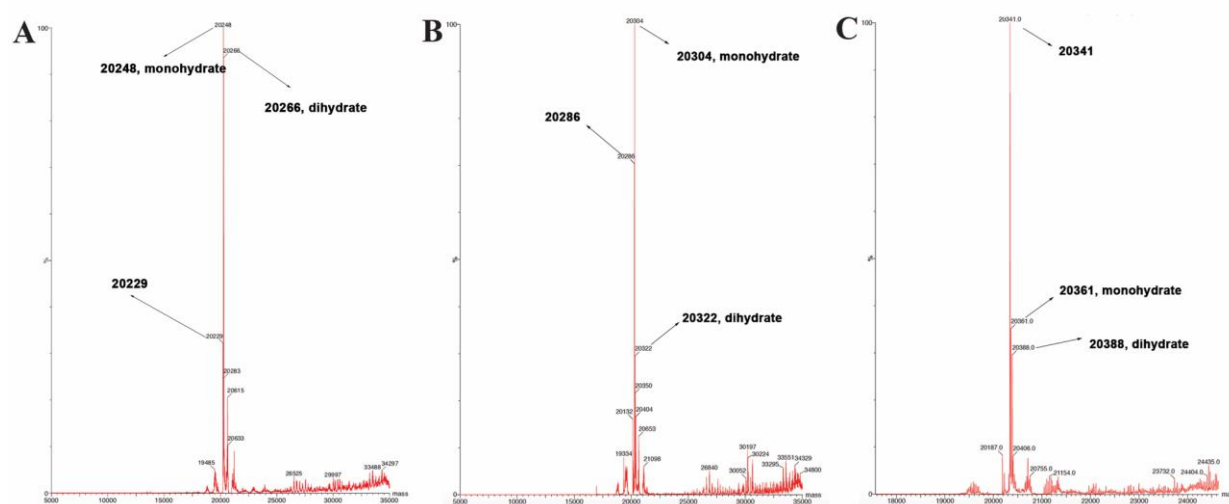


**Figure S5.2** ESI-TOF MS spectra of CLaNP13a (A), CLaNP13b (B) and CLaNP13c (C) linked to T4Lys N55C/V57C/T147C/N151C mutant.

### 5.5.1 Cell culture and live cell imaging

Axenic *D. discoideum* (AX2) was obtained from Dr. Günther Gerisch (MPI for Biochemistry, Martinsried, Germany). Cells were grown at 20 °C in HL5 medium and cultured in 100 mm Petridishes (TC-treated culture dish, Corning, USA) and confluency was kept below 70%. For microscopy experiments, cells were harvested and centrifuged at 1500 rpm for 3 min followed by three successive washing steps of the cellular pellet with 17 mM K-Na-phosphate buffered saline (PBS), adjusted to pH = 6.0. After resuspension in PBS, the cells were pipetted into a 70  $\mu$ L well inside a 35 mm imaging dish (Insert and dish, Ibidi GmbH, Martinsried, Germany) and left to adhere for 30 min. While imaging, T4Lys K147C/T151C linked to ATTO-647 (ATTO-TEC GmbH) was added to a final concentration of 100  $\mu$ M. Cells were left to incubate for 60 min and were imaged every 30 seconds in two channels (BF and 647) with a Nikon Eclipse Ti microscope, equipped with a Yokogawa confocal spinning disk unit operated at 10,000 rpm (Nikon, Tokyo, Japan). ATTO-647 was excited by a 647 nm solid state diode laser (Coherent, Santa Clara, U.S.A.), supported in an Agilent MLC4 unit (Agilent Technologies, Santa Clara, U.S.A.). Images were captured (50 ms) by an Andor iXon Ultra 897 High Speed EM-CCD (Andor Technology, Belfast, Northern Ireland) through a Cy5 HYQ filter (Nikon, Tokyo, Japan). After incubation, the well was carefully washed with PBS five times (50  $\mu$ L each step) and imaged for another 15 min.

### 5.5.2 Quantification of the in-cell T4-ATTO-647 concentration

Known concentrations of T4Lys K147C/T151C linked to ATTO-647 in PBS were imaged in the same condition as described for cells. The data were averaged over all images and pixels to find mean intensities per concentration. For the cell data, all pixels belonging to each cell were determined using an in-house Matlab (The Mathworks, Inc., Natick, MA, U.S.A.) script for cell edge recognition. In-cell pixels were averaged and subsequently compared to the concentration calibration measurements (see Figure S5.3) for two laser powers. All images were pre-processed by flat-field correction and dark-field subtraction.

LC-MS results showed that T4Lys K147C/T151C was tagged with only a single ATTO-647-maleimide per protein molecule. *D. discoideum* is known for its high uptake of extracellular components<sup>184,187</sup>. After 30 min incubation, almost all cells have taken up fluorescent protein and it was present in cell body in vesicles (Figure S5.3). The protein was washed away from the medium after 60 min, but the fluorescent protein can still be detected inside the cells and the concentration was estimated to be 5  $\mu$ M. The protein can still be detected in 3 h after the start of the incubation (Figure S5.3).

Similar experiments were conducted with double CLaNP13b tagged T4Lys for in-cell DEER experiments. After incubation, the cells were washed, concentrated and cooled on



ice. Before the cells were frozen for EPR measurement, 10% (v/v) DMSO was added to the medium. DEER experiments were performed at 10 K for 48 h.

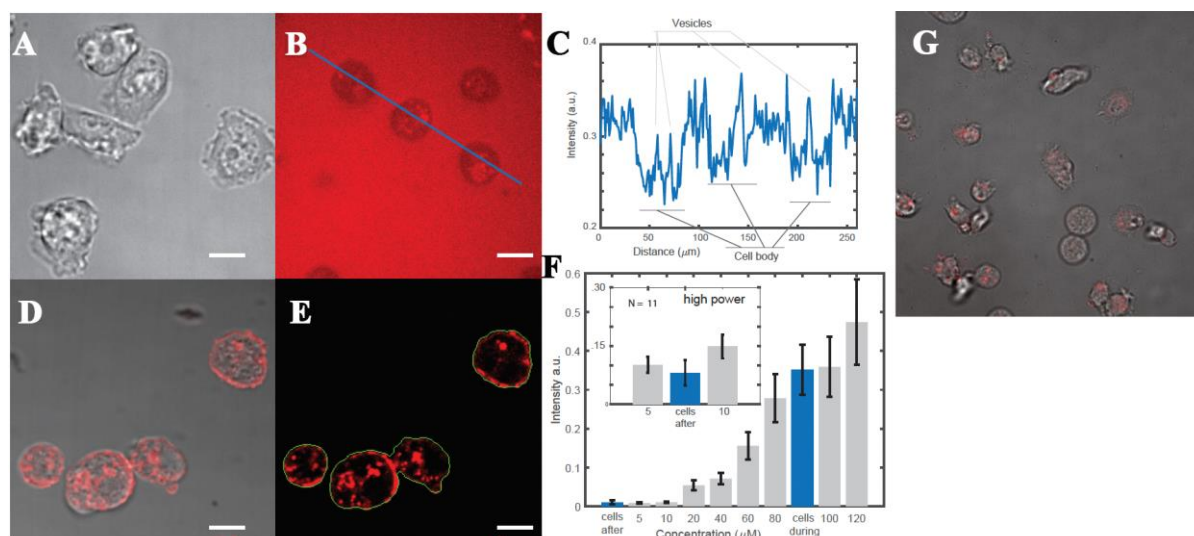


**Figure S5.3** Different stages of the internalization process of T4-ATTO-647 in vegetative *D. discoideum*. **A)** Just prior ( $t = 0$  min) to incubation, cells are adhered to the substrate; **B)** Incubation and subsequent internalization results in a shock response and cell rounding. Confocal fluorescence image (red) shows cells after  $t = 30$  min of incubation. Blue line marks the direction of intensity profile plot; **C)** Intensity profile of three cells during incubation, the protein is ubiquitous in cell body and surrounding medium; **D)** After washing with PBS ( $t = 60$  min) the cells recover and start spreading. T4-ATTO-647 remains in the cell after washing with phosphate buffered saline ( $t = 75$  min); **E)** To determine the protein concentration inside cells after incubation, cell edges are recognized (green) and mean fluorescence (red) intensities measured; **F)** Mean intensity histogram of various concentrations of T4-ATTO-647 in PBS (grey) versus mean fluorescence inside cells (blue) during and after incubation, measurements were repeated with higher power (inset); **G)** State of the cells after 3 hours of incubation

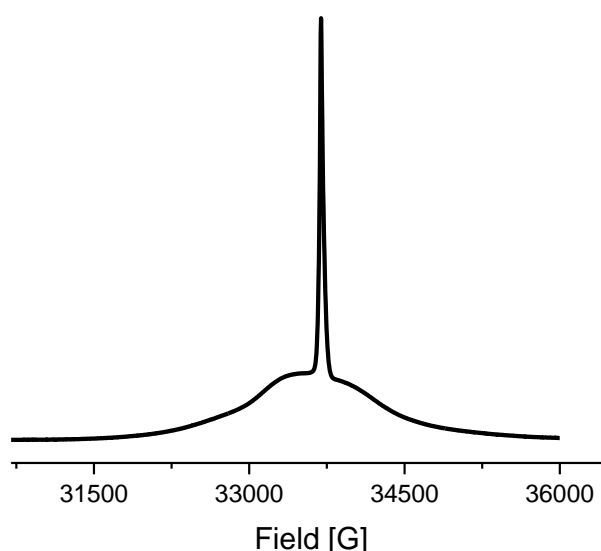


**Figure S5.4** EPR of samples in vitro. Shown is a Field-Swept Electron-Spin Echo (FSESE) spectrum at 95 GHz obtained at 10 K of Gd-CLaNP13b tagged T4Lys N55C/V57C/ K147C/T151C (200 μM). The measurement was carried out by a 2-pulse  $\{\pi/2-\tau-\pi-\tau\}$ -echo sequence with  $t(\pi/2) = 32$  ns,  $t(\pi) = 64$  ns. and  $\tau = 360$  ns.

## Chapter 5

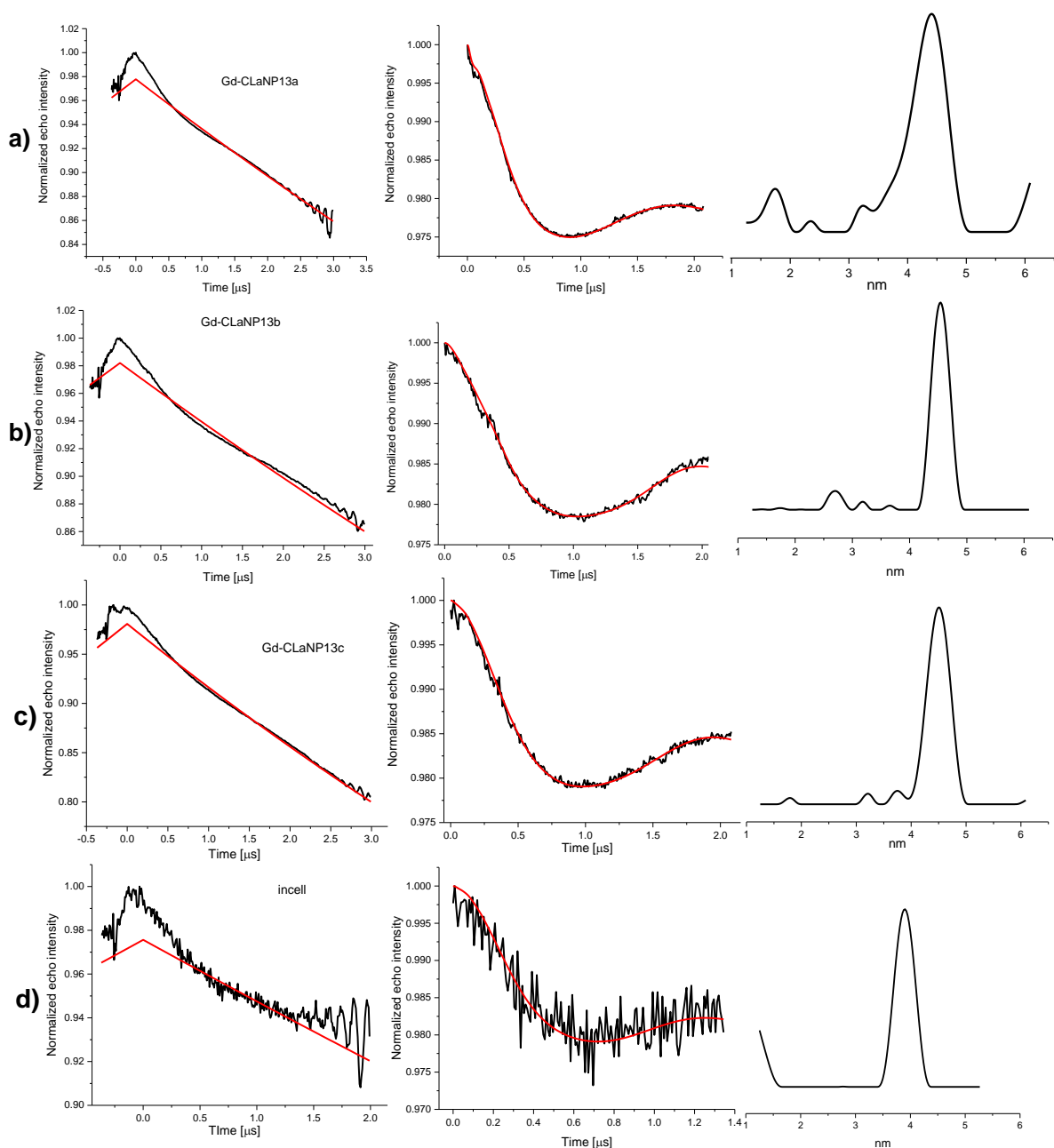


**Figure S5.5** Four-pulse DEER results obtained for Gd13iT4L (with  $i = a, b, c$ ) at 10 K. On the left: Normalized DEER traces fitted with appropriate background decay (in red). Middle: Same DEER traces after background removal along with the fits obtained by Tikhonov regularization (red). On the right: Distance distribution obtained by Tikhonov regularization ( $\alpha = 1000$ ) in DEER Analysis 2018. a) In vitro Gd13aT4L; b) In vitro Gd13bT4L; c) In vitro Gd13cT4L; d) In-cell Gd13bT4L.

## Chapter 5

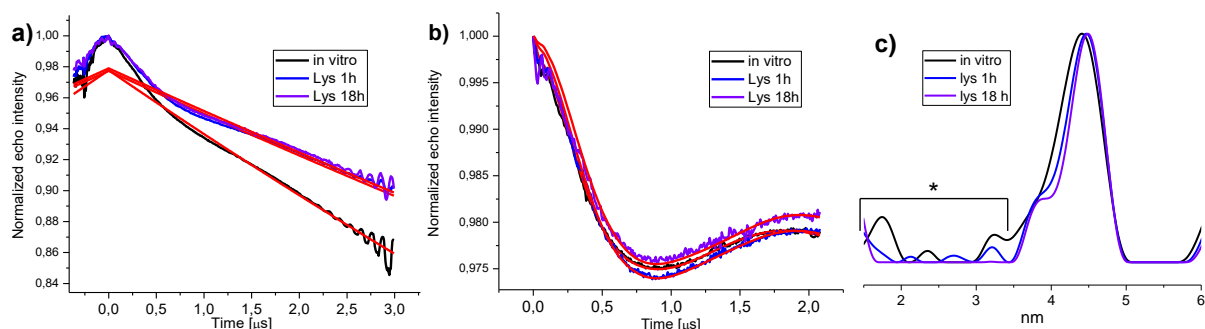


**Figure S5.6.** Four-pulse DEER traces and distance distributions for the Gd-CLaNP13a tagged T4Lys N55C/V57C/K147C/T151C samples in vitro (black), incubated in *E. coli* lysate for 1 hour (blue) and for 18 hours (violet). Measurements were done at 10 K. a) Normalized DEER traces fitted with appropriate background decay (red); b) Background corrected DEER traces. Red lines, fits obtained with the distance-distribution calculations shown in (c) obtained after Tikhonov regularization ( $\alpha = 1000$ ) in DEER Analysis 2018.<sup>56</sup> Peaks marked with an asterisk do not contribute significantly to the data.

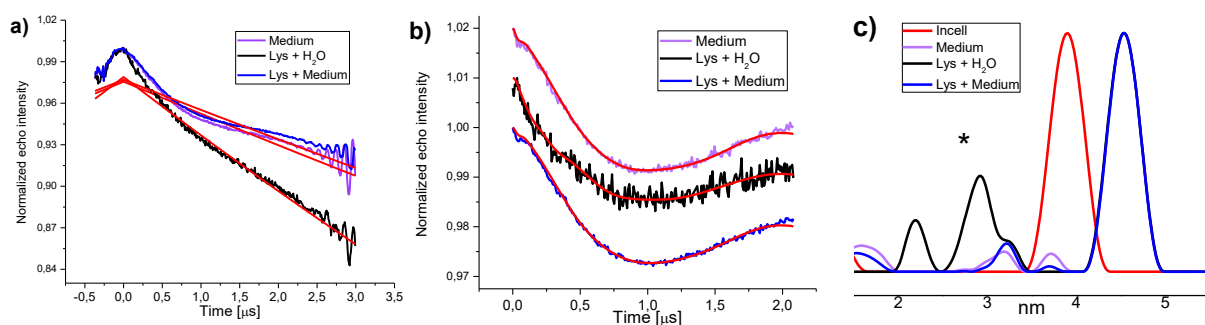


**Figure S5.7.** Four pulse DEER traces and distance distributions for the Gd-CLaNP13b tagged T4Lys N55C/V57C/K147C/T151C samples in *D. discoideum* cell lysate + milliQ H<sub>2</sub>O (black), in medium (violet), in lysate + medium (blue). Measurements were done at 10 K. a) Normalized DEER traces fitted with appropriate background decay (red). b) The corresponding four pulse DEER traces along with the fits obtained by Tikhonov regularization (red). Traces are shifted vertically for clarity. c) Distance distributions obtained by Tikhonov regularization ( $\alpha = 1000$ ) in DEER Analysis 2018.<sup>56</sup> The distance distribution of the in-cell Gd13bT4L (red) has been added to better show the differences. Peaks marked with the asterisk do not contribute significantly to the data.



## **6 Synthesis and characterization by EPR of backbone-labeled Amyloid $\beta$ peptides and influence of an antiamyloidogenic cyclic D,L- $\alpha$ -peptide as potential inhibitor for their aggregation**

The Amyloid  $\beta$  peptide ( $A\beta$ ) is involved in Alzheimer's disease, the most common neurodegenerative disease. This chapter reports the synthesis of two TOAC, 2,2,6,6-tetramethyl-N-oxyl-4-amino-4-carboxylic acid, labeled  $A\beta$  peptides, T0 $A\beta$  with the spin label at the N-terminus, and T26 $A\beta$  with the spin label at position 26 in the sequence. The TOAC spin label incorporates directly into the backbone of peptides, an advantage to determine the aggregation of the peptide. To monitor the aggregation, the rotational correlation time ( $\tau_r$ ) is measured by 9 and 95 GHz EPR. Both constructs aggregate, however, T26 $A\beta$  significantly less than T0 $A\beta$ . We show that the antiamyloidogenic cyclic D,L- $\alpha$ -peptide CP-2<sup>188,189</sup> interacts with T0 $A\beta$  and T26 $A\beta$ , possibly as a multimer. Above a ratio of 5 : 1 of CP2 to  $A\beta$ , CP2 blocks the formation of fibrils.

## 6.1 Introduction

Alzheimer's disease is a neurodegenerative disease affecting an increasing amount of the aging population<sup>190</sup>. There is currently no cure, making the search for mechanisms of the disease urgent and timely. The aggregation of the amyloid  $\beta$  peptide, that derives from the misprocessing of the amyloid precursor protein (APP) is one of the central features of the disease<sup>191–196</sup>. As also the physical-chemical mechanisms of amyloid aggregation are poorly understood, research techniques to investigate the physical-chemical mechanisms of amyloid aggregation are necessary.

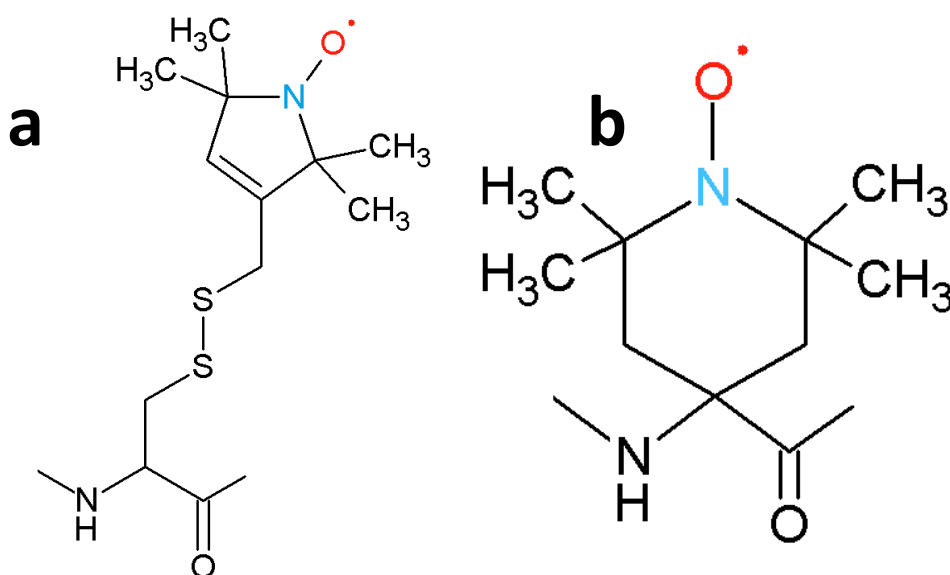


**Figure 6.1** a) Molecular structure of the MTSL spin label attached to a cysteine side-chain. b) Molecular structure of the TOAC spin label.

Here we want to make use of Electron Paramagnetic Resonance (EPR) to study amyloid aggregation. Specifically, we will employ the sensitivity of continuous wave EPR to the rotational mobility of an object, which is related to its size and thereby can measure the size-increase of the aggregating peptides<sup>45–47,57,197</sup>. The rotational correlation time can be measured, if the object contains a nitroxide spin label. In the context of the present study this means that the amyloid peptide has to be labeled with a nitroxide spin label, see Figure 6.1.

Usually spin labels, such as the *S*-(1-oxyl-2,2,5,5-tetramethyl-2,5-dihydro-1H-pyrrol-3-yl)methyl methanesulfonothioate (MTSL) are used. Such labels are coupled to a cysteine in the protein, a cysteine that is introduced by site-directed spin labeling<sup>45,57</sup>. The disadvantage of this approach is the local mobility of such spin labels, caused by the rotational freedom about the single bonds connecting the nitroxide to the cysteine residue, and thereby the backbone of the protein, see Figure 6.1a. As EPR probes the mobility of the N-O group of the nitroxide, this decoupling, local mobility, limits the access

## Chapter 6

to mobility information on the particle, i.e. the aggregates that the peptide forms. We therefore resorted to the 2,2,6,6-tetra-methylpiperidine-1-oxyl-4-amino-4-carboxylic acid (TOAC) spin label. In TOAC, the nitroxide is directly coupled to the peptide backbone, see Figure 6.1b, thus avoiding the problem of local mobility.

To investigate the aggregation of amyloid peptides using this approach, we synthesized the peptides shown in Table 6.1 by SPPS (Solid Phase Peptide Synthesis). The peptides are based on the 40-amino acid long APP fragment A $\beta$ -40. They contain the TOAC spin label in two strategically chosen positions: At the N-terminus (T0A $\beta$ ) and at position 26 (T26A $\beta$ ), replacing the Asn in the A $\beta$ WT sequence. These constructs enable us to monitor the end (T0A $\beta$ ) and the central part (T26A $\beta$ ) of the peptide.

We investigate these peptides by continuous wave EPR in liquid solution. To maximize the sensitivity and resolution, standard 9 GHz EPR is combined with high-field, 95 GHz EPR. The lineshape of the EPR spectra obtained is sensitive to the nitroxide motion in the time regime of 0.1 ns to 10 ns and thereby is relevant to the aggregation process as described below.

In the present study we investigate if and how TOAC influences the aggregation of A $\beta$ , as a first characterization of the synthesized constructs. As a first application, we study the interaction of T0A $\beta$  and T26A $\beta$  with a cyclic D,L- $\alpha$ -peptide (CP-2) (Table 6.1), a recently discovered inhibitor of A $\beta$  aggregation, considered as a possible drug candidate<sup>188,189</sup>.

We find that T0A $\beta$  aggregates significantly faster and with higher yields than T26A $\beta$ . We show that the interaction of A $\beta$  with CP-2 can be detected and that multiple CP-2 peptides must be involved in the interaction.

**Table 6.1** Sequences of peptides. The spin label TOAC (2,2,6,6-tetra-methylpiperidine-1-oxyl-4-amino-4-carboxylic acid) is abbreviated as T.

<i>Sequence<sup>a</sup></i>	
<b>A<math>\beta</math>-40 WT</b>	DAEFRHDSGYEVHHQKLVFFAEDVGSNKGAIIGLMVGGVV
<b>T0A<math>\beta</math>-40</b>	T-DAEFRHDSGYEVHHQKLVFFAEDVGSNKGAIIGLMVGGVV
<b>T26A<math>\beta</math>-40</b>	DAEFRHDSGYEVHHQKLVFFAEDVGS-T-KGAIIGLMVGGVV
<b>CP-2</b>	[I-J-w-H-s-K]

<sup>a</sup> Capital and lower case letters represent L- and D-amino acid residues, respectively. Square brackets indicate a cyclic structure.

## 6.2 Materials and methods

### 6.2.1 Synthesis and Characterization of Peptides

All chemicals were commercial products of the best quality available and, unless otherwise indicated, they were used without any further purification. The Abeta40 WT and Abeta42 WT peptide were purchased from tebu-bio (Heerhugowaard, The Netherlands).

9-Fluorenylmethoxycarbonyl(Fmoc)-amino acids, Fmoc-Val-Wang Tentagel resin and the other chemicals used for the solid phase peptide synthesis were purchased from Sigma Aldrich. 2,2,6,6-Tetramethylpiperidine-N-oxyl-4-(9-fluorenylmethoxycarbonylamino)-4-carboxylic acid (Fmoc-TOAC-OH) and H-Val-Wang resin were supplied by Iris Biotech (Marktredwitz, Germany).

The peptide sequences were assembled on AB433A Peptide Synthesizer (Applied Biosystems, Foster City, CA, USA), using 0.05 mmol of Gly-Wang resin (substitution 0.24 mmol/g). For all amino acids except TOAC we use 10 equivalents (0.5 mmol) of each AA for the synthesis. Deprotection by Fmoc was done 3 times (2 minutes each) by adding 2.5 mL of a solution of 20 % piperidine (PIP) in N-methylpyrrolidone (NMP). Couplings were performed using 1-[Bis(dimethylamino)methylene]-1H-1,2,3-triazolo[4,5-b]pyridinium 3-oxid hexafluorophosphate (HATU) as an activator and N-Methylmorpholine (NMM) as base. We used 1 equivalent of HATU and 2 equivalents of NMM for 1 equivalent of AA. 2 mL of a solution of HATU (0.225 M in NMP), 0.5 mL of a solution of NMM (1 M in NMP) and 1 mL of NMP:DMSO (1:1) were added to the resin for the coupling reactions. Each coupling reaction lasted 2 hrs.

The TOAC spin label was treated differently. Only 2 equivalents of AA were added for 1 equivalent of resin. HATU was used as activator and 400  $\mu$ L of its solution (0.5 M in NMP) were put directly inside the cartridge with the spin label together with 600  $\mu$ L of NMP. The coupling in this case lasted 4 hrs. For the AA introduced immediately after the TOAC we used a double coupling, keeping the same conditions as for the rest of the sequence. The Fmoc absorption at 301 nm was followed to check the status of the synthesis after each coupling step.

At the end of the synthesis the resin was dried by washing it with dichloromethane (DCM). To cleave the peptide from the resin 2 mL of a solution 95% trifluoroacetic acid (TFA) + 5% water was used. A small amount of peptide was cleaved from the resin and characterized by LC-MS. Unless otherwise indicated, the peptides were purified by semi-preparative HPLC.

Analytical HPLC separation was carried out on a LCQ Advantag Thermo Finnigan LC-MS system with UV-Vis and Ion-trap mass detectors. The column used was a C-18 Gemini (4.6 x 50 mm, 3  $\mu$ m particle size) from Phenomenex (Torrance, California). The mobile phase A (H<sub>2</sub>O), B (acetonitrile, MeCN) and C (aqueous 1 % TFA) was used for preparing ternary



## Chapter 6

gradients. Elution condition: A 80 % B 10 % C 10-90 %, linear gradient B 18-33 % in 10 min. Flow rate 1 mL/min.

Crude peptide purifications were performed on a Gilson HPLC preparative system with a semipreparative Gemini C<sub>18</sub> column (10 x 250 mm) from Phenomenex with UV-Vis detector. The mobile phase A (aqueous 1 % trifluoroacetic acid, TFA) and B (acetonitrile, MeCN) were used for preparing binary gradients. Elution condition: A 82 % B 18 %, linear gradient B 18-33 % in 10 min, Flow rate 5 mL/min.

The lyophilization was done on a Christ Alpha 2-4 LO lyophilizer (Salm&Kipp, Breukelen, Netherlands) with a Christ RVC 2-25 rotor. All TOAC peptides had a high level of purity as shown by single band elution and mass spectrometry.

T0AB40: yield 11.996%; LC-MS (C<sub>18</sub>)  $t_R$  7.06 min; purity > 95%; Mass: calculated for C<sub>61</sub>H<sub>108</sub>N<sub>15</sub>O<sub>18</sub> [M+H]<sup>+</sup> 4529.14, found: 4529.40

T26AB40: yield 3.152%; LC-MS (C<sub>18</sub>)  $t_R$  7.27 min; purity > 95%; Mass: calculated for C<sub>69</sub>H<sub>122</sub>N<sub>17</sub>O<sub>20</sub> [M+H]<sup>+</sup> 4440.06, found: 4440.00

### ***6.2.2 Protocol for the aggregation experiments***

Samples were prepared as follows: The powder of the lyophilized spin-labelled A $\beta$  peptides was treated with a solution of 30 % NH<sub>3</sub> in H<sub>2</sub>O for 3 hours at RT to restore the nitroxide radical. The solution was then lyophilized once again. The resulting powder was dissolved in DMSO to obtain stock solutions of concentration 3 mM. Of these stock solutions, 33  $\mu$ L were pipetted into 1.5 mL Eppendorf tubes. To ensure the monomeric state of the peptide, we added 100  $\mu$ L of NaOH 10 mM to the Eppendorf tubes<sup>198</sup>. After 2 minutes of sonication in an ice bath, chilled 100  $\mu$ L of PBS 100 mM buffer containing 25  $\mu$ M ThioT was added. To neutralize the base we added 100  $\mu$ L of HCl 10 mM to obtain a final pH of 7.4. At this point, milliQ water and DMSO were added to obtain a final volume of 500  $\mu$ L. The final concentrations are A $\beta$  200  $\mu$ M, PBS buffer 20 mM, ThioT 5  $\mu$ M with a final concentration of DMSO of 10 %. Samples containing the inhibitor CP-2 were prepared following the same protocol. The stock solution of CP-2 was prepared by dissolving the lyophilized powder in DMSO to a final concentration of 39 mM. Of this stock solution, the appropriate amounts of CP-2 were added to the A $\beta$  solution to obtain the desired ratio of peptide and inhibitor. If required, DMSO was added to obtain a final 10 % DMSO concentration in all samples. Aggregation experiments were carried out during one week, unless noted otherwise.

### 6.2.3 ThioflavinT fluorescence plate reader experiments

The samples were monitored by the standard Thioflavin T (ThioT) fluorescence assay<sup>107</sup>. The Eppendorfs were put for 2 minutes of sonication in ice bath, then samples were pipetted into a 96 wells plate, holding 200  $\mu$ L each. Each sample was measured in duplicates. Fluorescence measurements were recorded with an CLARIOStar Plus (BMG LABTECH GmbH, Allmendgrün 8, 77799 Ortenberg, Germany) microplate reader every 10 min for a week, using excitation and emission wavelengths of  $444 \pm 10$  and  $485 \pm 10$  nm, respectively. The plate was held at +37 °C, and the wells were automatically shaken 30 seconds before each measurement step. The fluorescence increase was measured with respect to the ThioT blank without the peptide.

### 6.2.4 EPR measurement conditions

The remaining sample solutions in the Eppendorf tubes were kept on ice to be measured by EPR. After an initial measurement taken at the time the sample was prepared ( $t = 0$ ), the remaining samples of 80  $\mu$ L in 1.5 mL Eppendorf tubes were aggregated on a thermomixer (Eppendorf, Thermomixer comfort, Waltham, MA USA) at 310 K. The EPR of the aggregated sample was measured after one week to observe the aggregation.

The 9 GHz, continuous-wave EPR spectra were recorded using an ELEXSYS E680 spectrometer (Bruker, Rheinstetten, Germany). The measurements were done under the following conditions: room temperature (293 K), a microwave power of 0.63 mW and a modulation amplitude of 0.2 mT at a modulation frequency of 100 kHz. The time expended on each measurement was adapted according to the spectral lineshape. Glass micropipettes of a volume of 50  $\mu$ L (Blaubrand Intramark, Wertheim, Germany) were filled with 20  $\mu$ L of the sample for each measurement. The spin concentration was determined by comparing the double integral of the EPR spectra with the double integral of a reference sample (MTSL, 100  $\mu$ M). The spin concentrations determined from the double integrals were 60  $\mu$ M for T26A $\beta$  and 80  $\mu$ M for T0A $\beta$  to an expected 200  $\mu$ M, giving an activity of  $\approx 30\%$  and  $\approx 40\%$  respectively.

The 95 GHz EPR spectra were recorded at room temperature on a Bruker ELEXSYS E680 spectrometer using a home-built probehead with a single-mode cavity specially designed for cw measurements. Acquisition parameters: microwave frequency 94.04 GHz, microwave power 0.63  $\mu$ W, modulation amplitude 1 mT, modulation frequency 6 kHz. Total measurement time: approximately 5 hours.

### 6.2.5 Simulations of EPR spectra

MATLAB (version 9.4.0.813654, R2018a, The MathWorks, Inc., Natick, MA, USA) and the EasySpin package (5.2.25) were used for simulations of the EPR spectra.<sup>48</sup> The parameters of the simulation were manually adjusted to agree best with the experimental spectra. For all simulations, an isotropic rotation of the nitroxide ( $S = 1/2$ ) was utilized. The following g-tensor values were used:  $g = [2.0086 \ 2.0059 \ 2.0020]$ . These values were obtained from M. Hashemi Shabestari et al.<sup>108</sup>, and we used these values for all other simulations. The spectra were simulated with a superposition of three components: a fast and medium fractions using the “Chili” function and a slow fraction using the “Pepper” function. For T0A $\beta$  the principal values of the  $^{14}\text{N}$  hyperfine coupling tensor were  $A_{xx} = A_{yy} = 13$  MHz and  $A_{zz} = 112.7$  MHz for the fast component,  $A_{xx} = A_{yy} = 13$  MHz and  $A_{zz} = 107.5$  MHz for the medium component, and  $A_{xx} = A_{yy} = 13$  MHz and  $A_{zz} = 95$  MHz for the slow component.<sup>108</sup> For T26A $\beta$  the values were  $A_{xx} = A_{yy} = 13$  MHz and  $A_{zz} = 110.7$  MHz for the fast component, and  $A_{xx} = A_{yy} = 13$  MHz and  $A_{zz} = 95$  MHz for the slow component. For the 9 GHz spectra, a Gaussian component with a linewidth of 0.1 mT was used for the fast component and medium components, and 0.65 mT for the slow component. For the 95 GHz spectra of T26A $\beta$ , a Gaussian line with a width of 0.12 mT was used for the fast component and of 0.15 mT for the slow component was applied. The  $\tau_r$  of the fast component was chosen by simulating the narrow lines of the time 0 samples without CP2. Optimal  $\tau_r$  values of the medium and slow components were derived from later time-point spectra and then kept constant for all simulations, with and without CP-2.

## 6.3 Results

The two A $\beta$  variants, T0A $\beta$  and T26A $\beta$  (sequences given in Table 6.1) were obtained in good yield and high purity (see Material and Methods). Reactivation of the nitroxide radical resulted in the  $40 \pm 5$  % active nitroxide for T0A $\beta$  and  $30 \pm 15$  % for T26 $\beta$ . Here we report the first characterization of the aggregation behavior for both peptide variants.

To detect fibrilization, ThioT fluorescence was used. For T0A $\beta$  ThioT fluorescence shows a plateau phase after 24 hours of aggregation, showing the formation of fibrils<sup>199</sup>. For T26A $\beta$  the ThioT signal increases as well, but the fluorescence of the plateau is approximately 10 % of that of T0A $\beta$  at comparable concentrations (see Figure S6.3). The ThioT results show that after a few days, aggregation is complete. Therefore, the EPR experiments, described in the following, were performed immediately after dissolving the peptide in buffer, referred to as “before aggregation” and after 7 days of aggregation referred to as “aggregated sample”.

Figure 6.2 shows the 9 GHz EPR spectra of T0A $\beta$  and T26A $\beta$  before and after aggregation. The spectra have the three-line pattern typical of nitroxide spin labels. The spectra (black) of T0A $\beta$  and T26A $\beta$  before aggregation differ from each other. The lines of T26A $\beta$

are broader than those of T0A $\beta$ , which shows a lower mobility at the center of the peptide compared to the N-terminus.

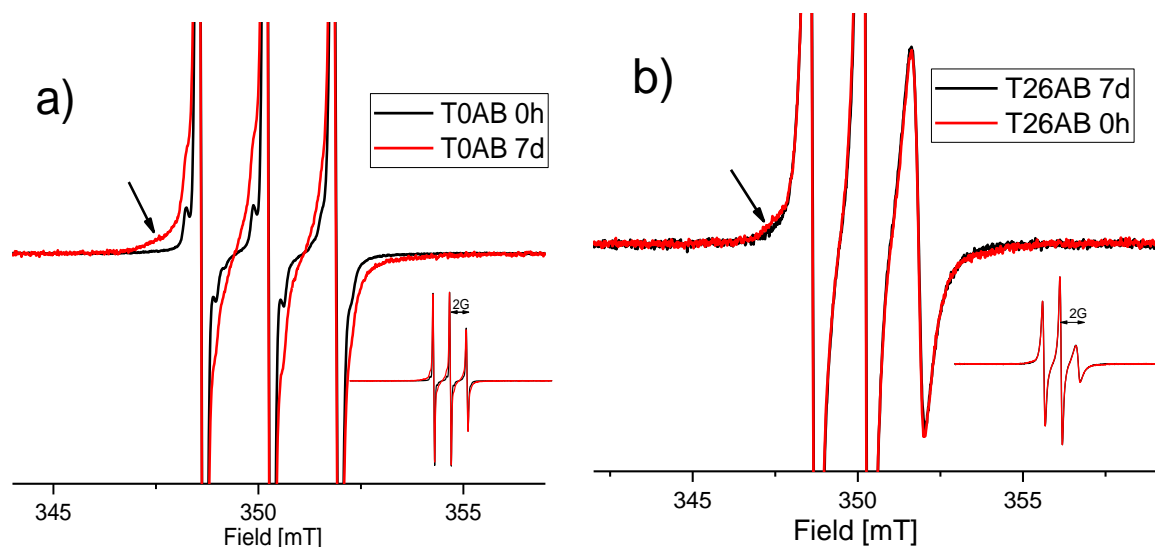


**Figure 6.2** Comparison of EPR spectra of TOAC A $\beta$  constructs before and after aggregation. Full spectra: inset. Zoomed-in spectra: Amplitude expanded four-fold. a) Spectra of T0A $\beta$  at start of aggregation (black) and after 7 days (red). b) Spectra of T26A $\beta$  at start of aggregation (black) and after 7 days (red).

After aggregation (conditions see Material and Methods), the T0A $\beta$  spectrum (Figure 6.2a, red) shows of an additional broad component, marked by the arrow, representing a component with lower mobility. The T26A $\beta$  spectrum after aggregation (Figure 6.2b, red) closely resembles the one at time 0, with much smaller deviations from the initial spectrum than observed for T0A $\beta$ .

By spectral simulation more details are obtained: All spectra can be simulated with maximally three components, a fast, a medium and a slow component. Figure 6.3 shows the shape of the components and their agreement with the experimental spectra. In Figure 6.3a and b the components by 9 GHz EPR are shown. For T26A $\beta$  we confirmed these components by 95 GHz EPR (Figure 6.3c).

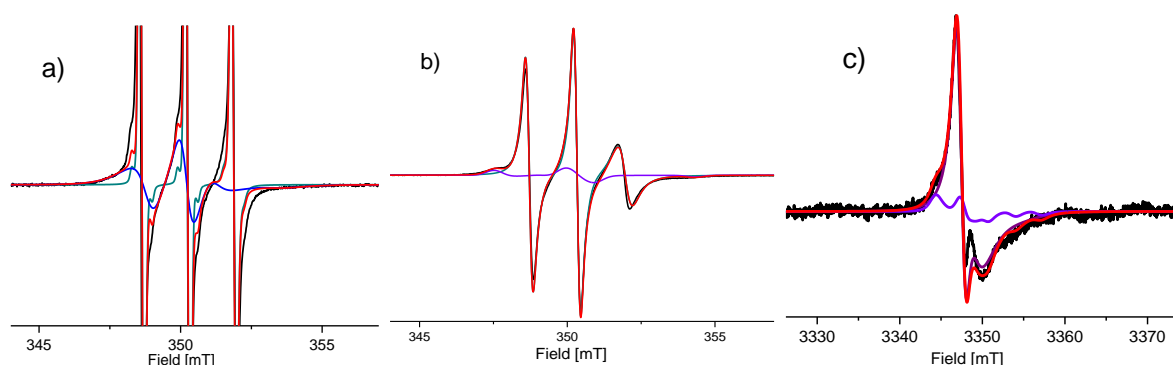


**Figure 6.3** Spectral components used in the simulation of the 9 GHz EPR spectrum of T0A $\beta$  (amplitude zoomed-in four-fold, 7 days aggregation) and T26A $\beta$  (10 days aggregation), and 95 GHz for T26A $\beta$  (10 days aggregation). Experimental spectra (black), fast component (dark cyan), medium component (blue), slow component (violet). Total simulation (red). For further details see the text.

## Chapter 6

In Table 6.2 the  $\tau_r$  values of these components are given and compared to the  $\tau_r$  value of R1A $\beta$  from M. Hashemi Shabestari et al.<sup>65</sup> The A $\beta$ 40 variant R1A $\beta$  contains an MTSL attached to a cysteine at the same position as the TOAC in T0A $\beta$ . The fastest  $\tau_r$ , assigned to monomeric A $\beta$ , is roughly seven times faster for T0A $\beta$  than for T26A $\beta$ . The fast component for T0A $\beta$  has a smaller  $\tau_r$  than R1A $\beta$ , even though we would have expected a higher mobility for the MTSL spin label.

**Table 6.2** The rotational correlation times of the components of T0A $\beta$ , T26A $\beta$  and their percentages before and after aggregation. Comparison with the  $\tau_r$  of MTSL labeled A $\beta$  from M. Hashemi Shabestari et al.<sup>65</sup>

	T0A $\beta$			T26A $\beta$			R1A $\beta$ <sup>65</sup>
	[ns]	time 0 [%]	7 days [%]	[ns]	time 0 [%]	7 days [%]	[ns]
$\tau_r$ fast	$0.151 \pm 0.004$	$82 \pm 6$	$36 \pm 2$	$1.071 \pm 0.050$	100%	$93 \pm 1$	$0.19 \pm 0.02$
$\tau_r$ medium	$3.162 \pm 0.410$	$18 \pm 6$	$64 \pm 2$	-	-	-	
$\tau_r$ slow	-	-	-	> 10	-	$7 \pm 1$	

In T0A $\beta$  a slower component of  $\tau_r$  (medium) is already present at the start of the aggregation with a contribution of ca. 20 %. Considering that we assigned the fastest  $\tau_r$  to the monomeric A $\beta$ , this medium component could be related to the presence of some aggregates. After aggregation, the amount by which this fraction contributes to the spectra has increased to 64 %, which suggests that more than half of the T0A $\beta$  has aggregated.

In T26A $\beta$  at the start of aggregation only one component is present, again assigned to monomers. After aggregation this fast component is still dominant, with the appearance of a small percentage of a component with lower mobility, which we refer to as the slow component.

In Figure 6.4 the effect of CP-2 on T0A $\beta$  and T26A $\beta$  is shown. Spectra with the inhibitor (CP-2 5:1 molar ratio) show additional broad lines at the low and high field side of the spectra, e.g. at  $B_0 = 347.5$  mT and 354 mT in Figure 6.4b and d. This shows that the mobility of the spin labels is reduced by the interaction with CP-2.

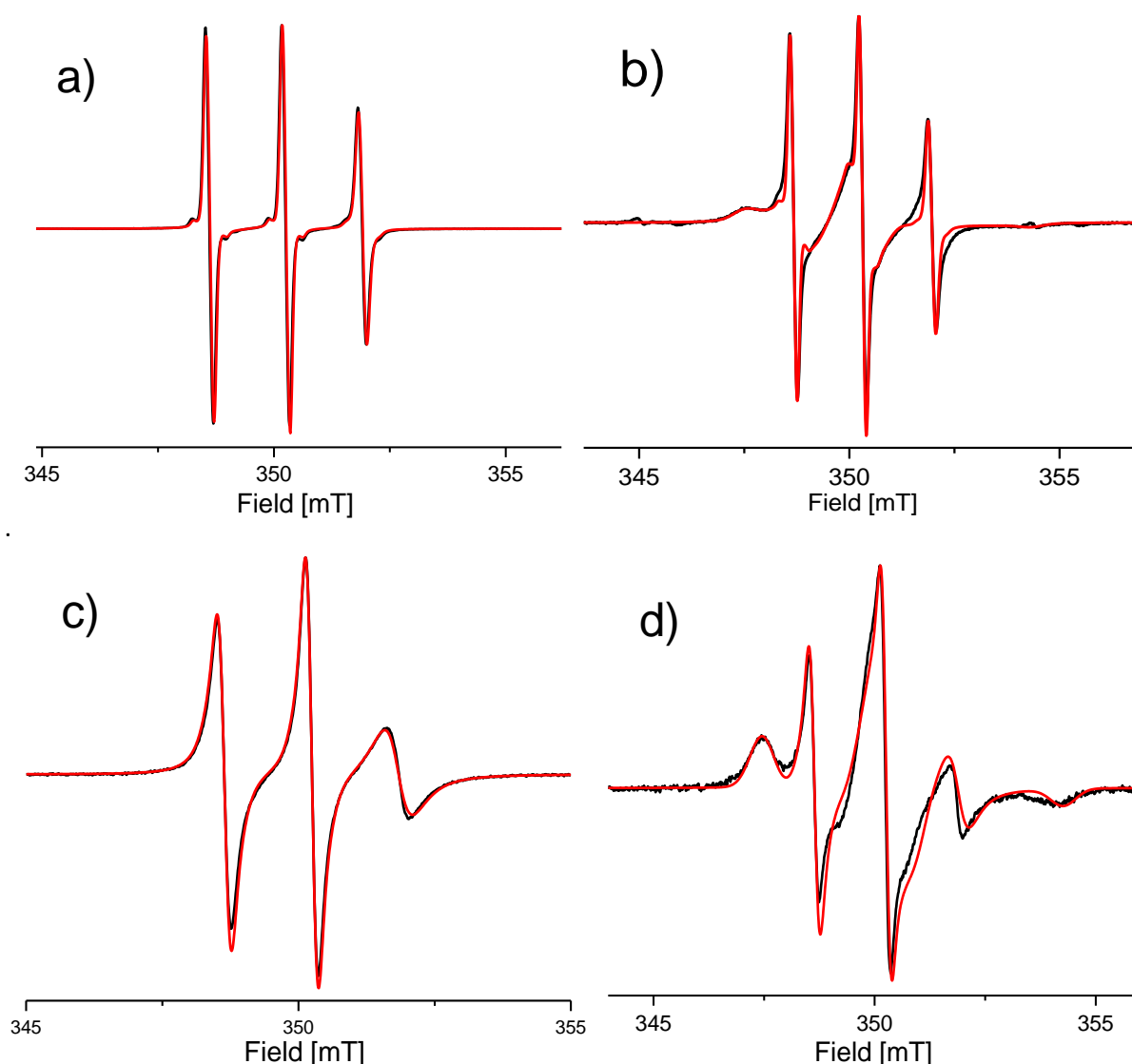


**Figure 6.4** Comparison of EPR spectra of TOAC A $\beta$  constructs with and without CP-2 before aggregation. a) T0A $\beta$  200  $\mu$ M. b) T0A $\beta$  + 1 mM CP-2. c) T26A $\beta$  200  $\mu$ M. d) T26A $\beta$  + 1 mM CP-2. Black: experimental spectra. Red: simulations.

In the Table 6.3 the  $\tau_r$  values of these components are given. The fast and medium components are identical to those given in Table 6.2. The slow component is now present also for T0A $\beta$ . Figure 6.5 shows the shape of these components for the spectra shown in Figure 6.4b and d. Compared to the spectra of the T0A $\beta$  without CP-2, the interaction with the inhibitor results in a new component (Figure 6.5a, blue line) with a larger  $\tau_r$  compared to the fast and medium components. Figure 6.5b shows the components used to simulate the T26A $\beta$  peptide in the presence of CP-2.

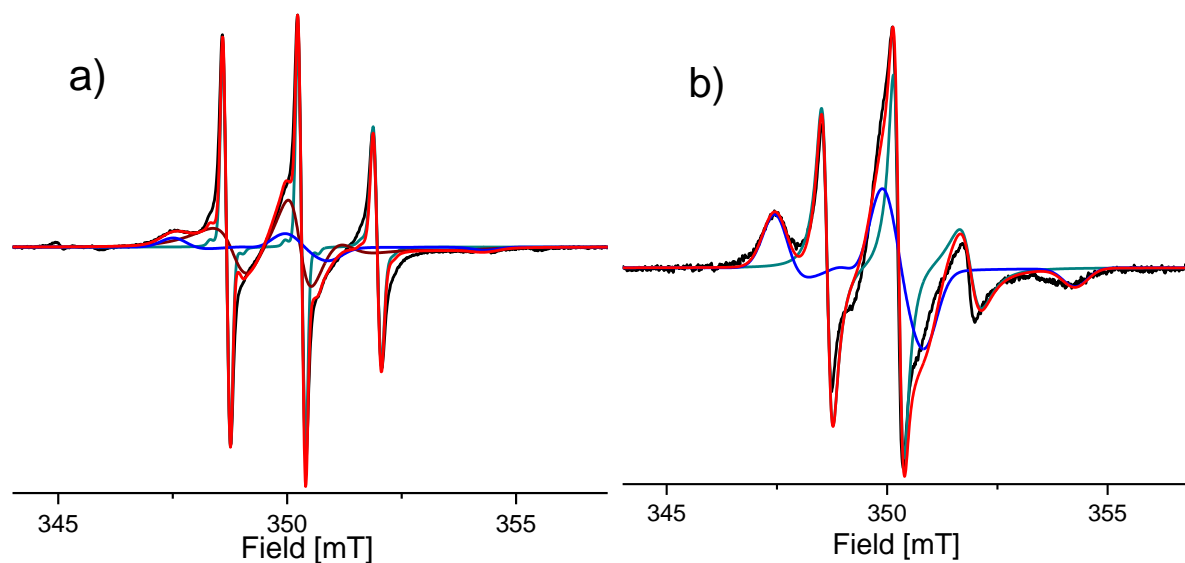


**Figure 6.5** Spectral components used in the simulation of the 9 GHz EPR spectrum of T0A $\beta$  200  $\mu$ M + 1 mM CP-2. Experimental spectra (black), fast component (dark cyan), medium component (wine), slow component (blue). Total simulation (red). For further details see the text.

**Table 6.3** Rotational correlation times of the components of T0A $\beta$  and T26A $\beta$  in the presence of CP-2 and comparison with the  $\tau_r$  of MTSL labeled CP-2 (R1CP-2).

	<b>T0A<math>\beta</math></b>	<b>T26A<math>\beta</math></b>	<b>R1CP-2</b>
	[ns]	[ns]	[ns]
$\tau_r$ fast	$0.151 \pm 0.004$	$1.071 \pm 0.050$	$0.141 \pm 0.003$
$\tau_r$ medium	$3.162 \pm 0.410$	-	
$\tau_r$ slow	> 10	> 10	

The amounts by which the individual components contribute to the spectra are plotted in Figure 6.6. In addition to the molar ratio of A $\beta$  : CP-2 of 1 : 5, two more ratios are tested, leading to the full set of 1:0.5, 1:1 and 1:5 (for individual spectra, see Figures S6.1).

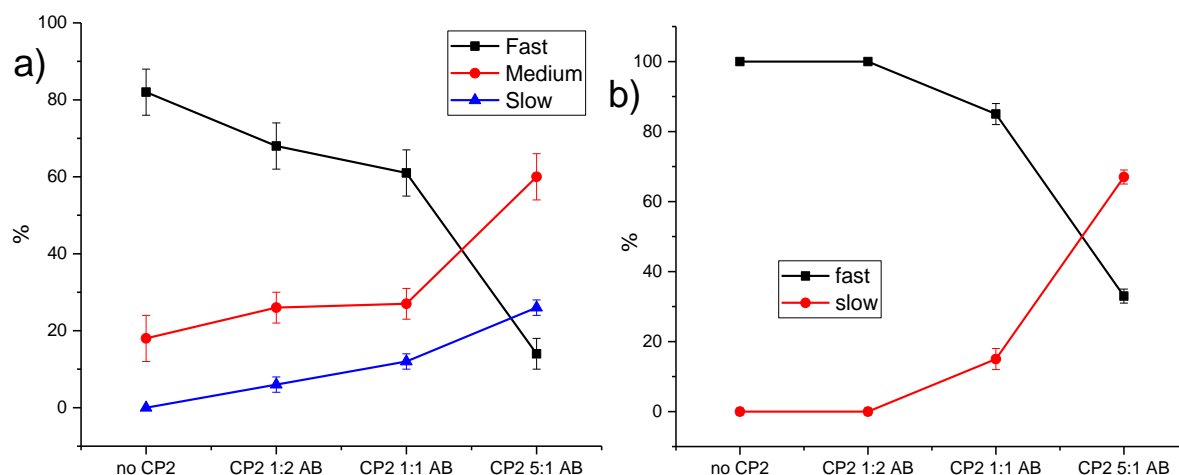


**Figure 6.6** Effects of various ratios of CP-2:A $\beta$  on EPR spectra. a) Amount of fast, medium and slow components in the EPR spectra simulations of T0A $\beta$ : fast (black), medium (red) and slow (blue). b) Amount of fast and slow components in the EPR spectra of T26A $\beta$ : fast (black), slow (red). The lines are a guide to the eye. For details see text.

The difference between the contribution of spectral components in the absence and presence of CP-2 on T0A $\beta$  and T26A $\beta$  at a CP-2 :A $\beta$  ratio of 1:2 are considered not significant, given the experimental errors.

## 6.4 Discussion

We synthesized two variants of the A $\beta$  peptide with the TOAC spin label in different positions in the A $\beta$  chain: at the N-terminus (T0A $\beta$ ) and in a central position (T26A $\beta$ ) (Table 6.1). We use TOAC because it reports more faithfully on the backbone mobility of the peptide, however, it is also known to induce  $\alpha$ -helical structures<sup>77–79,82,93,200</sup> and therefore may influence the peptide conformation and reactions. To test this we test the ability of the newly synthesized peptides to aggregate.

### 6.4.1 EPR properties of monomers

The nitroxide in T26A $\beta$  has a higher  $\tau_r$  value than that of T0A $\beta$ . As both peptides should have almost the same molecular weight (only 2 % difference) and thereby the same volume, the Stokes-Einstein relation (Eqn. S6.1) predicts that both peptides should have similar  $\tau_r$  values. The faster  $\tau_r$  of T0A $\beta$  therefore must reflect a higher local backbone flexibility at the N-terminus than in the middle of peptide.

This local mobility apparently is so high that the  $\tau_r$  of the nitroxide in T0A $\beta$  is smaller



than the one of R1A $\beta$ <sup>65,201</sup>. That is surprising because for the MTSL spin-label the rotation about the single bonds linking the nitroxide to the peptide backbone (see Figure 6.1a) should dominate the motion, which is not possible for TOAC. It is possible that sample conditions, such as the high peptide concentration of 0.55 mM<sup>65</sup> contribute to this difference. An indication for such an effect is that the  $\tau_r$  values differences of  $\tau_r$  found for R1A $\beta$  in another study<sup>201</sup> also differ from those in ref.<sup>65</sup>. Further experiments are needed to clarify this point. Also the center of the peptide is not devoid of local mobility: the  $\tau_r$  expected from the molecular volume is 25 % longer than that measured for T26A $\beta$ .

### ***6.4.2 Influence of TOAC on aggregation behavior***

Qualitatively, T0A $\beta$  aggregates similarly to A $\beta$  wild type. More detailed studies are needed to reveal in how far the time scale and the concentration dependence also agree. In contrast to T0A $\beta$ , T26A $\beta$  hardly shows signs of amyloid aggregation: ThioT levels remain low and immobilization, observed by EPR, occurs on a much lower level than for T0A $\beta$ . As the literature does not report such a trend for the R1 derivatives of A $\beta$ <sup>65,201</sup>, we assume that the main factor is the presence of the TOAC amino acid. Further studies are needed to determine the role played by TOAC in such a context, however we can already indicate two possible factors combining to inhibit the aggregation: Crowding in the middle of the  $\beta$ -sheet structure of the fibril, and the  $\alpha$ -helix-inducing properties of TOAC<sup>77–79,82,93,200</sup>.

### ***6.4.3 Cyclic peptide CP-2 as amyloid aggregation inhibitor***

Having established that TOAC enables tracking the aggregation properties of A $\beta$  at different positions, we use it to analyze the interaction between the labeled peptides and the CP-2 inhibitor. ThioT fluorescence (Figure S6.3) shows that the effect of CP-2 on the formation of fibrils for our TOAC labeled peptides is similar to what has been previously observed by Rahimipour et al.<sup>188,189</sup> for the A $\beta$  WT: CP-2 inhibits A $\beta$  aggregation. The EPR experiments confirm a direct interaction between CP-2 and the TOAC labeled A $\beta$  peptides: A new component appears in both T0A $\beta$  and T26A $\beta$  spectra. This component has a  $\tau_r$  that is larger than the  $\tau_r$  in the absence of CP-2, which suggests a complete immobilization of the peptide, or at least a  $\tau_r$  larger than 10 ns. In chapter 3 we have shown that by cw EPR the number of peptide units present in the aggregates can be estimated<sup>197</sup>. Following the same principle we tried to determine the composition of the aggregates and the limits of the detection. Considering the molecular weight of the TOAC labeled A $\beta$  peptides (4500 Da, see Materials and methods), seven is the highest amount of units in an aggregate that would have a non-immobilized EPR spectrum in the absence of local mobility of the spin label. As CP-2 has a molecular weight (787 Da) that is lower

than that of A $\beta$ , a maximum of 34 CP-2 units added to one A $\beta$  peptide would result in immobilized spectra. The presence of CP-2 gives rise to a completely immobilized  $\tau_r$ , so we can assume that T0A $\beta$  and T26A $\beta$  get partially trapped in large units formed with the inhibitor.

The results of the EPR experiments on the spin-labeled version of CP-2 (R1CP-2) (see SI) reveal that CP-2 indeed strongly interacts with itself. A dominant fraction of R1CP-2 has a spectrum (Figure S6.4) that is characteristic of strong spin-spin exchange, which suggests the interaction of more than ten R1 residues, with R1-R1 distances around 4-5 Å<sup>202,203</sup>. Such an interaction is fully consistent with the model of in-register- $\beta$ -sheet stacking proposed by Rahimipour et al.<sup>188,189</sup>

## 6.5 Conclusions

Here we show that A $\beta$  peptides labeled with TOAC at strategic positions open new ways to study the amyloid aggregation: The real-time measurement of rotational motion reveals different mobility at the two sites investigated in A $\beta$ , giving a better understanding of the interactions involved in the aggregation process. The TOAC at the N-terminal position in A $\beta$  (T0A $\beta$ ) seems to have no impact into the formation of fibrils, whereas the TOAC at center of the peptide partially inhibits its aggregation. The T26A $\beta$  gives us a better understanding of the total mobility of the peptide, however it seems to influence the aggregation process.

We use these two labeled A $\beta$  peptides to better understand the effect of the anti-amyloidogenic cyclic D,L- $\alpha$ -peptide CP-2 on the aggregation process. We prove that CP-2, above a certain ratio with A $\beta$ , forms instantaneously a construct that immobilizes the amyloid peptide and blocks the formation of fibrils. By using cw EPR on a MTSL labeled CP-2 (R1CP-2) we show that, under our experimental conditions, the inhibitor forms a macromolecular structure by itself, which suggests that, if present, A $\beta$  gets trapped into such structures, blocking the fibril formation.

New strategic positions for the labels in A $\beta$  could be used to better define their influence in the aggregation process. Such research could be used to better observe the presence of relevant A $\beta$  forms, e.g. oligomers. Further experiments should be done to determine the structure of the A $\beta$ -CP-2 aggregates and the exact source of the interaction of CP-2 with the A $\beta$  peptide.

## 6.6 Supporting information

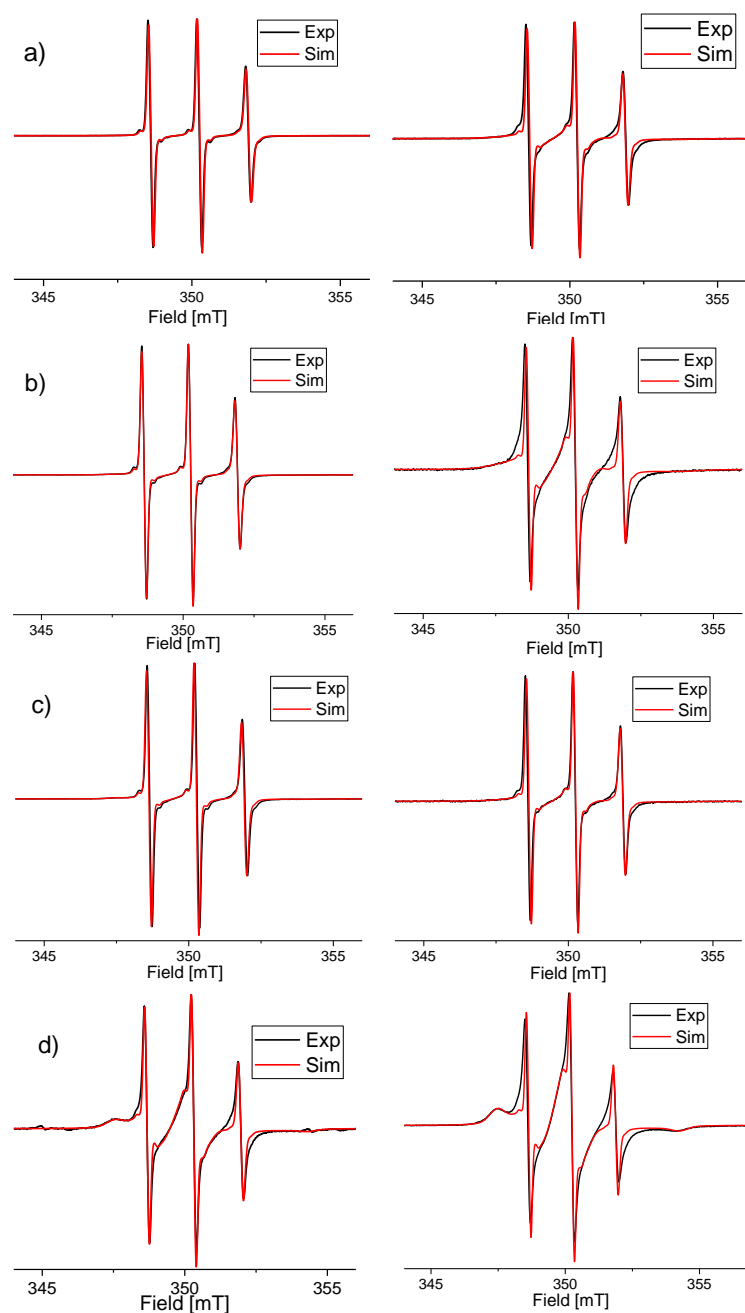


**Figure S6.1** Room temperature 9 GHz EPR spectra of T0A $\beta$  200  $\mu$ M + CP-2 before and after aggregation. Left column: EPR spectra at time 0. Right column: EPR spectra after 7 days of aggregation. Spectra a) no CP-2, b) 100  $\mu$ M CP-2, c) 200  $\mu$ M CP-2, d) 1 mM CP-2. Black: Experimental spectra. Red: Simulated spectra. Remaining experimental conditions and detailed description: See main text.

## Chapter 6

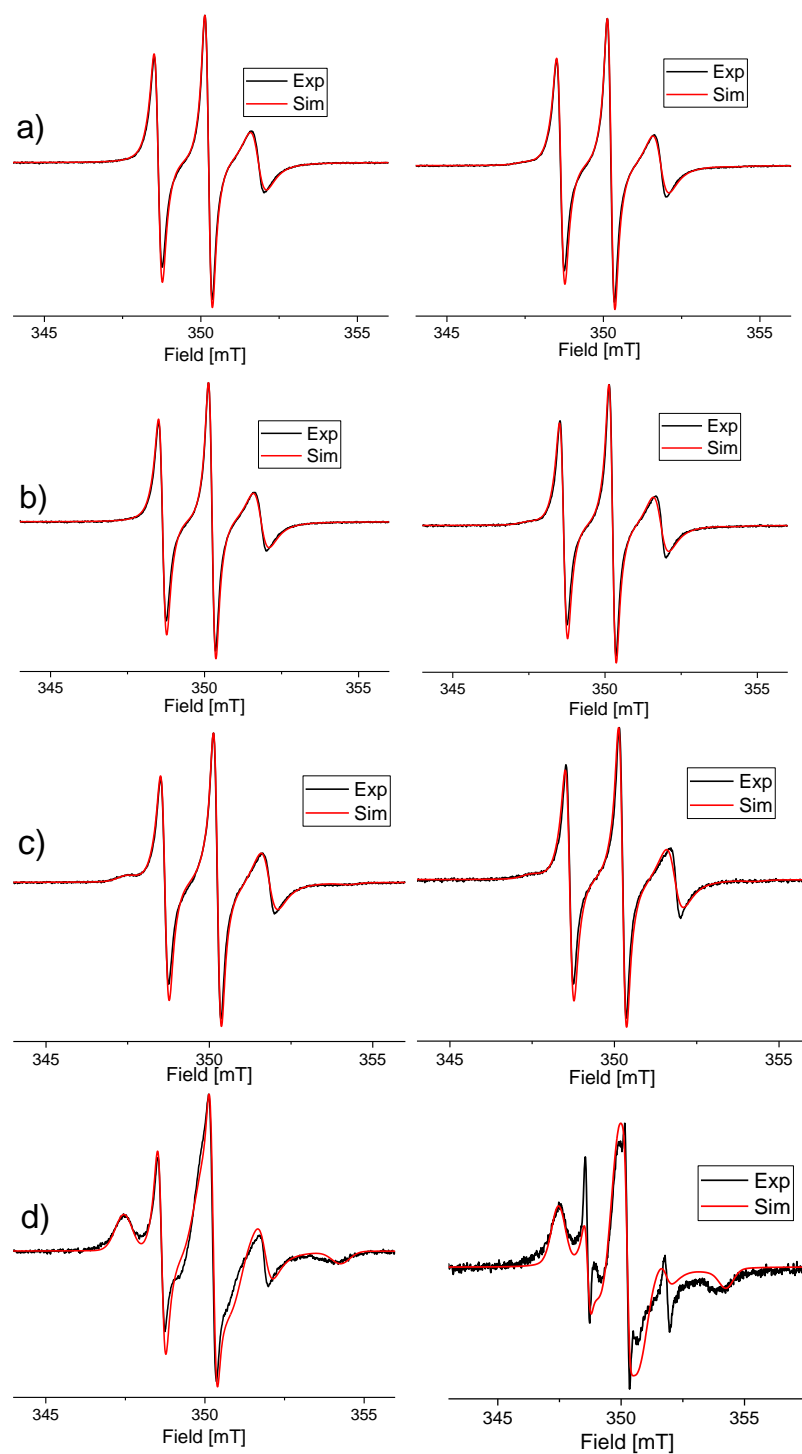


**Figure S6.2** Room temperature 9 GHz EPR spectra of T26A $\beta$  200  $\mu$ M + CP-2 before and after aggregation. Left column: EPR spectra at time 0. Right column: EPR spectra after 7 days of aggregation. Spectra a) no CP-2, b) 100  $\mu$ M CP-2, c) 200  $\mu$ M CP-2, d) 1 mM CP-2.

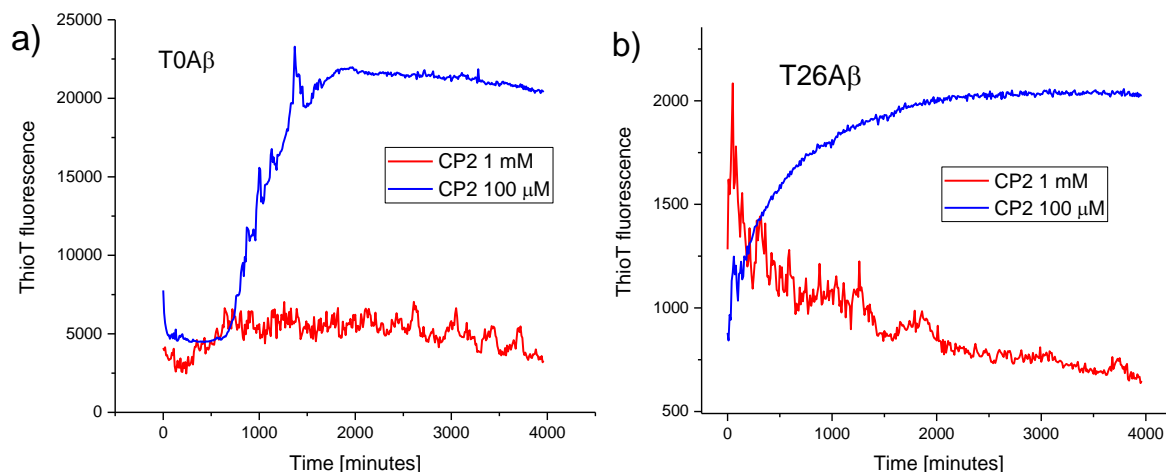


**Figure S6.3** Inhibitory effect of CP-2 on T0Aβ and T26Aβ detected by ThioT fluorescence in plate reader. a) ThioT fluorescence kinetics of T0Aβ 200 μM incubated for 3 days at 37 °C in the presence of CP-2 at concentration 100 μM (blue) and 1 mM (red). b) ThioT fluorescence kinetics of T26Aβ 200 μM incubated for 3 days at 37 °C in the presence of CP-2 at concentration 100 μM (blue) and 1 mM (red). For more details, see main text.

### 6.6.1 Interpretation of $\tau_r$ values and molecular volumes

We used the Stokes-Einstein equation to interpret the  $\tau_r$  values. This implies a spherical approximation for the particles:

$$\tau_r = \frac{4\pi\eta\alpha^3}{3kT} = \frac{\eta}{kT} V_{EPR} \quad (\text{S6.1})$$

In Eqn. (S6.1)  $k$  is the Boltzmann constant,  $T$  is the temperature (293 K),  $\eta$  is the viscosity of the solvent (1.05 cP for 10 % DMSO in water<sup>204</sup>) and  $\alpha$  is the hydrodynamic radius.

The volumes of the peptide and its aggregates can be derived by using the molecular weight (MW) and a certain density of the proteins using Eqn. (S6.2):

$$V = \frac{MW}{N_A \rho} \quad (\text{S6.2})$$

Here,  $\rho$  is the protein density,  $N_A$  is Avogadro's constant.

By comparing the volumes obtained by Eqn. S6.1 with the ones relative to a certain molecular weight we can estimate the number of units comprising an aggregate. For more details, see Chapter 3 of this thesis.

### 6.6.2 EPR experiments on spin-labeled CP-2

To detect the influence of CP-2 on the aggregation of Aβ, initial experiments of spin labeled CP-2 (R1CP-2) with and without Aβ were performed. The nitroxide was attached

to the CP-2 to a cysteine in position 6 in the sequence via a iodoacetamide labeling reaction. Sequence R1CP-2: [I-J-w-H-s-R1]

The same protocol used to prepare the TOAC labeled peptide samples was used for the R1CP-2 samples, but the final concentrations of A $\beta$  WT was 400  $\mu$ M and R1CP-2 was 200  $\mu$ M. As a reference, a sample of pure R1CP-2 at a concentration of 200  $\mu$ M without A $\beta$  was prepared.

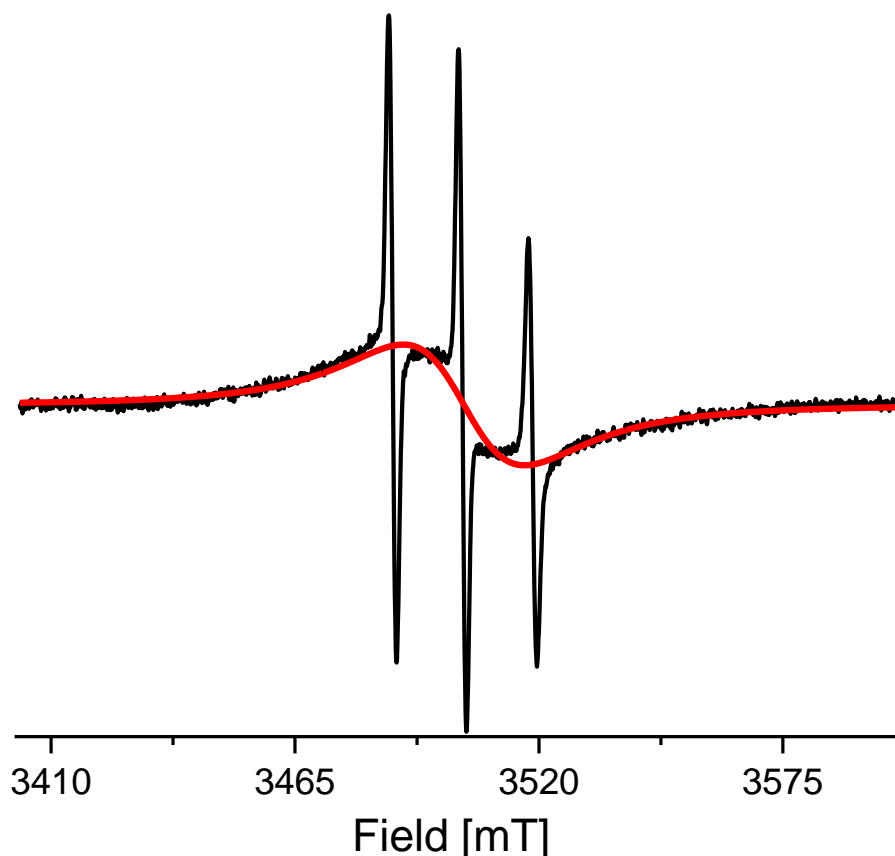


**Figure S6.4** Spin-spin exchange interaction in a aggregated solution of R1CP-2. Experimental 9 GHz EPR spectrum (black) and fitted Lorentzian derivative of the broadened signal (red).

Figure S6.4 shows the 9 GHz EPR spectrum of the reference sample taken at time 0. The three-line pattern of the nitroxide radical is visible, however the spectrum is dominated by a broad band, which can be related to spin-spin interactions between the labels. The Lorentzian-derivative fitting of the broad band (red) tells us that more than 95 % of the labels are subject to such interactions. The R1CP-2 was completely labeled, therefore, there was no diamagnetic dilution in the sample. If macromolecular aggregates are formed, confining the labels to distances in the range of 5 Å<sup>202,203</sup>, such an exchange-broadened signal is expected. The measurements done with A $\beta$  WT show the same results (spectra not shown), showing that the interaction between inhibitor and A $\beta$  cannot be detected under these conditions.

# Bibliography

1. Brocchieri, L. & Karlin, S. Protein length in eukaryotic and prokaryotic proteomes. *Nucleic Acids Res.* **33**, 3390–3400 (2005).
2. Petsko, G. A. & Ringe, D. *Protein structure and function*. (New Science Press, 2004).
3. Richardson, J. S. The Anatomy and Taxonomy of Protein Structure. in (eds. Anfinsen, C. B., Edsall, J. T. & Richards, F. M. B. T.-A. in P. C.) **34**, 167–339 (Academic Press, 1981).
4. Dunker, A. K. *et al.* Intrinsically disordered protein. *J. Mol. Graph. Model.* **19**, 26–59 (2001).
5. Dyson, H. J. & Wright, P. E. Intrinsically unstructured proteins and their functions. *Nat. Rev. Mol. cell Biol.* **6**, 197–208 (2005).
6. Kumar, S., Mohanty, S. K. & Udgaonkar, J. B. Mechanism of formation of amyloid protofibrils of barstar from soluble oligomers: evidence for multiple steps and lateral association coupled to conformational conversion. *J. Mol. Biol.* **367**, 1186–1204 (2007).
7. Tompa, P. Intrinsically disordered proteins: a 10-year recap. *Trends Biochem. Sci.* **37**, 509–516 (2012).
8. Wright, P. E. & Dyson, H. J. Intrinsically disordered proteins in cellular signalling and regulation. *Nat. Rev. Mol. cell Biol.* **16**, 18–29 (2015).
9. Fändrich, M. & Dobson, C. M. The behaviour of polyamino acids reveals an inverse side chain effect in amyloid structure formation. *EMBO J.* **21**, 5682–5690 (2002).
10. Greenwald, J. & Riek, R. Biology of amyloid: structure, function, and regulation. *Structure* **18**, 1244–1260 (2010).
11. Rose, A. S. *et al.* NGL viewer: web-based molecular graphics for large complexes. *Bioinformatics* **34**, 3755–3758 (2018).
12. Kirschner, D. A., Abraham, C. & Selkoe, D. J. X-ray diffraction from intraneuronal paired helical filaments and extraneuronal amyloid fibers in Alzheimer disease indicates cross-beta conformation. *Proc. Natl. Acad. Sci.* **83**, 503–507 (1986).
13. Liberta, F. *et al.* Cryo-EM fibril structures from systemic AA amyloidosis reveal the species complementarity of pathological amyloids. *Nat. Commun.* **10**, 1–10 (2019).
14. Xue, W.-F. *et al.* Fibril fragmentation enhances amyloid cytotoxicity. *J. Biol. Chem.* **284**, 34272–34282 (2009).
15. Kodali, R. & Wetzel, R. Polymorphism in the intermediates and products of amyloid assembly. *Curr. Opin. Struct. Biol.* **17**, 48–57 (2007).
16. Caughey, B. & Lansbury Jr, P. T. Protofibrils, pores, fibrils, and neurodegeneration: separating the responsible protein aggregates from the innocent bystanders. *Annu. Rev. Neurosci.* **26**, 267–298 (2003).
17. Kirkitadze, M. D., Bitan, G. & Teplow, D. B. Paradigm shifts in Alzheimer's disease and other neurodegenerative disorders: the emerging role of oligomeric assemblies. *J. Neurosci. Res.* **69**, 567–577 (2002).
18. Haass, C. & Selkoe, D. J. Soluble protein oligomers in neurodegeneration: Lessons from the

- Alzheimer's amyloid  $\beta$ -peptide. *Nat. Rev. Mol. Cell Biol.* **8**, 101–112 (2007).
19. van Diggelen, F., Tepper, A. W. J. W., Apetri, M. M. & Otzen, D. E.  $\alpha$ -Synuclein Oligomers: A Study in Diversity. *Isr. J. Chem.* **57**, 699–723 (2017).
  20. Kaye, R. *et al.* Common structure of soluble amyloid oligomers implies common mechanism of pathogenesis. *Science*. **300**, 486–489 (2003).
  21. Portelius, E., Mattsson, N., Andreasson, U., Blennow, K. & Zetterberg, H. Novel A $\beta$  isoforms in Alzheimer's Disease-Their Role in Diagnosis and Treatment. *Curr. Pharm. Des.* **17**, 2594–2602 (2011).
  22. Jakob-Roetne, R. & Jacobsen, H. Alzheimer's disease: from pathology to therapeutic approaches. *Angew. Chemie Int. Ed.* **48**, 3030–3059 (2009).
  23. Chopra, K., Misra, S. & Kuhad, A. Neurobiological aspects of Alzheimer's disease. *Expert Opin. Ther. Targets* **15**, 535–555 (2011).
  24. Lanctôt, K. L. *et al.* Neuropsychiatric signs and symptoms of Alzheimer's disease: New treatment paradigms. *Alzheimer's Dement. Transl. Res. Clin. Interv.* **3**, 440–449 (2017).
  25. Braak, H. *et al.* Pattern of brain destruction in Parkinson's and Alzheimer's diseases. *J. Neural Transm.* **103**, 455–490 (1996).
  26. Selkoe, D. J. Alzheimer's disease: genes, proteins, and therapy. *Physiol. Rev.* **81**, 741–766 (2001).
  27. Gralle, M. & Ferreira, S. T. Structure and functions of the human amyloid precursor protein: the whole is more than the sum of its parts. *Prog. Neurobiol.* **82**, 11–32 (2007).
  28. Serra-Batiste, M. *et al.* A $\beta$ 42 assembles into specific  $\beta$ -barrel pore-forming oligomers in membrane-mimicking environments. *Proc. Natl. Acad. Sci.* **113**, 10866 LP – 10871 (2016).
  29. Cline, E. N., Bicca, M. A., Viola, K. L. & Klein, W. L. The amyloid- $\beta$  oligomer hypothesis: Beginning of the third decade. *J. Alzheimer's Dis.* **64**, S567–S610 (2018).
  30. Hayden, E. Y. & Teplow, D. B. Amyloid  $\beta$ -protein oligomers and Alzheimer's disease. *Alzheimers. Res. Ther.* **5**, 60 (2013).
  31. Lee, S. J. C., Nam, E., Lee, H. J., Savellieff, M. G. & Lim, M. H. Towards an understanding of amyloid- $\beta$  oligomers: characterization, toxicity mechanisms, and inhibitors. *Chem. Soc. Rev.* **46**, 310–323 (2017).
  32. Parkinson, J. An Essay on the Shaking Palsy (London: Sherwood, Neely and Jones). (1817).
  33. Cookson, M. R.  $\alpha$ -Synuclein and neuronal cell death. *Mol. Neurodegener.* **4**, 9 (2009).
  34. De Rijk, M. C. *et al.* Prevalence of Parkinson's disease in the elderly: the Rotterdam Study. *Neurology* **45**, 2143–2146 (1995).
  35. Ozansoy, M. & Başak, A. N. The central theme of Parkinson's disease:  $\alpha$ -synuclein. *Mol. Neurobiol.* **47**, 460–465 (2013).
  36. Venda, L. L., Cragg, S. J., Buchman, V. L. & Wade-Martins, R.  $\alpha$ -Synuclein and dopamine at the crossroads of Parkinson's disease. *Trends Neurosci.* **33**, 559–568 (2010).
  37. Sun, J. *et al.* Functional cooperation of  $\alpha$ -synuclein and VAMP2 in synaptic vesicle recycling. *Proc. Natl. Acad. Sci. U. S. A.* **116**, 11113–11115 (2019).
  38. Chen, S. W. *et al.* Structural characterization of toxic oligomers that are kinetically trapped



- during  $\alpha$ -synuclein fibril formation. *Proc. Natl. Acad. Sci.* **112**, E1994 LP-E2003 (2015).
39. Cremades, N. *et al.* Direct observation of the interconversion of normal and toxic forms of  $\alpha$ -synuclein. *Cell* **149**, 1048–1059 (2012).
  40. Merrifield, R. B. Solid phase peptide synthesis. I. The synthesis of a tetrapeptide. *J. Am. Chem. Soc.* **85**, 2149–2154 (1963).
  41. Atherton, N. M. *Principles of electron spin resonance*. (Ellis Horwood Limited, 1993).
  42. Roessler, M. M. & Salvadori, E. Principles and applications of EPR spectroscopy in the chemical sciences. *Chem. Soc. Rev.* **47**, 2534–2553 (2018).
  43. Brustolon, M. R. *Principles and Applications of Electron Paramagnetic Resonance Spectroscopy*. (John Wiley & Sons, 2008).
  44. Briere, R., Lemaire, H. & Rassat, A. NITROXYDES 15-SYNTHESE ET ETUDE DE RADICAUX LIBRES STABLES PIPERIDINIQUES ET PYRROLIDINIQUE. *Bull. Soc. Chim. Fr.* 3273 (1965).
  45. Hubbell, W. L. & Altenbach, C. Investigation of structure and dynamics in membrane proteins using site-directed spin labeling. *Curr. Opin. Struct. Biol.* **4**, 566–573 (1994).
  46. Hubbell, W. L., Mchaourab, H. S., Altenbach, C. & Lietzow, M. A. Watching proteins move using site-directed spin labeling. *Structure* **4**, 779–783 (1996).
  47. Hubbell, W. L., Cafiso, D. S. & Altenbach, C. Identifying conformational changes with site-directed spin labeling. *Nat. Struct. Biol.* **7**, 735–739 (2000).
  48. Stoll, S. & Schweiger, A. EasySpin, a comprehensive software package for spectral simulation and analysis in EPR. *J. Magn. Reson.* **178**, 42–55 (2006).
  49. Milov, A. D., Ponomarev, A. B. & Tsvetkov, Y. D. Electron-electron double resonance in electron spin echo: Model biradical systems and the sensitized photolysis of decalin. *Chem. Phys. Lett.* **110**, 67–72 (1984).
  50. Schiemann, O. & Prisner, T. F. Long-range distance determinations in biomacromolecules by EPR spectroscopy. *Q. Rev. Biophys.* **40**, 1 (2007).
  51. Bowman, M. K., Maryasov, A. G., Kim, N. & DeRose, V. J. Visualization of distance distribution from pulsed double electron-electron resonance data. *Appl. Magn. Reson.* **26**, 23–39 (2004).
  52. Chiang, Y. W., Borbat, P. P. & Freed, J. H. The determination of pair distance distributions by pulsed ESR using Tikhonov regularization. *J. Magn. Reson.* **172**, 279–295 (2005).
  53. Jeschke, G., Panek, G., Godt, A., Bender, A. & Paulsen, H. Data analysis procedures for pulse ELDOR measurements of broad distance distributions. *Appl. Magn. Reson.* **26**, 223 (2004).
  54. Jeschke, G. *et al.* DeerAnalysis2006—a comprehensive software package for analyzing pulsed ELDOR data. *Appl. Magn. Reson.* **30**, 473–498 (2006).
  55. Jeschke, G. & Polyhach, Y. Distance measurements on spin-labelled biomacromolecules by pulsed electron paramagnetic resonance. *Phys. Chem. Chem. Phys.* **9**, 1895–910 (2007).
  56. Jeschke, G. *et al.* DeerAnalysis2006 - A comprehensive software package for analyzing pulsed ELDOR data. *Appl. Magn. Reson.* **30**, 473–498 (2006).
  57. Mchaourab, H. S., Lietzow, M. A., Hideg, K. & Hubbell, W. L. Motion of spin-labeled side chains in T4 lysozyme. Correlation with protein structure and dynamics. *Biochemistry* **35**, 7692–7704 (1996).

58. Jeschke, G. DEER Distance Measurements on Proteins. *Annu. Rev. Phys. Chem.* **63**, 419–446 (2012).
59. Fajer, P. G. Site directed spin labelling and pulsed dipolar electron paramagnetic resonance (double electron–electron resonance) of force activation in muscle. *J. Phys. Condens. Matter* **17**, S1459–S1469 (2005).
60. Shabestari, M. H., Wolfs, C. J. A. M., Spruijt, R. B., Van Amerongen, H. & Huber, M. Exploring the structure of the 100 amino-acid residue long N-terminus of the plant antenna protein CP29. *Biophys. J.* **106**, 1349–1358 (2014).
61. Drescher, M., Huber, M. & Subramaniam, V. Hunting the Chameleon: Structural Conformations of the Intrinsically Disordered Protein Alpha-Synuclein. *ChemBioChem* **13**, 761–768 (2012).
62. Petrlova, J. *et al.* A differential association of Apolipoprotein E isoforms with the amyloid- $\beta$  oligomer in solution. *Proteins* **79**, 402–16 (2011).
63. Grimaldi, M. *et al.* Membrane charge dependent states of the  $\beta$ -amyloid fragment A $\beta$  (16–35) with differently charged micelle aggregates. *Biochim. Biophys. Acta (BBA)-Biomembranes* **1798**, 660–671 (2010).
64. Shabestari, M. *et al.* The Aggregation Potential of the 1-15- and 1-16-Fragments of the Amyloid  $\beta$  Peptide and Their Influence on the Aggregation of A $\beta$ 40. *Appl. Magn. Reson.* **44**, 1167–1179 (2013).
65. Shabestari, M. H., Meeuwenoord, N. J., Filippov, D. V. & Huber, M. Interaction of the amyloid  $\beta$  peptide with sodium dodecyl sulfate as a membrane-mimicking detergent. *J. Biol. Phys.* **42**, 299–315 (2016).
66. Hashemi Shabestari, M. *et al.* Three Long-Range Distance Constraints and an Approach Towards a Model for the  $\alpha$ -Synuclein-Fibril Fold. *Appl. Magn. Reson.* **46**, 369–388 (2015).
67. Laganowsky, A. *et al.* Atomic view of a toxic amyloid small oligomer. *Science* **335**, 1228–31 (2012).
68. Georgieva, E. R., Borbat, P. P., Ginter, C., Freed, J. H. & Boudker, O. Conformational ensemble of the sodium-coupled aspartate transporter. *Nat. Struct. Mol. Biol.* **20**, 215–221 (2013).
69. Dunkel, S., Pulagam, L. P., Steinhoff, H.-J. & Klare, J. P. *In vivo* EPR on spin labeled colicin A reveals an oligomeric assembly of the pore-forming domain in *E. coli* membranes. *Phys. Chem. Chem. Phys.* **17**, 4875–4878 (2015).
70. Warshaviak, D. T., Khramtsov, V. V., Cascio, D., Altenbach, C. & Hubbell, W. L. Structure and dynamics of an imidazoline nitroxide side chain with strongly hindered internal motion in proteins. *J. Magn. Reson.* **232**, 53–61 (2013).
71. Stoller, S., Sicoli, G., Baranova, T. Y., Bennati, M. & Diederichsen, U. TOPP: A novel nitroxide-labeled amino acid for EPR distance measurements. *Angew. Chemie - Int. Ed.* **50**, 9743–9746 (2011).
72. Jeschke, G. Conformational dynamics and distribution of nitroxide spin labels. *Prog. Nucl. Magn. Reson. Spectrosc.* **72**, 42–60 (2013).
73. Fawzi, N. L. *et al.* A rigid disulfide-linked nitroxide side chain simplifies the quantitative analysis of PRE data. *J. Biomol. NMR* **51**, 105–114 (2011).
74. Schilder, J. *et al.* Protein docking using an ensemble of spin labels optimized by intra-

- molecular paramagnetic relaxation enhancement. *Phys. Chem. Chem. Phys.* **18**, (2015).
75. Di Valentin, M., Albertini, M., Zurlo, E., Gobbo, M. & Carbonera, D. Porphyrin triplet state as a potential Spin label for nanometer distance measurements by peldor spectroscopy. *J. Am. Chem. Soc.* **136**, 6582–6585 (2014).
  76. Milov, A. D. *et al.* The secondary structure of a membrane-modifying peptide in a supramolecular assembly studied by PELDOR and CW-ESR spectroscopies. *J. Am. Chem. Soc.* **123**, 3784–3789 (2001).
  77. McNulty, J. C. *et al.* Electron spin resonance of TOAC labeled peptides: Folding transitions and high frequency spectroscopy. *Biopolym. - Pept. Sci. Sect.* **55**, 479–485 (2000).
  78. Monaco, V. *et al.* Orientation and immersion depth of a helical lipopeptaibol in membranes using TOAC as an ESR probe. *Biopolymers* **50**, 239–253 (1999).
  79. Toniolo, C., Crisma, M. & Formaggio, F. TOAC, a nitroxide spin-labeled, achiral C $\alpha$ -tetrasubstituted  $\alpha$ -amino acid, is an excellent tool in material science and biochemistry. *Pept. Sci.* **47**, 153–158 (1998).
  80. Chen, K., Liu, Z., Zhou, C., Bracken, W. C. & Kallenbach, N. R. Spin relaxation enhancement confirms dominance of extended conformations in short alanine peptides. *Angew. Chemie - Int. Ed.* **46**, 9036–9039 (2007).
  81. Hansen, P. *et al.* Distinguishing Helix Conformations in Alanine Rich Peptides Using the Unnatural Amino Acid TOAC and Electron Spin Resonance. *J. Am. Chem. Soc.* **118**, 271–272 (1996).
  82. Monaco, V. *et al.* Determining the occurrence of a 310-helix and an  $\alpha$ -helix in two different segments of a lipopeptaibol antibiotic using TOAC, a nitroxide spin-labeled C( $\alpha$ )-tetrasubstituted  $\alpha$ -amino acid. *Bioorganic Med. Chem.* **7**, 119–131 (1999).
  83. Ghimire, H. *et al.* Distance measurements on a dual-labeled TOAC AChR M2 $\delta$  peptide in mechanically aligned DMPC bilayers via dipolar broadening CW-EPR spectroscopy. *J. Phys. Chem. B* **116**, 3866–3873 (2012).
  84. Marchetto, R., Schreier, S. & Nakaie, C. R. A novel spin-labeled amino acid derivative for use in peptide synthesis: (9-fluorenylmethyloxycarbonyl)-2,2,6,6-tetramethylpiperidine-N-oxyl-4-amino-4-carboxylic acid. *J. Am. Chem. Soc.* **115**, 11042–11043 (1993).
  85. Cilli, E. M., Marchetto, R., Schreier, S. & Nakaie, C. R. Correlation between the mobility of spin-labeled peptide chains and resin solvation: An approach to optimize the synthesis of aggregating sequences. *J. Org. Chem.* **64**, 9118–9123 (1999).
  86. Nakaie, C. R. *et al.* Synthesis and pharmacological properties of TOAC-labeled angiotensin and bradykinin analogs. *Peptides* **23**, 65–70 (2002).
  87. Di Valentin, M., Albertini, M., Zurlo, E., Gobbo, M. & Carbonera, D. Porphyrin triplet state as a potential Spin label for nanometer distance measurements by peldor spectroscopy. *J. Am. Chem. Soc.* **136**, 6582–6585 (2014).
  88. Di Valentin, M. *et al.* Light-Induced Porphyrin-Based Spectroscopic Ruler for Nanometer Distance Measurements. *Chem. - A Eur. J.* **22**, (2016).
  89. Milov, A. D. *et al.* Synthesis and conformational properties of a TOAC doubly spin-labeled analog of the medium-length, membrane active peptaibiotic ampullosporin as revealed by CD, fluorescence, and EPR spectroscopies. *Biopolym. - Pept. Sci. Sect.* **102**, 40–48 (2014).

90. Shabestari, M. H. *et al.* Conformation and EPR characterization of rigid, 310-helical peptides with TOAC spin labels: Models for short distances. *Biopolym. - Pept. Sci. Sect.* **102**, 244–251 (2014).
91. Hanson, P. *et al.* Electron spin resonance and structural analysis of water soluble, alanine-rich peptides incorporating TO AC. *Mol. Phys.* **95**, 957–966 (1998).
92. Polese, A. *et al.* First interchain peptide interaction detected by ESR in fully synthetic, template-assisted, two-helix bundles. *J. Am. Chem. Soc.* **121**, 11071–11078 (1999).
93. Hanson, P., Millhauser, G., Formaggio, F., Crisma, M. & Toniolo, C. ESR characterization of hexameric, helical peptides using double TOAC spin labeling. *J. Am. Chem. Soc.* **118**, 7618–7625 (1996).
94. Greenfield, N. & Fasman, G. D. Computed Circular Dichroism Spectra for the Evaluation of Protein Conformation. *Biochemistry* **8**, 4108–4116 (1969).
95. Fasman, G. D. *Circular dichroism and the conformational analysis of biomolecules*. (Springer Science & Business Media, 2013).
96. Chiti, F. & Dobson, C. M. Protein misfolding, functional amyloid, and human disease. *Annu. Rev. Biochem.* **75**, 333–366 (2006).
97. Michaels, T. C. T. *et al.* Chemical Kinetics for Bridging Molecular Mechanisms and Macroscopic Measurements of Amyloid Fibril Formation. *Annu. Rev. Phys. Chem.* **69**, annurev-physchem-050317-021322 (2018).
98. Chiti, F. & Dobson, C. M. Amyloid formation by globular proteins under native conditions. *Nat Chem Biol* **5**, 15–22 (2009).
99. Bordignon E., Steinhoff HJ. Membrane Protein Structure and Dynamics Studied by Site-Directed Spin-Labeling ESR. In: ESR Spectroscopy in Membrane Biophysics. Biological Magnetic Resonance, vol **27**. Springer, Boston, MA(2007)
100. Mchaourab, H. S., Lietzow, M. A., Hideg, K. & Hubbell, W. L. Motion of spin-labeled side chains in T4 lysozyme. Correlation with protein structure and dynamics. *Biochemistry* **35**, 7692–7704 (1996).
101. Hubbell, W. L., Mchaourab, H. S., Altenbach, C. & Lietzow, M. A. Watching proteins move using site-directed spin labeling. *Structure* **4**, 779–783 (1996).
102. Bartucci, R. *et al.* Backbone dynamics of alamethicin bound to lipid membranes: Spin-echo electron paramagnetic resonance of TOAC-spin labels. *Biophys. J.* **94**, 2698–2705 (2008).
103. Hanson, P. *et al.* Electron spin resonance and structural analysis of water soluble, alanine-rich peptides incorporating TO AC. *Mol. Phys.* **95**, 957–966 (1998).
104. Schreier, S. *et al.* Conformational basis for the biological activity of TOAC-labeled angiotensin II and bradykinin: Electron paramagnetic resonance, circular dichroism, and fluorescence studies. *Biopolymers* **74**, 389–402 (2004).
105. Schreier, S., Bozelli, J. C., Marín, N., Vieira, R. F. F. & Nakaie, C. R. The spin label amino acid TOAC and its uses in studies of peptides: Chemical, physicochemical, spectroscopic, and conformational aspects. *Biophys. Rev.* **4**, 45–66 (2012).
106. Latajka, R. *et al.* Pentapeptides containing two dehydrophenylalanine residues--synthesis, structural studies and evaluation of their activity towards cathepsin C. *J. Pept. Sci.* **14**, 1084–1095 (2008).

107. Naiki, H., Higuchi, K., Hosokawa, M. & Takeda, T. Fluorometric determination of amyloid fibrils in vitro using the fluorescent dye, thioflavine T. *Anal. Biochem.* **177**, 244–249 (1989).
108. Hashemi Shabestari, M. *et al.* Conformation and EPR characterization of rigid, 310-helical peptides with TOAC spin labels: Models for short distances. *Pept. Sci.* **102**, 244–251 (2014).
109. Murphy, L. R., Matubayasi, N., Payne, V. A. & Levy, R. M. Protein hydration and unfolding – insights from experimental partial specific volumes and unfolded protein models. *Fold. Des.* **3**, 105–118 (2005).
110. Fischer, H., Polikarpov, I. & Craievich, A. F. Average protein density is a molecular-weight-dependent function. *Protein Sci.* **13**, 2825–2828 (2004).
111. Micsonai, A. *et al.* BeStSel: a web server for accurate protein secondary structure prediction and fold recognition from the circular dichroism spectra. *Nucleic Acids Res.* **46**, W315–W322 (2018).
112. Micsonai, A. *et al.* Accurate secondary structure prediction and fold recognition for circular dichroism spectroscopy. *Proc. Natl. Acad. Sci.* **112**, E3095–E3103 (2015).
113. Biancalana, M. & Koide, S. Molecular mechanism of Thioflavin-T binding to amyloid fibrils. *Biochim. Biophys. Acta (BBA)-Proteins Proteomics* **1804**, 1405–1412 (2010).
114. Milov, A. D., Ponomarev, A. B. & Tsvetkov, Y. D. Electron-electron double resonance in electron spin echo: model biradical systems and the sensitized photolysis of decalin. *Chem. Phys. Lett.* **110**, 67–72 (1984).
115. Bode, B. E. *et al.* Counting the monomers in nanometer-sized oligomers by pulsed electron-electron double resonance. *J. Am. Chem. Soc.* **129**, 6736–6745 (2007).
116. Gu, L. *et al.* Antiparallel triple-strand architecture for prefibrillar A $\beta$ 42 oligomers. *J. Biol. Chem.* **289**, 27300–13 (2014).
117. Cohen, S. I. A. *et al.* Proliferation of amyloid-42 aggregates occurs through a secondary nucleation mechanism. *Proc. Natl. Acad. Sci.* **110**, 9758–9763 (2013).
118. Bleiholder, C., Dupuis, N. F., Wyttenbach, T. & Bowers, M. T. Ion mobility–mass spectrometry reveals a conformational conversion from random assembly to  $\beta$ -sheet in amyloid fibril formation. *Nat. Chem.* **3**, 172 (2011).
119. Seo, J. *et al.* An infrared spectroscopy approach to follow  $\beta$ -sheet formation in peptide amyloid assemblies. *Nat. Chem.* **9**, 39 (2017).
120. Alexander, N., Al-Mestarihi, A., Bortolus, M., Mchaourab, H. & Meiler, J. De novo high-resolution protein structure determination from sparse spin-labeling EPR data. *Structure* **16**, 181–195 (2008).
121. Jao, C. C., Hegde, B. G., Chen, J., Haworth, I. S. & Langen, R. Structure of membrane-bound  $\alpha$ -synuclein from site-directed spin labeling and computational refinement. *Proc. Natl. Acad. Sci.* **105**, 19666–19671 (2008).
122. Meirovitch, E., Liang, Z. & Freed, J. H. Protein dynamics in the solid-state from  $^2\text{H}$  NMR lineshape analysis. III. MOMD in the presence of Magic Angle Spinning. *Solid State Nucl. Magn. Reson.* **89**, 35–44 (2018).
123. Meirovitch, E., Liang, Z. & Freed, J. H. Protein Dynamics in the Solid State from  $^2\text{H}$  NMR Line Shape Analysis. II. MOMD Applied to C-D and C-CD $_3$  Probes. *J. Phys. Chem. B* **119**, 14022–14032 (2015).

124. Budil, D. E., Lee, S., Saxena, S. & Freed, J. H. Nonlinear-least-squares analysis of slow-motion EPR spectra in one and two dimensions using a modified Levenberg–Marquardt algorithm. *J. Magn. Reson. Ser. A* **120**, 155–189 (1996).
125. García de la Torre, J., Huertas, M. . & Carrasco, B. HYDRONMR: Prediction of NMR Relaxation of Globular Proteins from Atomic-Level Structures and Hydrodynamic Calculations. *J. Magn. Reson.* **147**, 138–146 (2000).
126. Perrin, F. Mouvement Brownien d'un ellipsoïde (II). Rotation libre et dépolarisation des fluorescences. Translation et diffusion de molécules ellipsoïdales. *J. Phys. le Radium* **7**, 1–11 (1936).
127. Koenig, S. H. Brownian motion of an ellipsoid. A correction to Perrin's results. *Biopolymers* **14**, 2421–2423 (1975).
128. Marsh, D. & Horváth L.I. *Advanced EPR: applications in biology and biochemistry*. (Elsevier, 2012).
129. López, C. J., Fleissner, M. R., Guo, Z., Kusnetzow, A. K. & Hubbell, W. L. Osmolyte perturbation reveals conformational equilibria in spin-labeled proteins. *Protein Sci.* **18**, 1637–1652 (2009).
130. Columbus, L., Kálai, T., Jekő, J., Hideg, K. & Hubbell, W. L. Molecular motion of spin labeled side chains in  $\alpha$ -helices: analysis by variation of side chain structure. *Biochemistry* **40**, 3828–3846 (2001).
131. Zhang, Z. *et al.* Multifrequency electron spin resonance study of the dynamics of spin labeled T4 lysozyme. *J. Phys. Chem. B* **114**, 5503–5521 (2010).
132. Langen, R., Oh, K. J., Cascio, D. & Hubbell, W. L. Crystal structures of spin labeled T4 lysozyme mutants: implications for the interpretation of EPR spectra in terms of structure. *Biochemistry* **39**, 8396–8405 (2000).
133. Fleissner, M. R., Cascio, D. & Hubbell, W. L. Structural origin of weakly ordered nitroxide motion in spin-labeled proteins. *Protein Sci.* **18**, 893–908 (2009).
134. Clayton, D. F. & George, J. M. The synucleins: a family of proteins involved in synaptic function, plasticity, neurodegeneration and disease. *Trends Neurosci.* **21**, 249–254 (1998).
135. Burré, J. *et al.*  $\alpha$ -Synuclein promotes SNARE-complex assembly in vivo and in vitro. *Science*. **329**, 1663–1667 (2010).
136. Nemani, V. M. *et al.* Increased Expression of  $\alpha$ -Synuclein Reduces Neurotransmitter Release by Inhibiting Synaptic Vesicle Reclustering after Endocytosis. *Neuron* **65**, 66–79 (2010).
137. Villar-Piqué, A., Lopes da Fonseca, T. & Outeiro, T. F. Structure, function and toxicity of alpha-synuclein: the Bermuda triangle in synucleinopathies. *J. Neurochem.* **139**, 240–255 (2016).
138. Arosio, P., Knowles, T. P. J. & Linse, S. On the lag phase in amyloid fibril formation. *Phys. Chem. Chem. Phys.* **17**, 7606–7618 (2015).
139. Ke, P. C. *et al.* Implications of peptide assemblies in amyloid diseases. *Chem. Soc. Rev.* **46**, 6492–6531 (2017).
140. van Diggelen, F., Tepper, A. W. J. W., Apetri, M. M. & Otzen, D. E.  $\alpha$ -Synuclein Oligomers: A Study in Diversity. *Isr. J. Chem.* **57**, 699–723 (2017).
141. Iyer, A. & Claessens, M. M. A. E. Disruptive membrane interactions of alpha-synuclein aggregates. *Biochim. Biophys. Acta - Proteins Proteomics* **1867**, 468–482 (2019).

142. Ilie, I. M. & Caflisch, A. Simulation studies of amyloidogenic polypeptides and their aggregates. *Chem. Rev.* **119**, 6956–6993 (2019).
143. Afitska, K., Fucikova, A., Shvadchak, V. V & Yushchenko, D. A.  $\alpha$ -Synuclein aggregation at low concentrations. *Biochim. Biophys. Acta (BBA)-Proteins Proteomics* **1867**, 701–709 (2019).
144. Cascella, R. *et al.* Probing the Origin of the Toxicity of Oligomeric Aggregates of  $\alpha$ -Synuclein with Antibodies. *ACS Chem. Biol.* **14**, 1352–1362 (2019).
145. Pérez-Pi, I. *et al.*  $\alpha$ -Synuclein-Confocal Nanoscanning (ASYN-CONA), a Bead-Based Assay for Detecting Early-Stage  $\alpha$ -Synuclein Aggregation. *Anal. Chem.* **91**, 5582–5590 (2019).
146. Xu, M., Loa-Kum-Cheung, W., Zhang, H., Quinn, R. J. & Mellick, G. D. Identification of a New  $\alpha$ -Synuclein Aggregation Inhibitor via Mass Spectrometry Based Screening. *ACS Chem. Neurosci.* **10**, acschemneuro.9b00092 (2019).
147. van Diggelen, F. *et al.* Two conformationally distinct  $\alpha$ -synuclein oligomers share common epitopes and the ability to impair long-term potentiation. *PLoS One* **14**, e0213663 (2019).
148. van Raaij, M. E., Segers-Nolten, I. M. J. & Subramaniam, V. Quantitative morphological analysis reveals ultrastructural diversity of amyloid fibrils from  $\alpha$ -synuclein mutants. *Biophys. J.* **91**, L96–L98 (2006).
149. Veldhuis, G., Segers-Nolten, I., Ferlemann, E. & Subramaniam, V. Single-Molecule FRET Reveals Structural Heterogeneity of SDS-Bound  $\alpha$ -Synuclein. *ChemBioChem* **10**, 436–439 (2009).
150. Jao, C. C., Der-Sarkissian, A., Chen, J. & Langen, R. Structure of membrane-bound  $\alpha$ -synuclein studied by site-directed spin labeling. *Proc. Natl. Acad. Sci.* **101**, 8331–8336 (2004).
151. Steigmiller, S., Börsch, M., Gräber, P. & Huber, M. Distances between the b-subunits in the tether domain of F<sub>0</sub>F<sub>1</sub>-ATP synthase from E. coli. *Biochim. Biophys. Acta - Bioenerg.* **1708**, 143–153 (2005).
152. Iljina, M. *et al.* Quantifying co-oligomer formation by  $\alpha$ -synuclein. *ACS Nano* **12**, 10855–10866 (2018).
153. Iljina, M. *et al.* Kinetic model of the aggregation of alpha-synuclein provides insights into prion-like spreading. *Proc. Natl. Acad. Sci.* **113**, E1206–E1215 (2016).
154. Meisl, G. *et al.* Molecular mechanisms of protein aggregation from global fitting of kinetic models. *Nat. Protoc.* **11**, 252 (2016).
155. Gaspar, R. *et al.* Secondary nucleation of monomers on fibril surface dominates  $\alpha$ -synuclein aggregation and provides autocatalytic amyloid amplification. *Q. Rev. Biophys.* **50**, (2017).
156. Cohen, S. I. A. *et al.* Proliferation of amyloid- $\beta$ 42 aggregates occurs through a secondary nucleation mechanism. *Proc. Natl. Acad. Sci.* **110**, 9758–9763 (2013).
157. Drescher, M. *et al.* Spin-label EPR on  $\alpha$ -synuclein reveals differences in the membrane binding affinity of the two antiparallel helices. *ChemBioChem* **9**, 2411–2416 (2008).
158. Reyes, J. F. *et al.* Binding of  $\alpha$ -synuclein oligomers to Cx32 facilitates protein uptake and transfer in neurons and oligodendrocytes. *Acta Neuropathol.* **138**, 23–47 (2019).
159. Quist, A. *et al.* PNAS-2005-Quist-10427-32. **102**, 1–6 (2005).
160. Glabe, C. G. Structural classification of toxic amyloid oligomers. *J. Biol. Chem.* **283**, 29639–29643 (2008).

161. Buell, A. K. *et al.* Solution conditions determine the relative importance of nucleation and growth processes in  $\alpha$ -synuclein aggregation. *Proc. Natl. Acad. Sci.* **111**, 7671–7676 (2014).
162. Pannier, M., Veit, S., Godt, A., Jeschke, G. & Spiess, H. W. Dead-time free measurement of dipole–dipole interactions between electron spins. *J. Magn. Reson.* **142**, 331–340 (2000).
163. Schiemann, O. & Prisner, T. F. Long-range distance determinations in biomacromolecules by EPR spectroscopy. **1**, 1–53 (2020).
164. Drescher, M. EPR in protein science. in *EPR Spectroscopy* 91–119 (Springer, 2011).
165. Tsvetkov, Y. D., Milov, A. D. & Maryasov, A. G. Pulsed electron–electron double resonance (PELDOR) as EPR spectroscopy in nanometre range. *Russ. Chem. Rev.* **77**, 487 (2008).
166. Schmidt, T., Wälti, M. A., Baber, J. L., Hustedt, E. J. & Clore, G. M. Long Distance Measurements up to 160 Å in the GroEL Tetradecamer Using Q-Band DEER EPR Spectroscopy. *Angew. Chemie Int. Ed.* **55**, 15905–15909 (2016).
167. Qi, M., Groß, A., Jeschke, G., Godt, A. & Drescher, M. Gd (III)-PyMTA label is suitable for in-cell EPR. *J. Am. Chem. Soc.* **136**, 15366–15378 (2014).
168. Bellapadrona, G. *et al.* Probing Protein Conformation in Cells by EPR Distance Measurements using Gd 3+ Spin Labeling. *J. Am. Chem. Soc.* **136**, 13458–13465 (2014).
169. Igarashi, R. *et al.* Distance Determination in Proteins inside *Xenopus laevis* Oocytes by Double Electron–Electron Resonance Experiments. *J. Am. Chem. Soc.* **132**, 8228–8229 (2010).
170. Krstić, I. *et al.* Long-range distance measurements on nucleic acids in cells by pulsed EPR spectroscopy. *Angew. Chemie Int. Ed.* **50**, 5070–5074 (2011).
171. Collauto, A. *et al.* Gd ( III ) complexes as paramagnetic tags : Evaluation of the spin delocalization over the nuclei of the ligand. **263**, 156–163 (2016).
172. Garbuio, L., Zimmermann, K., Häussinger, D. & Yulikov, M. Gd ( III ) complexes for electron – electron dipolar spectroscopy : Effects of deuteration , pH and zero field splitting. *J. Magn. Reson.* **259**, 163–173 (2015).
173. Yang, Y. *et al.* A Reactive, Rigid GdIII Labeling Tag for In-Cell EPR Distance Measurements in Proteins. *Angew. Chemie Int. Ed.* **56**, 2914–2918 (2017).
174. Keizers, P. H. J., Desreux, J. F., Overhand, M. & Ubbink, M. Increased paramagnetic effect of a lanthanide protein probe by two-point attachment. *J. Am. Chem. Soc.* **129**, 9292–9293 (2007).
175. Fleissner, M. R. *et al.* Structure and dynamics of a conformationally constrained nitroxide side chain and applications in EPR spectroscopy. *Proc. Natl. Acad. Sci.* **108**, 16241–16246 (2011).
176. Liu, W.-M. *et al.* A Two-Armed Lanthanoid-Chelating Paramagnetic NMR Probe Linked to Proteins via Thioether Linkages. *Chem. - A Eur. J.* **20**, 6256–6258 (2014).
177. Georgieva, E. R. *et al.* Effect of freezing conditions on distances and their distributions derived from Double Electron Electron Resonance (DEER): A study of doubly-spin-labeled T4 lysozyme. *J. Magn. Reson.* **216**, 69–77 (2012).
178. Pannier, M., Veit, S., Godt, A., Jeschke, G. & Spiess, H. . Dead-Time Free Measurement of Dipole–Dipole Interactions between Electron Spins. *J. Magn. Reson.* **142**, 331–340 (2000).
179. Clayton, J. A. *et al.* Gd3+-Gd3+ distances exceeding 3 nm determined by very high frequency continuous wave electron paramagnetic resonance. *Phys. Chem. Chem. Phys.* **19**, 5127–5136 (2017).



180. Matalon, E. *et al.* Gadolinium(III) Spin Labels for High-Sensitivity Distance Measurements in Transmembrane Helices. *Angew. Chemie Int. Ed.* **52**, 11831–11834 (2013).
181. Feintuch, A., Otting, G. & Goldfarb, D. Gd<sup>3+</sup> + Spin Labeling for Measuring Distances in Biomacromolecules: Why and How? *Methods Enzymol.* **563**, 415–457 (2015).
182. Liu, L., Quillin, M. L. & Matthews, B. W. Use of experimental crystallographic phases to examine the hydration of polar and nonpolar cavities in T4 lysozyme. *Proc. Natl. Acad. Sci.* **105**, 14406 – 14411 (2008).
183. Yagi, H. *et al.* Gadolinium tagging for high-precision measurements of 6 nm distances in protein assemblies by EPR. *J. Am. Chem. Soc.* **133**, 10418–10421 (2011).
184. Neuhaus, E. M., Almers, W. & Soldati, T. Morphology and dynamics of the endocytic pathway in Dictyostelium discoideum. *Mol. Biol. Cell* **13**, 1390–1407 (2002).
185. Lu, H. P. Revealing time bunching effect in single-molecule enzyme conformational dynamics. *Phys. Chem. Chem. Phys.* **13**, 6734–6749 (2011).
186. Yang, Y., Yang, F., Li, X.-Y., Su, X.-C. & Goldfarb, D. In-Cell EPR Distance Measurements on Ubiquitin Labeled with a Rigid PyMTA-Gd(III) Tag. *J. Phys. Chem. B* **123**, 1050–1059 (2019).
187. Annesley, S. J. & Fisher, P. R. Dictyostelium discoideum—a model for many reasons. *Mol. Cell. Biochem.* **329**, 73–91 (2009).
188. Richman, M. *et al.* In vitro and mechanistic studies of an antiamyloidogenic self-assembled cyclic d, l- $\alpha$ -peptide architecture. *J. Am. Chem. Soc.* **135**, 3474–3484 (2013).
189. Chemerovski-glikman, M., Richman, M. & Rahimipour, S. Structure-based study of antiamyloidogenic cyclic D, L - a -peptides. *Tetrahedron* **70**, 7639–7644 (2014).
190. Barnes, D. E. & Yaffe, K. The projected effect of risk factor reduction on Alzheimer’s disease prevalence. *Lancet Neurol.* **10**, 819–828 (2011).
191. Roßner, S., Sastre, M., Bourne, K. & Lichtenthaler, S. F. Transcriptional and translational regulation of BACE1 expression-Implications for Alzheimer’s disease. *Prog. Neurobiol.* **79**, 95–111 (2006).
192. Bucciantini, M. *et al.* Inherent toxicity of aggregates implies a common mechanism for protein misfolding diseases. *Nature* **416**, 507–511 (2002).
193. Kelly, J. W. The alternative conformations of amyloidogenic proteins and their multi-step assembly pathways. *Curr. Opin. Struct. Biol.* **8**, 101–106 (1998).
194. Dobson, C. M., Swoboda, B. E. P., Joniau, M. & Weissman, C. The structural basis of protein folding and its links with human disease. *Philos. Trans. R. Soc. B Biol. Sci.* **356**, 133–145 (2001).
195. Chiti, F. & Dobson, C. M. Protein Misfolding, Functional Amyloid, and Human Disease. *Annu. Rev. Biochem.* **75**, 333–366 (2006).
196. Chiti, F. & Dobson, C. M. Protein Misfolding, Amyloid Formation, and Human Disease: A Summary of Progress Over the Last Decade. *Annu. Rev. Biochem.* **86**, 27–68 (2017).
197. Zurlo, E., Gorroño Bikandi, I., Meeuwenoord, N. J., Filippov, D. V. & Huber, M. Tracking amyloid oligomerization with monomer resolution using a 13-amino acid peptide with a backbone-fixed spin label. *Phys. Chem. Chem. Phys.* **21**, 25187–25195 (2019).
198. Ghalebani, L., Wahlström, A., Danielsson, J., Wärmländer, S. K. T. S. & Gräslund, A. pH-dependence of the specific binding of Cu(II) and Zn(II) ions to the amyloid- $\beta$  peptide.

- Biochem. Biophys. Res. Commun.* **421**, 554–560 (2012).
199. Vassar, P. S. & Culling, C. F. Fluorescent stains, with special reference to amyloid and connective tissues. *Arch. Pathol.* **68**, 487–498 (1959).
  200. Di Valentin, M., Albertini, M., Zurlo, E., Gobbo, M. & Carbonera, D. Porphyrin triplet state as a potential Spin label for nanometer distance measurements by peldor spectroscopy. *J. Am. Chem. Soc.* **136**, (2014).
  201. Sepkhanova, I. *et al.* Monitoring Alzheimer amyloid peptide aggregation by EPR. *Appl. Magn. Reson.* **36**, 209 (2009).
  202. Chen, M., Margittai, M., Chen, J. & Langen, R. Investigation of  $\alpha$ -synuclein fibril structure by site-directed spin labeling. *J. Biol. Chem.* **282**, 24970–24979 (2007).
  203. Margittai, M. & Langen, R. Template-assisted filament growth by parallel stacking of tau. *Proc. Natl. Acad. Sci. U. S. A.* **101**, 10278–10283 (2004).
  204. Lebel, R. G. & Goring, D. A. I. Density, Viscosity, Refractive Index, and Hygroscopicity of Mixtures of Water and Dimethyl Sulfoxide. *J. Chem. Eng. Data* **7**, 100–101 (1962).

# Summary

Neurodegenerative diseases, such as Parkinson's disease (PD) and Alzheimer's disease (AD), are expected to become more widespread in the future due to the ageing of the population, thereby causing large problems for society and for the economy. So far, no cure has been found, largely because the mechanism of the disease is not clearly understood. Here we focus on one such mechanism: Amyloid aggregation. In the brains of patients with neurodegenerative diseases, plaques of  $\beta$ -sheet amyloid aggregates are found, but the mechanism of their formation and their role vis-à-vis the disease are unknown. Aggregation is difficult to study because amyloids are intrinsically disordered proteins that lack an ordered structure in solution. Here we apply electron paramagnetic resonance (EPR) as a new technique to better understand the properties of amyloid oligomers and their formation. **Chapter 1** gives a general overview of amyloid systems and briefly describes the EPR methods applied in this thesis.

Amyloid aggregation is the process in which amyloid proteins self-assemble and exhibit toxicity. The thermodynamic end-point of the aggregation is the formation of fibrils. Meanwhile, evidence is growing that amyloid oligomers, not fibrils, are the more toxic species. Oligomers are aggregates of up to tens to hundred monomers. They can be on-pathway to fibril formation or off-pathway. Oligomers can differ in size, i.e., the number of peptides, structure, stability and physico-chemical properties. Their transient nature and heterogeneity make oligomers difficult to track.

The first step in this thesis is to determine if EPR is a suitable technique for the detection and characterization of amyloid oligomers. In **Chapter 2** we show how EPR can be applied to detect the formation of amyloid aggregates. We choose the K1V peptide as a model because it forms reasonably stable oligomers and fibrilizes much more slowly than most other amyloids. We synthesize, by solid phase peptide synthesis (SPPS), three variants of the K1V peptide, containing the TOAC spin label in three different positions. We use liquid solution, room-temperature continuous-wave EPR (cw EPR) to determine if oligomers can be detected by EPR. This method is sensitive to the nano-second rotational motion of the nitroxide. We show how changes in the mobility of the TOAC spin label, detected by EPR, allow us to detect the formation of aggregates.

After establishing that EPR can detect the aggregation of the spin-labeled peptide, in **Chapter 3** we show how EPR can also be used to characterize the structures of the aggregates. From the lineshape of the EPR spectra we estimate the size of the aggregates. As larger aggregates have a slower motion than smaller aggregates, the rotational mobility reflects the size, i.e. the volume of the oligomers. The volume is related to the number of monomers assembled in the aggregates, so we estimate the number of peptides in the constructs. By EPR we observe that there are multiple species of aggregates in the solution and that one of these is probably the known oligomer of the original K1V peptide reported in literature.

In **Chapter 4**, the ability of cw EPR to detect oligomers in solution is used to study the kinetics of the aggregation of  $\alpha$ -Synuclein, the amyloid protein believed to be related to Parkinson's disease. We present how, by EPR, the amount of intermediates can be measured over the course of the aggregation, directly in the reacting solution, without the need for separation. We show that primary oligomers can be detected, which are formed directly from monomeric species, rather than by secondary nucleation processes. These oligomers are short-lived, such that the majority of them dissociates before converting to fibrils.

Ascertained that EPR can be used to study the properties of the aggregation of amyloid proteins, we investigate if it can be used to detect the inhibition of aggregation. In **Chapter 6** we present a study on the aggregation of the amyloid  $\beta$  ( $A\beta$ ) peptide, the peptide related to Alzheimer's disease. We synthesized two variants of  $A\beta$  with the TOAC spin label at different positions and we measured their aggregation by cw EPR at 9 GHz and 95 GHz. We apply a drug candidate, a cyclic D,L- $\alpha$ -peptide (CP-2), which, in previous studies, was shown to inhibit the fibril formation of  $A\beta$ . By EPR we show that the interaction of  $A\beta$  with CP-2 can be detected and that multiple CP-2 peptides must be involved in the interaction.

EPR is a technique with a vast range of uses, especially in biological systems. In **Chapter 5** we demonstrate that EPR cannot only be applied to proteins *in vitro*, but can also be used to study proteins in the cell. We present how double electron-electron resonance (DEER) spectroscopy can be used *in-cell*. The technique, DEER, is a pulsed EPR method that measures distances between paramagnetic centers. The main obstacle into performing DEER *in-cell* is that most paramagnetic centers are degraded by the reducing cell medium. In **Chapter 6** we present the properties of three recently developed Gd(III) labeling tags, Gd-CLaNP<sub>13i</sub> (i = a,b,c) attached to the Bacteriophage T4-Lysozyme protein. We demonstrate the excellent performance of these new tags for *in-cell* DEER measurements. The experiments show a stable conjugation of the labels to the protein, a high binding constant of the Gd (III) even under *in-cell* conditions, and high rigidity of the clamp resulting in narrow distance distributions.

This thesis shows how EPR can be used to better understand and characterize the aggregation of amyloid peptides and proteins. The final step shows how EPR can be applied to proteins in cells opening up the possibility to expand the study amyloids also to the native environment of the cell.

# Samenvatting

Neurodegeneratieve ziekten, zoals de ziekte van Parkinson (PD) en de ziekte van Alzheimer (AD), zullen naar verwachting in de toekomst meer en meer voorkomen als gevolg van de vergrijzing van de bevolking, wat grote problemen zal veroorzaken voor de samenleving en de economie. Tot dusver is er nog geen geneesmiddel tegen de ziekte gevonden, vooral omdat het mechanisme van de ziekte nog niet goed begrepen is. De aandacht zal in dit proefschrift uitgaan naar de aggregatie van amyloïde. In de hersenen van patiënten met neurodegeneratieve ziekten worden plaques van  $\beta$ -sheet amyloïde aggregaten gevonden, maar het mechanisme van hun vorming en hun rol in het ziekteproces zijn onbekend. Aggregatie is moeilijk te bestuderen omdat amyloïden bestaan uit intrinsiek ongeordende eiwitten. Dat wil zeggen dat ze in oplossing geen geordende structuur aannemen. In ons onderzoek passen wij elektron paramagnetische resonantie (EPR) toe als een nieuwe techniek om de eigenschappen van amyloïde oligomeren en hun ontstaan beter te begrijpen. **Hoofdstuk 1** geeft een algemeen overzicht van amyloïdesystemen en beschrijft in het kort de EPR-methoden die in dit proefschrift worden toegepast.

De vorming van amyloïden komt tot stand tijdens een proces waarbij amyloïde eiwitten samenklonteren en toxisch worden. Het thermodynamische eindpunt van de aggregatie is de vorming van vezels (fibrillen). Inmiddels zijn er steeds meer aanwijzingen die erop duiden dat amyloïde oligomeren toxischer zijn dan fibrillen. Oligomeren zijn aggregaten van tientallen tot honderd monomeren. Oligomeren kunnen een tussenstadium vertegenwoordigen op de weg naar de vorming van fibrillen, maar ze kunnen ook op zichzelf bestaan. Oligomeren kunnen verschillen in grootte (aantal peptiden), structuur, stabiliteit en fysisch-chemische eigenschappen. Door hun instabiliteit en heterogeniteit zijn de oligomeren moeilijk te bestuderen.

De eerste stap in ons onderzoek was om vast te stellen of EPR een geschikte techniek is voor de detectie en karakterisering van amyloïde oligomeren. In **Hoofdstuk 2** laten we zien hoe EPR kan worden toegepast om de vorming van amyloïdaggregaten te detecteren. We hebben hiervoor het K1V-peptide als model gekozen omdat het stabielere oligomeren vormt en omdat het veel langzamer aggregaat dan de meeste andere amyloïde vormende varianten. Door middel van solid-phase peptidesynthese (SPPS) synthetiseren we drie varianten van het K1V-peptide, die het zgn TOAC-spinlabel op drie verschillende posities bevatten. We gebruiken “continuous wave” EPR (cw EPR) aan oplossingen bij kamertemperatuur om te bepalen of oligomeren met EPR kunnen worden gedetecteerd. Het EPR signaal is gevoelig voor de rotaties van het nitroxide spin label. We laten zien hoe veranderingen in de mobiliteit van het TOAC-spinlabel kunnen worden gedetecteerd met EPR en hoe dit ons in staat stelt de vorming van aggregaten waar te nemen.

Nadat we hebben vastgesteld dat we met EPR aggregatie kunnen detecteren, laten we in **Hoofdstuk 3** zien hoe EPR kan worden gebruikt om meer te weten te komen over de structuur van de aggregaten. Uit de lijnvorm van de EPR-spectra kunnen we de grootte van de aggregaten als volgt inschatten. Grotere aggregaten bewegen langzamer dan kleinere aggregaten, d.w.z. hun beweeglijkheid weerspiegelt de grootte oftewel het volume van de oligomeren, dat op haar beurt weer is gerelateerd aan het aantal monomeren waaruit de aggregaten bestaan. Aangezien de EPR lijnvorm is gerelateerd aan beweeglijkheid kunnen we uit de lijnvorm dus de beweeglijkheid en daarmee de grootte van de oligomeren inschatten. Ook zien we met behulp van EPR dat er verscheidene soorten aggregaat in oplossing aanwezig zijn. Eén daarvan is waarschijnlijk het bekende oligomeer van het oorspronkelijke K11V-peptide dat in de literatuur wordt vermeld.

In **Hoofdstuk 4**, gebruiken we cw EPR om oligomeren in oplossing te detecteren en om de kinetiek van de aggregatie van  $\alpha$ -synucleïne te bestuderen.  $\alpha$ -Synucleïne is het eiwit dat het ameloïde vormt dat gerelateerd is aan de ziekte van Parkinson. Door middel van EPR kan de hoeveelheid tussenproducten, ontstaan tijdens de vorming van aggregaten, rechtstreeks in de oplossing worden gemeten zonder dat de verschillende aggregaten eerst van elkaar gescheiden hoeven te worden. We tonen aan dat primaire oligomeren eerder worden gedetecteerd in monomere soorten dan in secundaire producten. Deze oligomeren hebben een korte levensduur doordat de meerderheid van hen dissocieert in plaats van tot vezels te associëren.

Wetend dat EPR kan worden gebruikt om de aggregatie van amyloïde eiwitten te bestuderen, onderzoeken we of EPR ook kan worden gebruikt om de remming van het aggregatieproces te detecteren. In **Hoofdstuk 6** presenteren we een studie over de aggregatie van het amyloïde  $\beta$ -peptide ( $A\beta$ ), het peptide dat verband houdt met de ziekte van Alzheimer. We hebben twee varianten van  $A\beta$  gesynthetiseerd met het TOAC-spinlabel op verschillende posities en we hebben met behulp van cw EPR bij 9 GHz en 95 GHz hun aggregatie gemeten. We passen een kandidaat-geneesmiddel toe, een cyclisch D, L- $\alpha$ -peptide (CP-2), waarvan in eerdere studies werd aangetoond dat het de fibrilvorming van  $A\beta$  remt. Met behulp van EPR laten we zien dat de interactie van  $A\beta$  met CP-2 kan worden gedetecteerd en dat meerdere CP-2-peptiden bij de interactie betrokken moeten zijn.

EPR is een techniek met een breed scala aan toepassingen, vooral in biologische systemen. In **Hoofdstuk 5** tonen we aan dat EPR niet alleen in *in-vitro* studies van eiwitten kan worden toegepast, maar dat EPR ook kan worden gebruikt om eiwitten *in de cel* te bestuderen. We laten zien hoe dubbele elektronen-elektronen resonantie (DEER) spectroscopie kan worden toegepast *in de cel*. De DEER-techniek is een methode die gebruik maakt van microgolf pulsen en die afstanden tussen paramagnetische centra meet. Het voornaamste obstakel bij het uitvoeren van DEER *in de cel* is dat de meeste paramagnetische centra in het reducerende cel milieu worden

afgebroken. In **Hoofdstuk 6** presenteren we de eigenschappen van drie recent ontwikkelde Gd (III) labels, Gd-CLaNP<sub>13i</sub> (i = a, b, c) gekoppeld aan het Bacteriofaag T<sub>4</sub>-Lysozyme-eiwit. We laten zien dat deze labels bij uitstek geschikt zijn als nieuwe tags voor DEER-metingen *in de cel*. Er blijkt een stabiele koppeling van de labels aan het eiwit tot stand te komen die gepaard gaat met een hoge bindingsconstante van het Gd (III), zelfs onder *in-cel* omstandigheden, en met een hoge stijfheid van het construct, resulterend in nauwe afstandsverdelingen.

Dit proefschrift laat zien hoe EPR kan worden gebruikt om de aggregatie van amyloïde peptiden en van eiwitten beter te begrijpen en te karakteriseren. Het laatste hoofdstuk laat zien hoe EPR kan worden toegepast op eiwitten in cellen, waardoor we, naar we hopen, in de toekomst de mogelijkheid krijgen om het onderzoek naar amyloïden uit te breiden naar de natuurlijke omgeving van de cel.





# Curriculum vitae

Enrico Zurlo

August 26, 1987 Born in Cittadella, Veneto.

## *Research Experience*

February 2015 – June 2020

PhD student, Huygens-Kamerlingh Onnes Laboratory, Leiden Institute of Physics, Leiden University, Leiden, The Netherlands

February 2014 – January 2015

Junior research fellow, Department of Chemistry, University of Padova, Italy

Project : Phonon-Assisted Processes for Energy Transfer and Sensing

Supervisor: dr. Elisabetta Collini

## *Education*

September 2009 – October 2013

M. Sc. in Chemistry, Department of Chemistry, University of Padova, Italy

Project: Distance information by double electron-electron resonance (DEER) on a spin-labelled peptide conjugated to a porphyrin

Supervisor: dr. Marilena Di Valentin

September 2006 – September 2009

B. Sc. in Chemistry, Department of Chemistry, University of Padova, Italy

Project: Development of the setup for the quantification of nitroxide in plants by EPR spectroscopy

Supervisor: dr. Marilena Di Valentin



## List of publications

- **Zurlo, E.**, Gorroño Bikandi, I., Meeuwenoord, N. J., Filippov, D. V. & Huber, M. Tracking amyloid oligomerization with monomer resolution using a  $^{13}$ -amino acid peptide with a backbone-fixed spin label. *Phys. Chem. Chem. Phys.* **21**, 25187–25195 (2019).
- Gast P, Mance D, **Zurlo E**, Ivanov KL, Baldus M, Huber M. A tailored multi-frequency EPR approach to accurately determine the magnetic resonance parameters of dynamic nuclear polarization agents: Application to AMUPol. *Phys. Chem. Chem. Phys.* **19**, (2017).
- Di Valentin, M., Albertini, M., **Zurlo, E.**, Gobbo, M. & Carbonera, D. Porphyrin triplet state as a potential Spin label for nanometer distance measurements by peldor spectroscopy. *J. Am. Chem. Soc.* **136**, 6582–6585 (2014).
- Di Valentin M, Albertini M, Dal Farra MG, **Zurlo E**, Orian L, Polimeno A. Light-Induced Porphyrin-Based Spectroscopic Ruler for Nanometer Distance Measurements. *Chem. - A Eur. J.* **22**, (2016).
- Biscaglia F, Frezza E, **Zurlo E**, Gobbo M. Linker dependent chirality of solvent induced self-assembled structures of porphyrin- $\alpha$ -helical peptide conjugates. *Org Biomol Chem* 2016; **14**.

## In preparation

- **Enrico Zurlo**, Pravin Kumar, Georg Meisl, Alexander J Dear, Dipro Mondal, Mireille M.A.E. Claessens, Tuomas P J Knowles, Martina Huber, In situ kinetic measurements of  $\alpha$ -synuclein aggregation reveal large population of short-lived oligomers
- Qing Miao, **Enrico Zurlo**, Donny de Bruin, Joeri A. J. Wondergem, Monika Timmer, Anneloes Blok, Doris Heinrich, Mark Overhand, Martina Huber, Marcellus Ubbink, A two-armed probe for in-cell DEER measurements on proteins



# Acknowledgments

The end of my PhD is getting closer, so it also becomes more clear in my mind who has deeply contributed to this journey. Each person will be embedded in my memories for the help they have given me to achieve this goal. Some of them helped me in the professional area, while others helped me in my private life, but they share the fact that without them, I would not have succeeded in completing this thesis.

First and foremost, I want to express my gratitude to my supervisor, Dr. Martina Huber for giving me the possibility to join the project. Her wide knowledge and passion for science has given me new insight and directions for the development of the project. I was really lucky to be under her supervision.

I want to thank Prof. Edgar Groenen, Dr. Peter Gast and Dr. Huib Blok for inspiring discussion on EPR during the whole project and for allowing me to use equipment developed by them. Dr. Faezeh Nami, Dr. Mikhailo Azarkh, **Dr. Pravin Kumar** and Dr. Gabriele Panarelli were also helpful friends who helped me develop my knowledge of EPR and overcome many issues. A special thank goes to Iraitz Gorroño Bikandi, my bachelor student, who acknowledged me as his Master for the rest of his life.

I acknowledge the assistance offered by Nico Meeuwenoord, Lionel Ndamba, Marcel Winter and Dr. Dimitri Filippov in the peptides synthesis and preparation, and their availability to help me use the equipment in their labs. Thanks to them I obtained high-quality samples that proved useful in my research.

I must be thankful to Dr. Miao Q. for our collaboration project which has shown very interesting results and inspiration for future research.

Assistance by Henriette van Leeuwen for administrative support, Harmen van der Meer and Jos Disselhorst for technical assistance, and Dr. Federica Galli regarding AFM experiments, is gratefully acknowledged.

I would like to thank Prof. Eric Eliel for offering his guidance during my PhD and teaching me the best ways to overcome difficulties.

I would like to thank all PhD students who shared these 8 years as colleagues and friends: Dipro, Weichun, Martin C., Martin B., Marija, Aquiles, Miao X., Saptaswa, Thomas, Francesca, Antonella, Donny, Biswajit, and all the people present in the MONOS group right now.

Especially thankful I am to Bahar Zhalehgooyan for her genuine love and incredible support in the most difficult moments of my life. I am happy we have accomplished such a thing together and look forward to what the future will bring us.

I would like to thank my parents for their boundless love and support in each moment of my life, and especially for my mother who unluckily could not witness the moment I became a doctor.